The Astrophysical Journal, 731:102 (31pp), 2011 April 20 doi:10.1088/0004-637X/731/2/102

THE NONLINEAR BIASING OF THE zCOSMOS GALAXIES UP TO $z \sim 1$ FROM THE 10k SAMPLE*

K. Kovač[1], C. Porciani[1,2], S. J. Lilly[1], C. Marinoni[3], L. Guzzo[4], O. Cucciati[5], G. Zamorani[6], A. Iovino[4], P. Oesch[1], M. Bolzonella[6], Y. Peng[1], B. Meneux[7,8], E. Zucca[6], S. Bardelli[6], C. M. Carollo[1], T. Contini[9], J.-P. Kneib[5], O. Le Fèvre[5], V. Mainieri[10], A. Renzini[11], M. Scodeggio[12], A. Bongiorno[7], K. Caputi[1], G. Coppa[6], S. de la Torre[4,5,12], L. de Ravel[5], A. Finoguenov[7], P. Franzetti[12], B. Garilli[12], P. Kampczyk[1], C. Knobel[1], F. Lamareille[9], J.-F. Le Borgne[9], V. Le Brun[5], C. Maier[1], M. Mignoli[6], R. Pello[9], E. Perez-Montero[9], L. Pozzetti[6], E. Ricciardelli[13], J. D. Silverman[1], M. Tanaka[10], L. A. M. Tasca[5,12], L. Tresse[5], D. Vergani[6], U. Abbas[5,14], D. Bottini[12], A. Cappi[6], P. Cassata[5,15], A. Cimatti[16], M. Fumana[12], A. M. Koekemoer[17], A. Leauthaud[18], D. Maccagni[12], H. J. McCracken[19], P. Memeo[12], R. Scaramella[20], and N. Z. Scoville[21]

[1] Institute of Astronomy, ETH Zurich, 8093 Zurich, Switzerland; kovac@phys.ethz.ch
[2] Argelander Institut für Astronomie, Auf dem Hügel 71, D-53121 Bonn, Germany
[3] Centre de Physique Theorique, Marseille, France
[4] INAF Osservatorio Astronomico di Brera, Milan, Italy
[5] Laboratoire d'Astrophysique de Marseille, Marseille, France
[6] INAF Osservatorio Astronomico di Bologna, via Ranzani 1, I-40127 Bologna, Italy
[7] Max-Planck-Institut für extraterrestrische Physik, D-84571 Garching, Germany
[8] Universitats-Sternwarte, Scheinerstrasse 1, D-81679 Muenchen, Germany
[9] Laboratoire d'Astrophysique de Toulouse-Tarbes, Universite de Toulouse, CNRS, 14 avenue Edouard Belin, F-31400 Toulouse, France
[10] European Southern Observatory, Karl-Schwarzschild- Strasse 2, Garching, D-85748, Germany
[11] INAF-Osservatorio Astronomico di Padova, Padova, Italy
[12] INAF-IASF Milano, Milan, Italy
[13] Dipartimento di Astronomia, Universita di Padova, Padova, Italy
[14] INAF Osservatorio Astronomico di Torino, Strada Osservatorio 20, I-10025 Pino Torinese, Torino, Italy
[15] Department of Astronomy, University of Massachusetts at Amherst, MA 01003, USA
[16] Dipartimento di Astronomia, Universitá di Bologna, via Ranzani 1, I-40127 Bologna, Italy
[17] Space Telescope Science Institute, 3700 San Martin Drive, Baltimore, MD 21218, USA
[18] Physics Division, MS 50 R5004, Lawrence Berkeley National Laboratory, 1 Cyclotron Road, Berkeley, CA 94720, USA
[19] Institut d'Astrophysique de Paris, UMR 7095 CNRS, Université Pierre et Marie Curie, 98 bis Boulevard Arago, F-75014 Paris, France
[20] INAF, Osservatorio di Roma, Monteporzio Catone (RM), Italy
[21] California Institute of Technology, MS 105-24, Pasadena, CA 91125, USA
Received 2009 September 8; accepted 2011 January 28; published 2011 March 30

ABSTRACT

We use the zCOSMOS galaxy overdensity field to study the biasing of galaxies in the COSMOS field. By comparing the probability distribution function of the galaxy density contrast δ_g to the lognormal approximation of the mass density contrast δ, we obtain the mean biasing function $b(\delta, z, R)$ between the galaxy and matter overdensity fields and its second moments $\hat{b}$ and $\tilde{b}$. Over the redshift interval $0.4 < z < 1$ the conditional mean function $\langle \delta_g | \delta \rangle = b(\delta, z, R)\delta$ is of a characteristic shape, requiring nonlinear biasing in the most overdense and underdense regions. Taking into account the uncertainties due to cosmic variance, we do not detect any significant evolution in the $\langle \delta_g | \delta \rangle$ function, but we do detect a significant redshift evolution in the linear biasing parameter $\hat{b}$ from 1.23 ± 0.11 at $z \sim 0.55$ to 1.62 ± 0.14 at $z \sim 0.75$, for a luminosity-complete sample of $M_B < -20 - z$ galaxies. The $\hat{b}$ parameter does not change significantly with smoothing scale between 8 and $12\,h^{-1}$ Mpc, but increases systematically with luminosity (at 2σ–3σ significance between the $M_B < -20.5 - z$ and $M_B < -20 - z$ samples). The nonlinearity parameter $\tilde{b}/\hat{b}$ is offset from unity by at most 2%, with an uncertainty of the same order. The $\tilde{b}/\hat{b}$ parameter does not show any significant redshift evolution, dependence on the smoothing scale or on the luminosity. By matching the linear bias of galaxies to the halo bias, we infer that the $M_B < -20 - z$ galaxies reside in dark matter halos with a characteristic mass of about $(2.6-5.6) \times 10^{12}\,M_\odot$ with a small dependence on the adopted bias–mass relation. Our detailed error analysis and comparison with previous studies lead us to conclude that cosmic variance is the main contributor to the differences in the linear bias measured from different surveys. While our results support the general picture of biased galaxy formation up to $z \sim 1$, the fine-tuning of the galaxy formation models is still limited by the restrictions of the current spectroscopic surveys at these redshifts.

Key words: cosmology: observations – galaxies: evolution – galaxies: statistics

Online-only material: color figures

1. INTRODUCTION

The large-scale structure in the universe is believed to have formed via gravitational instability of small, primordial density fluctuations. Virialized dark matter halos are produced by the collapse of some overdense regions followed by hierarchical merging. Galaxies are formed within the dark matter halos through multiplex processes including gas cooling, star formation, and feedback which are difficult to model accurately (e.g., White & Rees 1978). It is thus expected that the relation between galaxies and the underlying matter distribution will also

* Based on observations obtained at the European Southern Observatory (ESO) Very Large Telescope (VLT), Paranal, Chile, as part of the Large Program 175.A-0839 (the zCOSMOS Spectroscopic Redshift Survey).

be complex. In particular, the efficiency of galaxy formation and the rate of galaxy evolution might vary from place to place depending on the matter density field. Therefore, the actual galaxy distributions are not expected to be a faithful tracer of the underlying mass. This phenomenon is often referred to as "galaxy biasing."

In order to extract cosmological information from galaxy surveys, it is important to model and parameterize galaxy biasing. This often requires using a statistical approach. Assuming that galaxies preferentially form within the peaks of the primordial density distribution, Kaiser (1984) showed that the two-point correlation function of the galaxy distribution, ξ_{gg}, should be amplified with respect to the mass autocorrelation function, ξ_{mm}, according to the relation

$$\xi_{gg}(r) = b_\xi^2 \xi_{mm}(r), \tag{1}$$

where the "biasing parameter" b_ξ is independent of the spatial separation r. A similar relation is obtained by relating the density contrast of the matter δ and of the galaxies δ_g at some position $\mathbf{r}$ through the deterministic and linear relation

$$\delta_g(\mathbf{r}) = b\,\delta(\mathbf{r}). \tag{2}$$

This is the simplest model for galaxy biasing and is still commonly used. While Equation (1) follows from Equation (2), the opposite does not hold. An obvious deficiency in the definition of δ_g above is that it will break down in the most underdense regions $\delta \ll 0$ if $b > 1$, as values of $\delta_g < -1$ are not possible. This implies that the galaxy bias b must be a nonlinear function of δ and, in general, it can also vary with redshift z, galaxy type, and the smoothing scale R used to define the density contrast:

$$b = b(\delta, z, R). \tag{3}$$

Fry & Gaztanaga (1993) proposed to parameterize this function in terms of coefficients of the Taylor expansion

$$\delta_g = b_0 + b_1\,\delta + \frac{b_2}{2}\,\delta^2 + \cdots, \tag{4}$$

subject to the constraints that $\langle \delta_g \rangle = 0$ and $\delta_g(\delta = -1) = -1$.

Galaxy biasing is also expected to have a stochastic element: for any given value of δ there will be a whole distribution of values for δ_g. The stochasticity originates from a number of different sources. First, the dynamics of large-scale flows depends on extra variables beyond the value of the local density contrast δ (e.g., on the tidal tensor) and makes the bias relation nonlinear, non-local, and stochastic (Catelan et al. 1998). Second, the efficiency of galaxy formation depends on details of the gas physics. Third, galaxies are discrete objects and any attempt to reconstruct δ_g will be affected by shot noise.

Dekel & Lahav (1999) have proposed a formalism which separately accounts for the nonlinearity and stochasticity of the biasing process. Galaxy biasing is described in terms of the conditional probability function $P(\delta_g|\delta)$ and its moments. A key quantity here is the mean biasing function $b(\delta)$ defined by the conditional mean

$$b(\delta)\delta = \langle \delta_g|\delta \rangle = \int d\delta_g\, P(\delta_g|\delta)\delta_g. \tag{5}$$

The mean biasing function $b(\delta)$ and its nonlinearity can be characterized by its second non-trivial moments:

$$\hat{b} \equiv \frac{\langle b(\delta)\delta^2 \rangle}{\sigma^2} \tag{6}$$

and

$$\tilde{b}^2 \equiv \frac{\langle b^2(\delta)\delta^2 \rangle}{\sigma^2}, \tag{7}$$

with σ^2 being the variance of the distribution of mass density contrasts. The expectation values are taken from the probability distribution of the corresponding density fields, as in Equation (5). The parameter $\hat{b}$ measures the slope of the linear regression of δ_g against δ. In the case of linear biasing (see Equation (2)), both $\hat{b}$ and $\tilde{b}$ reduce to the constant bias. The ratio $\tilde{b}/\hat{b}$ is thus a measure of the nonlinearity in the biasing relation. Moreover, the local variance of δ_g at fixed δ, $\sigma_g^2(\delta)$ can be used to quantify the degree of stochasticity of the biasing relation.

Based on the Press–Schechter formalism and its extensions (Bond et al. 1991), Mo & White (1996) developed an analytical model for the mean biasing relation of the dark matter halos. This assumes that large-scale motions follow the spherical collapse approximation. The general case is discussed by Catelan et al. (1998). Related work has been presented in Mo et al. (1997) and Porciani et al. (1998; see also Scannapieco & Barkana 2002) where two-point and higher-order statistics are considered. Following the analytical approach by Mo & White (1996), a number of studies based on N-body simulations were carried out to study the halo bias (e.g., Jing 1998; Porciani et al. 1999; Sheth & Lemson 1999; Sheth & Tormen 1999; Jing 1999; Kravtsov & Klypin 1999; Sheth et al. 2001; Seljak & Warren 2004; Tinker et al. 2005; Pillepich et al. 2010), leading to a new set of fitting formulae for the mean biasing relation, and a better understanding of the origin of halo biasing. Independently of the exact halo definition, assumed cosmology, simulation box size, and resolution, there is a consensus that in a cold-dark matter scenario: (1) at a given epoch, more massive halos are more biased tracers of the underlying matter than lower mass halos; (2) for halos of fixed mass, the amount of biasing increases with redshift.

However, it is still a huge step from a successful description of "halo biasing" to that of "galaxy biasing", as the latter requires incorporating a recipe for galaxy formation (and evolution) within the current cosmological framework. Galaxy biasing has been studied through hydrodynamic simulations (e.g., Blanton et al. 1999, 2000; Cen & Ostriker 2000; Yoshikawa et al. 2001) and semi-analytical modeling (SAM) combined with N-body simulations (e.g., Kauffmann et al. 1997; Benson et al. 2000; Somerville et al. 2001; Sigad et al. 2000, hereafter SBD). Despite the difference in the treatment of the various gas-related processes, all these studies reach the following consistent conclusions: galaxy biasing is expected to be nonlinear, to depend on the properties of the considered galaxy sample (and of their host dark matter halos), and to be a function of cosmic time.

There is now a lot of observational evidence for galaxy biasing, and its dependence on galaxy type or redshift. The Dressler's morphology–density relation (Dressler 1980)—the observational evidence that early-type galaxies are more abundant in dense regions than spiral galaxies—is a textbook example for this. Building on this, one can summarize decades of observations in the local universe with a statement that bulge-dominated, red galaxies with mainly old stellar populations preferentially live in dense regions, and they are more strongly clustered than the disk-dominated, blue, young galaxies (e.g., Norberg et al. 2001, 2002; Zehavi et al. 2005). Consistently, deriving the bias parameter from clustering studies (see, e.g., Equation (1)) suggests that early-type galaxies have a higher

bias than late-type galaxies at all luminosities (Norberg et al. 2002). On the other hand, H I-selected galaxies have some of the lowest bias values of all known objects (Basilakos et al. 2007). At higher redshifts, galaxies are more biased tracers of matter, with linear bias parameters of $b \sim 1.48$ at $0.7 < z < 1.3$ for $M_B < -20$ galaxies (Coil et al. 2006, see also Pollo et al. 2006 and Meneux et al. 2009), up to the highest biased samples of extremely red objects (EROs), Lyman Break galaxies (LBGs), and Lyman-α emitters. For example, the bias parameter of EROs at $z = 1.2$ is $b = 2.7$ (Moustakas & Somerville 2002), LBGs at $z \sim 3.8$ and $z \sim 4.9$ are $b \sim 2.5$ and $b \sim 4$, respectively, (Lee et al. 2006) and the bias parameter of Lyman-α emitters at $z \sim 4.5$ is $b \sim 3.7$ (Kovač et al. 2007). However, inferring the exact redshift evolution of the biasing process from the observational data is not straightforward because galaxy surveys typically sample different populations of galaxies at different redshifts (e.g., Kovač et al. 2007).

A simple way to model the biasing of galaxies which has received a lot of attention recently is through the halo occupation distribution (HOD) formalism (e.g., see review by Cooray & Sheth 2002 and references therein). This method splits the bias problem into two steps: (1) N-body simulations are used to characterize the spatial distribution and the clustering properties of virialized dark matter halos as a function of their mass (and/or some other properties) for a given cosmology; (2) the galaxy distribution is described in terms of the probability distribution that a halo of mass M hosts N galaxies of a specified type (the HOD). The first N moments of the HOD can be measured by fitting observed N-point statistics. Using the two-point correlation function, this approach has been widely employed to estimate the mass of the host halos of galaxies and quasars at low and high redshifts (e.g., Magliocchetti & Porciani 2003; Porciani et al. 2004; Abazajian et al. 2005; Zehavi et al. 2005; Phleps et al. 2006; Zheng et al. 2007) and also to derive the mass-to-light ratio of virialized cosmic structures (e.g., Yang et al. 2005; Tinker et al. 2005; van den Bosch et al. 2007).

It is however interesting to go beyond the measurement of a (possibly scale-dependent) bias parameter from two-point statistics. Tegmark & Bromley (1999) presented evidence that the present-day galaxy biasing is nonlinear and stochastic, employing the galaxy clustering in the Las Campanas Redshift Survey. Using the 2 degree Field Galaxy Redshift Survey (2dFGRS) data, some contradictory results on the nonlinear nature of galaxy bias have been obtained. While Verde et al. (2002) found no significant evidence for nonlinearity from the bispectrum analysis, Gaztañaga et al. (2005) detect non-vanishing quadratic corrections in the three-point correlation function. Moreover, Wild et al. (2005) and Conway et al. (2005) using the count-in-cells analysis exclude the deterministic linear bias model in both the flux-limited and volume-limited (luminosity-complete) samples of galaxies and find evidence for stochasticity. Measurements of the three-point correlation function and counts-in-cells statistics for galaxy samples from the Sloan Digital Sky Survey (SDSS) suggest that galaxy biasing is nonlinear and fairly complex (Kayo et al. 2004; Nishimichi et al. 2007; Swanson et al. 2008).

The mean nonlinear biasing function of a sample of galaxies can be constrained by combining counts-in-cells measurements with models for the probability distribution function (PDF) of mass density fluctuations (SBD; Szapudi & Pan 2004). Marinoni et al. (2005) applied this technique to the first-epoch VIMOS VLT deep survey (VVDS; Le Fèvre et al. 2005) over the redshift range 0.4–1.5 on a characteristic scale R from 5 to $10\,h^{-1}$ Mpc. They conclude that galaxy bias increases with redshift and is nonlinear in all redshift bins probed. In addition, brighter galaxies are more strongly biased than less luminous ones, as well as redder galaxies are more biased than blue ones independently of redshift. However, the area covered by the VVDS used for this study was rather small (0.4×0.4 deg^2) and the results are likely affected by cosmic variance.

It is therefore very important to cross-check their robustness against richer data sets. With this spirit, in this paper we perform a similar analysis on a larger sample of high-redshift galaxies. We make use of the first ∼10,000 spectra of the zCOSMOS redshift survey (Lilly et al. 2009) to measure galaxy densities within top-hat spheres of radius 8–12 h^{-1} Mpc in the redshift range 0.4–1 (see Kovač et al. 2010a). Assuming concordance cosmology, we then use the PDF of the galaxy density contrast to estimate the mean bias function $b = b(\delta, z, R)$ between zCOSMOS galaxies and matter overdensities. Within the limits of the zCOSMOS survey, we explore the shape and the luminosity, scale, and redshift dependence of the conditional mean function $\langle \delta_g | \delta \rangle$. A careful analysis of random and systematic errors based on mock galaxy catalogs is also presented. Finally, the characteristic mass of the halos hosting zCOSMOS galaxies is inferred from the value of the linear bias parameter. The structure of this paper is as follows. We present the data used for the analysis and describe the method to reconstruct the density field in Section 2. In Section 3, we provide the details of the method which we adopt to derive the biasing function. We present the results of the tests on the mock catalogs in Section 4. Finally, we present the biasing analysis on the real data set in Section 5, comparison to the literature results in Section 6, and conclusions in Section 7.

The assumed cosmology is specified by $\sigma_8 = 0.8$, $\Omega_{m,0} = 0.25$, $\Omega_{\Lambda,0} = 0.75$, and $H_0 = 70\,\mathrm{km\,s^{-1}\,Mpc^{-1}}$. We present the obtained results scaled to the units of dimensionless h parameter, $H_0 = 100\,h\,\mathrm{km\,s^{-1}\,Mpc^{-1}}$, except of magnitudes, which are calculated with $h = 0.7$.

2. THE zCOSMOS SURVEY

2.1. The 10k Sample

zCOSMOS (Lilly et al. 2007, 2009) is a redshift survey undertaken in the field of the multiwavelength 2 deg^2 COSMOS survey (Scoville et al. 2007a), the largest contiguous mosaic ever obtained using the *Hubble Space Telescope* (*HST*)/Advanced Camera for Surveys (Koekemoer et al. 2007). The zCOSMOS-bright sample is a purely flux-limited part of the survey, selected at $I_{AB} < 22.5$. It covers the central ∼1.7 deg^2 of the COSMOS field. This corresponds to the comoving size ($\sqrt{\mathrm{Area}}$) of about 6.7, 25.1, and 54.3 h^{-1} Mpc at redshifts 0.1, 0.4, and 1, respectively, using the assumed cosmology. The zCOSMOS-bright will obtain ∼20,000 spectra of galaxies up to $z < 1.4$ with sampling expected to reach a rather uniform 60%–70%. The first set of data contains spectra for 10644 objects, about half of the final expected sample, covering a slightly smaller area of about 1.52 deg^2. The spatial sampling of these objects is quite inhomogeneous, with ∼30% on average.

This reflects the fact that the design of the observations in the zCOSMOS-bright was guided by the properties of the used VIMOS instrument. VIMOS is a multi-slit spectrograph with four quadrants of about 7×8 arcmin^2 field of view, separated by a cross of about 2 arcmin wide. The details of the observational campaign are described in Lilly et al. (2007). In summary, the targets for the spectroscopic observations in

the chosen pointings are selected randomly by the software which maximizes the number of targets per each VIMOS mask, excluding already previously selected targets (unless otherwise specified). In order to observe the contiguous area in the uniform manner, the pointings are shifted in each direction by the amount corresponding to the size of one VIMOS quadrant. To reach uniformity, an 8 pass sampling strategy is required, to be achieved with the final sample of ∼20,000 spectra. In the spatial distribution of the first part of the sample, the imprint of the VIMOS spectrograph is still in places clearly visible.

We refer to the catalog containing only objects with reliable redshift measurements from the first data set as the "10k sample" of the zCOSMOS survey. We build also the so-called "30k sample" of galaxies in the zCOSMOS survey area which satisfies the magnitude selection criteria $I_{AB} < 22.5$, but for which spectroscopic measurement is not yet available or is not of sufficient reliability. For these galaxies, we measure their photometric redshift probability function $P(z)$ using the ZEBRA code (Feldmann et al. 2006) on the 11-band photometry (e.g., Capak et al. 2007; Sanders et al. 2007) available at the time of the scientific analysis for this paper. The maximum in $P(z)$ we simply refer to as the photometric redshift. The uncertainty in the photometric redshifts which we use is estimated to be $\delta z = 0.023(1+z)$ (P. Oesch et al. 2011, in preparation) when considering all $I_{AB} < 22.5$ galaxies together. The comparison between the spectroscopic and photometric redshifts for the current sample of zCOSMOS-bright galaxies of various spectroscopic confidence classes is presented in Figure 1 in Lilly et al. (2009). There is no degradation of the quality of the photometric redshift errors $\delta z/(1+z)$ with increasing of redshift, and there is no systematic offset between the spectroscopic and photometric redshifts. Moreover, the uncertainty in the photometric redshifts for red and blue galaxies differs by only $0.004(1+z)$; it is $\delta z = 0.025(1+z)$ and $\delta z = 0.021(1+z)$ for red and blue galaxies, respectively. We will treat in this study all $I_{AB} < 22.5$ galaxies as a single sample with the uncertainty typical for all galaxies without respect of their color.

The ZEBRA code has been employed also to calculate the rest-frame magnitudes of all $I_{AB} < 22.5$ targets. The magnitudes are obtained as the best fit to the empirical set of spectral energy distribution (SED) templates normalized to each galaxy photometry (Capak et al. 2007) at the best available redshift (spectroscopic or photometric). The stellar masses are obtained by fitting stellar population synthesis models to the SED of the observed magnitudes (Bolzonella et al. 2010; Pozzetti et al. 2010).

The basic samples of all possible tracer galaxies (i.e., tracers selected only by $I_{\rm AB} < 22.5$), with both spectroscopic and photometric redshifts, are equivalent to those described in Kovač et al. (2010a, Section 4.2.1). We call tracer galaxies all the observed galaxies which are used to reconstruct the density field. For the density field reconstruction we define four types of tracer galaxies: the "flux-limited sample" of galaxies with $I_{\rm AB} < 22.5$ in $0.1 < z < 1$ and three samples of galaxies satisfying the following criteria: $M_B < -19.5 - z$, $M_B < -20 - z$, and $M_B < -20.5 - z$. The last three samples are "luminosity complete" in the $0.1 < z < 0.7$, $0.1 < z < 0.9$ and $0.1 < z < 1$ redshift bins, respectively. For the galaxies without reliable spectroscopic redshift we use their photometric redshift (ZEBRA maximum likelihood redshift) and the M_B magnitude calculated at that redshift to define the samples of tracer galaxies. The uncertainty in photometric redshift will propagate into the M_B magnitude calculation. This effect is difficult to quantify as in principle with shifting the maximum likelihood redshift the best-fit ZEBRA galaxy type can change, modifying the corresponding M_B in an unpredictable way. In practice, this error will manifest itself by randomly bringing some galaxies in and out of the luminosity samples. As we are not considering samples in the narrow bins in luminosity this will have only minor, statistically random effects on our analysis and we will neglect it.

We include the passive evolution of $\Delta M_B = -\Delta z$ in selection of the luminosity-complete samples in order to keep similar galaxies in a unique sample at every redshift. The samples are selected to be complete for galaxies of both red/early and blue/late types (see Figure 2 in Kovač et al. 2010b). As explained later, we carry out the analysis only in $0.4 < z < 1$, and the numerical characterization of the described samples of zCOSMOS galaxies (e.g., the number of galaxies, redshift limits, and volumes) is given in Table 1.

2.2. Density Field Reconstruction

For the various COSMOS projects, environment has been characterized in a few different ways. The full volume density field reconstruction has been carried out by Scoville et al. (2007b), Massey et al. (2007), and Kovač et al. (2010a). Scoville et al. (2007b) reconstruct the galaxy large-scale structure at $z < 1.1$ using photometric redshifts of galaxies down to $I_{AB} < 25$. Based on the observed shear field, Massey et al. (2007) produce maps of the large-scale distribution of dark matter, resolved in both angle and depth, up to $z = 1$. Kovač et al. (2010a) carry out the reconstruction of the density field in the zCOSMOS volume up to $z = 1$, where the main ingredients are the spectroscopic redshifts (with the uncertainty of about $100\,{\rm km\,s^{-1}}$) of galaxies with $I_{AB} < 22.5$ or subsamples of those galaxies. Moreover, Kovač et al. (2010a) present an overview of the all estimators of the continuous environment applied to the 10k zCOSMOS sample and discuss the importance of the scientific application on the exact choice of the density reconstruction method. In the following text, we will summarize the main steps in the zCOSMOS density field reconstruction method. We refer to Kovač et al. (2010a) for all the details.

Briefly, the density $\rho(\mathbf{r})$ at a given point in space $\mathbf{r}$(R.A., decl., z) can be defined as

$$\rho(\mathbf{r}) = \Sigma_i \frac{m_i\, W(|\mathbf{r} - \mathbf{r_i}|;\, R)}{\phi(\mathbf{r_i})}, \qquad (8)$$

where m_i is a weight related to some astrophysical property of an object (e.g., mass), $W(|\mathbf{r} - \mathbf{r_i}|;\, R)$ is a spatial smoothing function, and $\phi(\mathbf{r_i})$ (or $1/\phi(\mathbf{r_i})$) is a survey selection function (ideally correcting the number of observed objects to the total number of objects of the same type in a given cell). The summation in Equation (8) goes over the tracer galaxies in the relevant sample. In Kovač et al. (2010a), we discuss thoroughly the possible values/functional forms of m_i, $W(|\mathbf{r} - \mathbf{r_i}|;\, R)$ and $\phi(\mathbf{r_i})$ and a choice of tracer galaxies and their influence on the reconstructed density field.

We developed a new technique (ZADE) which allows us to incorporate both galaxies with spectroscopic and photometric redshifts in the density field reconstruction (Kovač et al. 2010a). This approach is based on modifying the photometric redshift probability function $P(z)$ of galaxies without spectroscopic redshifts based on the density of nearby (at that z) objects with reliable spectroscopic redshifts. The motivation is that galaxies are correlated on scales up to $10\,h^{-1}$ Mpc at least up to $z \sim 1$

Table 1
Properties of the zCOSMOS Samples of Galaxies Used for the Biasing Analysis

Tracers	$z_{\rm min}$	$z_{\rm max}$	$z_{\rm avg,all}$	$N_{\rm phot}$	$N_{\rm spec}$	Volume ($10^6 \times (h^{-1}\,{\rm Mpc})^3$)	ρ_N ($10^{-3} \times (h^{-1}\,{\rm Mpc})^{-3}$)	$\rho_{\rm smooth}$	l ($h^{-1}\,{\rm Mpc}$)	$l_{\rm smooth}$
Flux	0.4	1.0	0.68	14003	5085	1.89	10.11	12.61	4.62	4.61
Flux	0.4	0.7	0.56	7788	2662	0.69	15.21	18.14	4.04	3.86
Flux	0.5	0.8	0.65	7859	2925	0.86	12.48	13.57	4.31	4.25
Flux	0.6	0.9	0.74	7689	2926	1.04	10.23	10.06	4.61	4.71
Flux	0.7	1.0	0.83	6220	2423	1.20	7.20	7.08	5.18	5.35
−19.5-z	0.4	0.7	0.58	4771	1786	0.69	9.54	10.18	4.71	4.61
−20-z	0.4	0.9	0.70	6257	2363	1.44	6.01	6.00	5.50	5.51
−20-z	0.4	0.7	0.58	2909	1106	0.69	5.84	6.09	5.55	5.48
−20-z	0.5	0.8	0.67	3718	1495	0.86	6.03	6.05	5.49	5.49
−20-z	0.6	0.9	0.76	4718	1849	1.04	6.33	5.93	5.40	5.53
−20.5-z	0.4	1.0	0.75	4116	1581	1.89	3.02	2.80	6.92	7.10
−20.5-z	0.4	0.7	0.58	1475	577	0.69	2.99	2.83	6.94	7.07
−20.5-z	0.5	0.8	0.67	1864	772	0.86	3.05	2.82	6.90	7.08
−20.5-z	0.6	0.9	0.76	2399	959	1.04	3.24	2.80	6.76	7.09
−20.5-z	0.7	1.0	0.86	2642	1004	1.20	3.04	2.76	6.91	7.13

Notes. The contents of the columns are as follows. Column 1: type of the tracer galaxies; Columns 2 and 3: lower and upper redshift limits to which the statistics refers; Column 4: mean redshift of all galaxies (both with photometric and spectroscopic redshifts) within the redshift limits specified by Columns 2 and 3; Columns 5 and 6: the numbers of galaxies with photometric and spectroscopic redshifts, respectively; Column 7: volume defined by the used zCOSMOS area within $z_{\rm min}$ and $z_{\rm max}$; column 8: number density of galaxies; Column 9: mean smooth (number) density of galaxies averaged over the corresponding redshift interval; Columns 10 and 11: values of mean intergalaxy separations corresponding to the densities in Columns 8 and 9, respectively.

(e.g., Meneux et al. 2009; de la Torre et al. 2009; Coil et al. 2006), and therefore galaxies are more likely to reside at a redshift of nearby galaxies than at some other redshift. With the current quality of photometric redshifts, there are typically a few close spectroscopic structures along a given line of sight within $P(z)$. Therefore, this approach is only statistical. The exact scale on which the density field can be reconstructed without dominant systematic errors depends on the particularities of a survey in question, such as the sampling rate, the uncertainty of $P(z)$, and how representative the spectroscopic sample is of the overall population and of the part of the population with only $P(z)$.

Our analysis is based on two assumptions which are permitted given the particular characteristics of the zCOSMOS-bright survey and the ZADE method: (1) the 10k zCOSMOS spectroscopic galaxies represent a subset of galaxies which are cosmologically biased in exactly the same way as the parent 40k sample, because the selection for spectroscopic observation was completely independent of galaxy properties and because the success rate in determining a redshift was also largely independent of them, at least up to $z = 1$ (Figures 2 and 3 in Lilly et al. 2009); (2) on sufficiently large scales, the 10k spectroscopic sample traces the same structures that contain the 30k photometric galaxies, and furthermore, these structures are representative of all types of environments. We have done a number of careful checks on mock catalogs to validate this assumption. In Kovač et al. (2010a), we present a proof of the ZADE (zCOSMOS) concept, working primarily with the density field calculated using the circular apertures defined by the projected radius within $\pm 1000\,{\rm km\,s^{-1}}$. We will show in this paper (see Section 4.2) that the same approach works reliably also for the reconstruction of the so-called three-dimensional densities on larger scales.

In practice, we use counts of objects from the spectroscopic 10k sample in spheres of radius $R_{\rm ZADE}$ along the line of sight to the 30k objects in order to redistribute their ZEBRA-calculated $P(z)$ into new, ZADE-modified, $P_{\rm ZADE}(z)$. In this way, the probability $P(z)$ of a particular galaxy is increased at the redshift of a nearby galaxy with a spectroscopic redshift. In modifying the $P(z)$ of the galaxies with photometric redshift, we use all $I_{AB} < 22.5$ spectroscopic galaxies. The redshifts of the spectroscopic galaxies, and the modified $P_{\rm ZADE}(z)$, can then be used to reconstruct the density field, with various filters and various samples of tracer galaxies, and in particular for various luminosity-complete samples. It might be thought logical to repeat the $P(z)$ modification process using only spectroscopic galaxies with exactly the same luminosity selection, but in practice we find, from tests based on the mock catalogs, that this introduces negligible gain at the cost of increased Poisson noise. We find that for the 10k zCOSMOS sample, a density field reconstruction with $R_{\rm ZADE} = 5\,h^{-1}\,{\rm Mpc}$ produces a density field on various scales without a dominant systematic error for a broad range of overdensity values in $0.1 < z < 1$ (see Section 4.2 and also Figure 6 in Kovač et al. 2010a). While the systematic reconstruction error is changing with redshift (e.g., it increases with redshift for the flux-limited sample of galaxies in the underdense regions; Figure 6 in Kovač et al. 2010a), our main point is that the relative systematic effect is rather small, and using the mock catalogs it can be quantified and corrected for.

When calculating densities of the tracer galaxies, tracers with spectroscopic redshift are counted as one (i.e., δ-function) at their measured redshifts, and the tracers with only photometric redshifts are counted as fractional objects according to the $P_{\rm ZADE}(z)$ value at the redshift of consideration z (see also Equation (9) below). Formally, the ZADE approach is equivalent to $\phi(\mathbf{r_i}) = 1$ for every tracer galaxy in Equation (8). This means that in the ZADE approach the mean intergalaxy separation in a statistical sense is the characteristic separation of the total population of that sample of tracer galaxies, and is therefore smaller than for some incomplete set of tracers, which is important in suppressing the effects of shot noise.

The ZADE approach should be seen as a practical approach to the problem of incomplete and inhomogeneous sampling present in many spectroscopic surveys. Ultimately, the justification for using ZADE is that, in tests on realistic mock catalogs, it has been shown to be superior to the commonly used weighting of galaxies with spectroscopic redshift with the inverse of the spatial sampling (Kovač et al. 2010a). Some of the details in a given implementation are of course arbitrary, e.g., the choice of $R_{\rm ZADE}$, but it has been shown that the outcomes do not depend sensitively on these around the values used here. Following the same lines, though it would seem natural to choose the cylindrical smoothing in the ZADE modification of $P(z)$, as all of the measurements are in the redshift space, we use the ZADE smoothing to be spherical as it has only one free parameter and the tests on the mocks have confirmed that already this simple approach works well enough. Moreover, it should be understood that while the idea behind the ZADE approach is clearly physical (i.e., clustering of galaxies), the exact implementation of the method has been done by optimizing the set of reasonable parameters on the realistic mock catalogs, not attempting to justify the details analytically.

For the biasing analysis in this paper, the density is estimated by counting galaxies within a spherical top-hat filter $W(|\mathbf{r}-\mathbf{r_{ij}}|; R)$ with smoothing scale $R = R_{\rm TH}$, following

$$W(\left|\mathbf{r}-\mathbf{r_{ij}}\right|; R) = \begin{cases} \dfrac{1}{\frac{4}{3}\pi R_{\rm TH}^3} P_{i,\rm ZADE}(z_j) & \text{if } |\mathbf{r}-\mathbf{r_{ij}}| \leqslant R_{\rm TH} \\ 0 & \text{otherwise.} \end{cases} \tag{9}$$

In the equation above, $|\mathbf{r}-\mathbf{r_{ij}}|$ is the three-dimensional distance between a tracer galaxy i at a position $\mathbf{r_{ij}}$ and the point $\mathbf{r}$ where the density is estimated. As discussed above, this equation is applied to all galaxies in the sample of tracer galaxies. For a galaxy i with reliable spectroscopic redshift we take that $P_{i,\rm ZADE}(z_j) = 1$ at z_j being the spectroscopic redshift of that galaxy. At all other redshifts it is zero. For a galaxy i with photometric redshifts only their spatial position R.A.$_i$ − decl.$_i$ is fixed, while their position along the z-direction is specified by the probability $P_{i,\rm ZADE}(z_j)$ to be at some redshift z_j. Therefore in practice one needs to sum Equation (8) over the 10k galaxies with reliable spectroscopic redshift and 30k × $N_{\rm bin}$ "probabilistic galaxies" where $N_{\rm bin}$ corresponds to the number of redshift bins to which $P(z)$ is interpolated. We have chosen these bins to be 0.002, which is even at the highest redshift in our analysis ($z = 1$) still about three times the spectroscopic redshift uncertainty.

The zCOSMOS selection catalog is based on the 0.1 arcsec resolution *HST* images in the F814W filter (Koekemoer et al. 2007), supplemented by photometry from a high-resolution Canada–France–Hawaii Telescope (CFHT) image in the i filter in the case when the *HST* data are missing or when the *HST* photometry is not of required quality. The fraction of targets added from the CFHT photometry is less than 0.5% away from the extreme edges of the COSMOS survey. Moreover, with this combination of underlying imaging only a negligible part of the zCOSMOS area is affected by the foreground stars (Lilly et al. 2009), and there is no need for masking some regions for the density field reconstruction. For galaxies without ZEBRA $P(z)$, we use instead the overall smoothed $N(z)$ normalized to 1 in $0.1 < z < 1.4$ (see Kovač et al. 2010a for more details).

We express the reconstructed density field in terms of the dimensionless density contrast $\delta(\mathbf{r})$ (also commonly referred to as "overdensity") defined as

$$\delta(\mathbf{r}) = \frac{\rho(\mathbf{r}) - \rho_m(z)}{\rho_m(z)}. \tag{10}$$

Here $\rho_m(z)$ is the mean density at redshift z, which we calculate as the volume average. For a point $\mathbf{r}$ in which a part of the cell defined by the smoothing scale R of a filter W falls outside of the survey limit, we apply an edge correction by scaling the measured density with the fraction f_e of the cell which is inside of the geometrical limits of the survey, such that the corrected density is ρ/f_e. For analysis, we use only the cells for which at least half of the volume is within the survey limits.

We estimate $\rho_m(z)$ for the four samples of tracer galaxies defined in Section 2.1 by adding up statistical contributions of all zCOSMOS tracer galaxies at each redshift z in the range $0.05 < z < 1.4$. For practical purposes redshift is quantified in bins each $\Delta z = 0.002$ wide. We require that galaxies satisfy the flux or luminosity limit in order to use them to calculate the mean density of that particular sample. For the mean density calculation, we use only the photometric redshifts (i.e., the maximum in $P(z)$) for all galaxies in the whole 10k+30kZADE sample, as the resulting mean density does not change significantly when using spectroscopic redshifts instead of the photometric redshifts for the 10k galaxies. The contribution of any tracer galaxy (included in the sample based on its photometric redshift in this calculation) to the mean density at some z in a given sample, up to $z_{\rm max}$, is calculated as $m_i \Delta V(z)/V_{\rm max}$, where $\Delta V(z)$ is the volume of the individual redshift bin and $V_{\rm max}$ is the volume of the zCOSMOS survey limited by $z_{\rm max}$. The redshift $z_{\rm max}$ corresponds to the highest redshift up to which a tracer galaxy of consideration (i.e., of a given luminosity) can still be detected in an $I_{AB} < 22.5$ survey. m_i is a weight of a galaxy (e.g., unity, L_B or M_*). Effectively, at some redshift z:

$$\rho_m(z) = \Sigma_i \frac{m_i \Delta V_i(z)}{V_{\rm max,i}}, \tag{11}$$

where the summation is carried over the sample of tracer galaxies available at that z. In the calculation, we take the passive evolution into account by modifying the luminosities as above ($\Delta M_B = -\Delta z$), using the K-correction for the individual galaxies obtained from the ZEBRA code. Essentially, calculation of the K-correction is based on the difference between the colors of the best-fit SED template of that galaxy at zero and its assigned redshift.

The resulting smooth (unity-weighted) $\rho_m(z)$ functions for the four samples of tracer galaxies are shown in Figure 1. As we are adding contributions of all galaxies in $0.05 < z < 1.4$ satisfying the flux or luminosity criteria to calculate the mean densities for each of the samples of tracer galaxies, the mean density is not zero outside of the redshift limits in which the tracers galaxies make the luminosity complete samples. For comparison, we also plot the actual number density in 0.05 redshift bins. It is obvious that, even in a survey of the area of the zCOSMOS, the density is dominated by inhomogeneities in the redshift distribution of galaxies of $\Delta z \sim 0.1$. On the other hand, the procedure described above to calculate $\rho_m(z)$ smooths the peaky distribution of the observed tracer galaxies, producing a mean volume density of luminosity-complete tracer galaxies that is almost constant with redshift.

The measured volume properties of the four samples of tracer galaxies are included in Table 1. Obviously, the value of

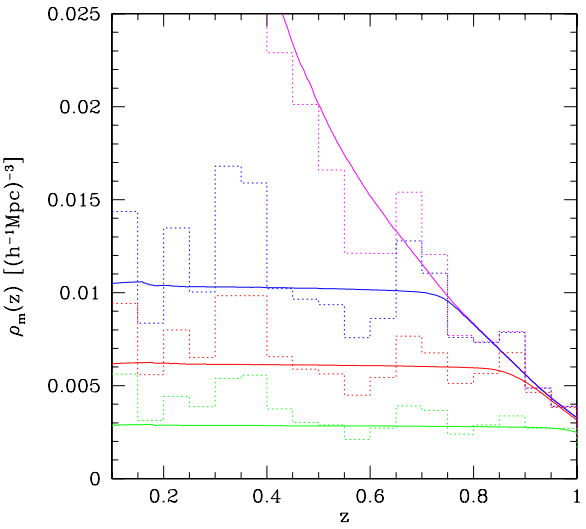

Figure 1. Unity-weighted ($m_i = 1$) mean volume density of the zCOSMOS tracer galaxies in $0.1 < z < 1$. The dotted lines are the mean volume densities of the zCOSMOS tracer galaxies obtained by dividing the number of galaxies with volume corresponding to redshift bins of 0.05. The continuous lines are smoothed mean densities, obtained by adding $\Delta V(z)/V_{\rm max}$ contributions of each tracer galaxy in redshift bins 0.002 wide. The magenta, blue, red, and green curves are for the flux-limited, and $M_B < -19.5 - z$, $M_B < -20 - z$ and $M_B < -20.5 - z$ luminosity-complete samples, respectively. See the text for more details.

the mean density is a fair representation only of the universe sampled by the zCOSMOS survey and may not be a true universal value. We include the uncertainty in the mean density in our error budget, as estimated from the mock catalogs.

3. MEASURING THE BIASING FROM THE OBSERVATIONAL DATA

A number of methods to measure the nonlinear biasing from the observed data have been proposed. Szapudi (1998) suggested to use the cumulant correlators of the observed distribution of galaxies in redshift surveys; Matarrese et al. (1997) and Verde et al. (1998) derived the first two Taylor coefficients of the biasing function from the bispectrum of galaxies from the survey. SBD proposed a method, tested on simulations, to measure the mean biasing function relating the cumulative distribution functions (CDFs) of the density fluctuations of galaxies and mass.

In this work, we follow the method developed by SBD to derive the mean biasing function $b(\delta)$ (or more specifically the conditional mean function $\langle\delta_g|\delta\rangle$) and its second moments, over the redshift interval 0.4–1.0. Here, we summarize the main points and limitations of the SBD method and refer the interested readers to the original paper for all the details.

We denote the CDFs of the density fluctuations for galaxies and for the underlying dark mass as $C_g(\delta_g)$ and $C(\delta)$, respectively. Both distributions are functions of the scale and redshift at which the density contrast is estimated and $C_g(\delta_g)$ will also depend on the type of tracer galaxies used to reconstruct the overdensity field. Assuming that the biasing relation between galaxies and mass is deterministic and monotonic, the biasing function may be estimated from the inverse CDF of galaxies at a given value (percentile) of the CDF of mass (SBD):

$$\delta_g(\delta) = C_g^{-1}[C(\delta)], \tag{12}$$

where $C_g^{-1}[\cdots]$ denotes the inverse CDF of the galaxy distribution. SBD used simulations to show that Equation (12) can successfully reproduce the true conditional mean function $\langle\delta_g|\delta\rangle$ over the broad range of δ probed, overestimating it slightly in the most dense regions. The error in δ_g due to the method is small with comparison to the scatter in the overdensity field itself. SBD also conclude that the assumption of the monotonicity of $\langle\delta_g|\delta\rangle$ is valid (or represents a very good approximation) on scales of a few Mpc, which are the scales over which the biasing is measured in practice. The errors on the second moments are of the order of a few percent.

3.1. PDF of Density Contrast of Galaxies and Mass

Current galaxy redshift surveys provide data to calculate the galaxy density contrast and its PDF with sufficient accuracy up to redshifts of about 1.5 (e.g., Marinoni et al. 2005). Obtaining the mass density contrast observationally is on the other hand an extremely difficult task. Direct reconstruction has been possible using galaxy peculiar velocities as tracers of mass fluctuations so far only in the local universe (out to $\sim 100\,h^{-1}$ Mpc; Dekel et al. 1990, 1999; Dekel 2000) or using weak lensing up to $z \sim 1$ (Massey et al. 2007), although with much lower resolution in the redshift dimension than is obtained for the galaxy density field from the galaxy redshift surveys. From a theoretical point of view it has been shown that in comoving space, the density contrast δ of matter follows, to a good approximation, a lognormal distribution $p(\delta)$ (Coles & Jones 1991). In this paper we will use this theoretical approximation of the matter distribution and in the following text, we will summarize the theoretical development necessary to calculate the PDF of the matter. We want to add at this place that there is a project in development to simultaneously use galaxy and matter density field (the latter one reconstructed from the weak lensing shear maps) in the COSMOS volume to estimate bias directly from the observed data.

Following SBD, the lognormal distribution of the matter fluctuations can be expressed as

$$p(\delta)_R = \frac{\left(2\pi\omega_R^2\right)^{-1/2}}{1+\delta}\exp\left\{-\frac{\left[\ln(1+\delta)+\omega_R^2/2\right]^2}{2\omega_R^2}\right\}. \tag{13}$$

In the last equation, the parameter ω_R^2 is defined as

$$\omega_R^2 = \ln[1 + \langle\delta^2\rangle_R], \tag{14}$$

where δ is directly related to the variance $\sigma_R^2(z)$ of the density contrast field at redshift z via

$$\langle\delta^2\rangle_R = \sigma_R^2(z) \tag{15}$$

given that the density contrast field has zero mean. In the equations above, the index R denotes the smoothing scale at which the density field is reconstructed. The value of σ_R on a given scale is determined by the adopted cosmology. For the smoothing scales R which are large enough to be in the linear regime, its evolution with redshift can be modeled as

$$\sigma_R(z) = \sigma_R(z=0)D(z), \tag{16}$$

where $D(z)$ is the linear growth factor of density fluctuations, normalized to unity at $z = 0$. For smaller scales, one would need nonlinear corrections.

Given that the derived lognormal form of the PDF of the matter overdensity field is calculated in real (comoving) space

and that the PDFs from surveys are obtained in redshift space, one has to convert both functions to the same space. If the redshift distortion affects both galaxies and matter in a similar way, we can expect that the mean biasing function $b(\delta)$ and the conditional mean function $\langle\delta_g|\delta\rangle$ in z space will be similar to the one in real space:

$$\langle\delta_{g,z}|\delta_z = \delta\rangle = \langle\delta_g|\delta\rangle. \quad (17)$$

SBD show that the PDF (or CDF) of the mass density contrast in redshift space can also be well described with the lognormal function (Equation (13)), with standard deviation obtained in redshift space. The relation between the azimuthally averaged standard deviations of mass fluctuations in real $\sigma_R(z)$ and redshift $\sigma_R^z(z)$ comoving space at high redshift is (e.g., SBD)

$$\sigma_R^z(z) = \left[1 + \frac{2}{3}f(z) + \frac{1}{5}f^2(z)\right]^{1/2}\sigma_R(z) \quad (18)$$

based on the expression derived by Kaiser (1987). For these calculations, we use the relation between the growth rate f and the growth factor D given by

$$f(\Omega_m(z), \Omega_\Lambda(z)) = \frac{d\ln D}{d\ln a} = -1 - \frac{\Omega_m(z)}{2} + \Omega_\Lambda(z) + \frac{5\Omega_m(z)}{2g(z)}, \quad (19)$$

where $a = (1+z)^{-1}$ and

$$D(z) = \frac{g(z)}{g(0)(1+z)} \quad (20)$$

for linear fluctuations (Carroll et al. 1992) and

$$g(z) \approx \frac{5}{2}\Omega_m(z) \times \left[\Omega_m^{4/7}(z) - \Omega_\Lambda(z) + \left(1 + \frac{\Omega_m(z)}{2}\right)\left(1 + \frac{\Omega_\Lambda(z)}{70}\right)\right]^{-1}. \quad (21)$$

In the literature, there are other approximations available for the growth rate f at different redshifts. For example, Lahav et al. (1991) derived $f \approx \Omega_m(z)^{0.6}$ and Wang & Steinhardt (1998) derived $f \approx \Omega_m(z)^{0.55}$, the latter one allowing the possibility that the current accelerated phase of the universe is due to quintessence (a time-evolving, spatially inhomogeneous component with negative pressure) and not due to the cosmological constant.

Following the framework outlined above, we use Equation (12) to derive the $\langle\delta_g|\delta\rangle$ function and Equations (6) and (7) to derive its second moments. We calculate the CDF of mass and galaxies in the redshift space. The CDF of galaxies is calculated from the reconstructed galaxy density field based on Equations (8)–(11). The CDF of mass is given by the lognormal distribution (Equation (13)) using $\sigma_R^z(z)$ instead of $\sigma_R(z)$ in Equation (15) (and Equation (14)). The value of $\sigma_R^z(z)$ is calculated for the specified cosmology (given at the end of Section 1) following Equations (16) and (18)–(21). For the calculations of the biasing parameters, mean sums (i.e., denominators in Equations (6) and (7)) are normalized by the corresponding $\sigma_R^z(z)^2$ (in the redshift space). We follow this procedure for the calculations of $\langle\delta_g|\delta\rangle$ and its biasing parameters for both the real data and mock catalogs.

4. ERRORS IN THE MEAN BIASING FUNCTION AND BIASING PARAMETERS

The mean biasing function (or the conditional mean function $\langle\delta_g|\delta\rangle$) and its moments, which are derived using the method described in Section 3, will contain uncertainties due to the finite volume of the survey (i.e., cosmic variance errors), the use of discrete objects to trace the continuous density field (shot noise errors), plus any errors related to the observational construction of the density field from a realistic galaxy sample (reconstruction errors). Our philosophy in this paper is to use mock catalogs to gain an understanding of the effects of these, to estimate the size of random uncertainties and, where possible, to correct for any systematic effects introduced. Although the specific set of mocks that we use represents only one particular implementation of cosmology and galaxy modeling, which is unlikely to be absolutely correct, the effects of the above three sources of observational measurement error should be the same as in any analysis of our own universe. We can isolate cosmic variance by comparing the same measurements made on independent mocks, and can isolate reconstruction effects (both random and systematic) by comparing the differences between the measurements on the same mocks with and without applying the selection function. The effects of shot noise are clearly intrinsically linked to the ratio of the smoothing scale and the mean intergalaxy separation and may therefore produce effects with, e.g., galaxy luminosity that do not have a physical origin. This effect can be simulated by randomly resampling smaller fractions of the total population of galaxies.

The mock catalogs which we employ are based on the COSMOS light cones kindly provided by Kitzbichler & White (2007). These are built from the N-body Millennium Simulation (Springel et al. 2005) in which $\Omega_m = 0.25$, $\Omega_b = 0.045$, $h = 0.73$, $\Omega_\Lambda = 0.75$, $n = 1$, and $\sigma_8 = 0.9$. The semi-analytic modeling of galaxy properties is based on De Lucia & Blaizot (2007) with some modifications described in Kitzbichler & White (2007). It should be noted that these mocks are realistic enough that basic galaxy properties such as luminosity distributions (Kitzbichler & White 2007) and clustering (Meneux et al. 2009) are quite well matched to observational data. There are 24 mock catalogs covering a field $1.^\circ4 \times 1.^\circ4$ and going down to $r \leqslant 26$ mag that are independent in the sense that, although they are based on a single very large volume, individual galaxies and large-scale structures appear at quite different redshifts in the different light cones. We randomly choose 12 of these mock catalogs for our tests. We use only an area and redshift range matching the zCOSMOS-bright survey and select galaxies with different flux or luminosity limits as required.

In analyzing the mock catalogs, we reconstruct the overdensity field on a grid with a separation of $0.5\,h^{-1}$ Mpc in the R.A.–decl. plane and 0.002 in the z-direction. As with the real data, we use every tracer galaxy to reconstruct the density field, using either its spectroscopic redshift or a simulated ZADE-modified $P(z)$ probability distribution. As above, this is equivalent to $\phi_i = 1$ for every tracer galaxy following notation of Equation (8). We limit ourselves to the use of the unity-weighted overdensities, i.e., $m_i = 1$ in the same equation.

In deriving bias parameters for the mock catalogs, we have chosen to use a value of $\sigma_8 = 0.8$, consistent with the latest *Wilkinson Microwave Anisotropy Probe* results (Dunkley et al. 2009), even though the mock catalogs themselves were constructed from cosmological simulations with $\sigma_8 = 0.9$. We want to use the better σ_8 value for the actual analysis, and by

using the preferred $\sigma_8 = 0.8$ in the analysis also on the mock catalogs we obtain the errors which can be directly applied to the data. This means that the values of the biasing parameters of mock galaxies estimated here are not the real values. We are not, of course, interested in the cosmological bias in the mocks, but rather, only in what the uncertainties are, so this change should be immaterial. Additional tests on the mock catalogs carried out for one type of tracer galaxies ($M_B < -20 - z$) and one smoothing radius ($R_{\rm TH} = 8\,{\rm Mpc}\,h^{-1}$) only confirm that this is indeed the case. The difference between the mock estimated errors in the $\langle\delta_g|\delta\rangle$ function which we quantitatively apply to the zCOSMOS data (cosmic variance and reconstruction errors, discussed in the following sections) derived with $\sigma_8 = 0.8$ and $\sigma_8 = 0.9$ is negligible.

Nevertheless, it is important to note that the difference between the assumed and mock σ_8 values of 0.1 causes only small differences in the biasing values themselves (i.e., SBD). The exact change in the biasing parameters is quantified later in Section 5, where we also show that the effect of changing the assumed σ_8 parameter on the conditional mean $\langle\delta_g|\delta\rangle$ function for the actual data is small (Figure 14).

As in other analyses, we choose a logarithmic representation of the conditional mean $\langle\delta_g|\delta\rangle$ function in terms of $1 + \delta$ and $1 + \delta_g$ variables, in order to emphasize the behavior in the underdense regions. For simplicity, we will refer to the conditional mean function of $\log(1 + \delta_g)$ at a given $\log(1 + \delta)$ also as $\langle\delta_g|\delta\rangle$.

4.1. Cosmic Variance

One of the main uncertainties in the biasing analysis comes from the finite survey volume and the consequent noise in $C_g(\delta_g)$. This random uncertainty is usually termed cosmic (or sample) variance. To isolate and quantify this effect, we use the 12 mock catalogs and assume that all $I_{AB} < 22.5$ galaxies have reliably measured redshifts (the so-called 40k mock catalogs). The different subsamples of tracer galaxies are then selected using the same luminosity and redshift criteria as for the real zCOSMOS galaxies.

It is not practical to use exactly the same method to estimate the mean density of galaxies as in zCOSMOS, because we cannot reliably assign a detailed SED to each galaxy. Rather, we estimate this directly from the mock catalog using a smoothing kernel that closely approximates the $V/V_{\rm max}$ procedure for the data. Specifically, to get the mean density in the flux-limited samples we use the iterative boxcar smoothing in redshift with the width of the smoothing kernel from $\Delta z = 0.04$ to $\Delta z = 0.02$. For the luminosity-complete samples (which should have roughly constant number density) in some redshift interval Δz, we use the number density of galaxies in the same bin broadened by 0.05 at each end (except for the $M_B < -20 - z$ sample in $0.8 < z < 0.9$ where to obtain mean density we count galaxies in $0.75 < z < 0.9$). As we are calculating the mean density for the different mock catalogs separately for each mock catalog, the uncertainty arising from the $\rho_m(z)$ value should also propagate through to our estimate of the bias.

We then compute the bias on the 40k mock overdensity fields following the procedure as described in Section 3. As an example, we show in the lower panel in Figure 2 the conditional mean functions $\langle\delta_g|\delta\rangle$ obtained for all 12 mock catalogs, where the mock galaxy density field has been constructed with the flux-limited sample of galaxies and the top-hat filter of $10\,h^{-1}$ Mpc in $0.4 < z < 0.7$ (we will explain in Section 4.2 the reason for using smoothing filter of $10\,h^{-1}$ Mpc). Because of the cosmic variance, there is a dispersion of the δ_g values associated with

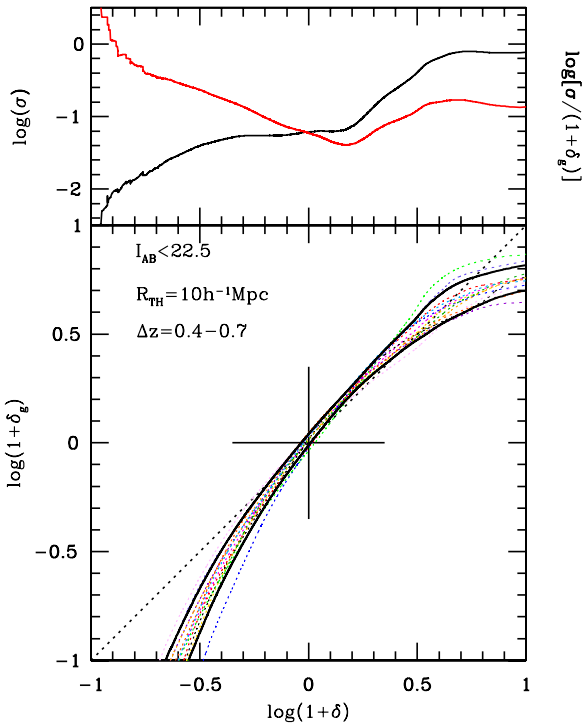

Figure 2. Effect of the cosmic variance errors on the conditional mean function $\langle\delta_g|\delta\rangle$. At every δ value, cosmic variance is causing a spread in the corresponding δ_g values. Lower panel: the $\langle\delta_g|\delta\rangle$ functions are obtained from the 12 mock catalogs, plotted as the thin dotted curves, where the mock galaxy density field has been reconstructed with the flux-limited sample of galaxies and the top-hat filter of $10\,h^{-1}$ Mpc in $0.4 < z < 0.7$. In all figures containing the $\langle\delta_g|\delta\rangle$ function, starting with this, we mark the case of a no-biasing (i.e., linear bias $b_L = 1$) with the black dotted straight line. The cross in the middle of the panels is drawn for a reference and marks the $\delta_g = \delta = 0$ case. The standard deviation σ of δ_g values in the mocks at every δ is plotted with the thick continuous lines, centered at δ_g obtained by averaging 12 mock values. Upper panel: the value of the standard deviation σ of δ_g values in the mocks plotted below at every δ (black curve). This is the effective cosmic variance noise expected in a single reconstruction, i.e., in the actual corresponding data sample. The same σ scaled by $(1 + \delta_g)$, with δ_g obtained by averaging 12 mock values at the same δ, is presented with the red curve.

every δ value, since every mock will uniquely map δ to a single (mean) δ_g value. A similar effect is seen for the other samples of tracer galaxies and in the other redshift bins.

We plot the corresponding standard deviation σ of $\delta_g(\delta)$ values at each δ in the upper panel of Figure 2 as the black curve. For the presentation, the matter overdensity is given on a $\log(1 + \delta)$-axis, and the cosmic variance errors are given on a log-axis (these are not errors on the logarithmic values; the corresponding ordinate for the black curve is labeled on the left-hand side). As discussed later, these σ values are the exact values for the cosmic variance errors on $\delta_g(\delta)$ adopted for the equivalent set of zCOSMOS data. For an easier interpretation of the influence of cosmic variance errors on our analysis, we also plot in the upper panel of Figure 2 as the red curve the same cosmic variance errors scaled by $(1 + \delta_g)$ (plotting again their log values, the corresponding ordinate is labeled on the right-hand side). The δ_g value used for the scaling is the mean of the 12 corresponding mock values obtained at the same δ marked on the abscissa. We also mark the $\pm 1\sigma$ region on the $\langle\delta_g|\delta\rangle$ function with the thick black lines in the lower panel of Figure 2, plotting these errors on the mock-averaged $\delta_g(\delta)$ value, averaging at the same δ (the errors are properly scaled for the representation of galaxy overdensities on the $\log(1 + \delta_g)$ axis). From the red curve in the upper panel, as well as from the thick

black lines in the bottom panel, it is obvious that due to the cosmic variance, the relative uncertainty in the measured range of possible $\delta_g(\delta)$ values is largest in the most underdense regions, then it gets smaller toward regions near the mean density, and it rises again and finally flattens in the most overdense regions. Not surprisingly, the effects of cosmic variance are seen most strongly in the rarest environments.

4.2. Reconstruction Errors

The reconstructed galaxy density field is supposed to be a faithful representation of the density field that would ideally be obtained from full knowledge of the population of tracer galaxies. In practice, this will not be perfect, and we refer to "reconstruction errors" as those errors which arise due to this. We can estimate these by constructing and comparing the conditional mean function $\langle\delta_g|\delta\rangle$, and thereby the biasing parameters, in each of the 12 mock fields using both the full 40k sample (assumed to have perfectly known redshifts) and a simulation of the 10k+30kZADE catalogs. The 40k mock catalogs are the same catalogs as described in the previous section (Section 4.1) already used to estimate the cosmic variance errors. The 10k+30kZADE catalogs are created from the 40k catalogs to resemble as close as possible the real 10k+30kZADE zCOSMOS sample. These catalogs match the geometrical limits and spatially inhomogeneous sampling of the zCOSMOS spectroscopic survey and contain ~10,000 galaxies with $15 < I_{AB} < 22.5$ and known spectroscopic redshifts, while the rest of the galaxies are assigned photometric redshifts.

As the spatial sampling pattern of the 10k sample is very inhomogeneous, we create the 10k+30kZADE mock catalogs by imposing on the 40k mock catalogs the spatial sampling that arises from the incomplete tiling of the 10k sample, described in Section 2.1. We start from the 10k catalogs of mock galaxies with spectroscopic redshifts produced by Knobel et al. (2009). These mock catalogs have already been used in various degrees in the previous 10k zCOSMOS scientific analyses (e.g., in galaxy groups analysis by Knobel et al. 2009, clustering analyses by Meneux et al. 2009 and de la Torre et al. 2011; see also the detailed paper on the galaxy density field reconstruction by Kovač et al. 2010a). They were constructed as follows. First, only galaxies satisfying a magnitude selection $15 < I_{AB} < 22.5$ were selected (making a small adjustment to the magnitudes so as to match the observed number counts—see Figure 1 in Knobel et al. 2009). As a second step, the spatial sampling rate (see Figure 4 in Lilly et al. 2009) and the redshift success rate of the 10k zCOSMOS sample (Lilly et al. 2007, 2009) were imposed by removing galaxies from the mocks following the probability that a galaxy at a given R.A. − decl. position and redshift would have been observed in the 10k sample.

We then assign photometric redshifts to the rest of the 40k mock galaxies, which were not "10k observed." The photometric redshift probability distribution $P(z)$ is taken to be a Gaussian distribution with $\sigma = 0.023(1 + z)$, with the central value randomly shifted in redshift using offsets selected from the same distribution. For the density field reconstruction this probability is then modified using the usual ZADE algorithm to yield $P_{\rm ZADE}(z)$ (see Section 2.2), digitized in increments of 0.002 in redshift. We do not incorporate the $\sim$100 km s^{-1} velocity uncertainty of the spectroscopic galaxies (equivalent to $0.00036(1 + z)$, see Lilly et al. 2009) as this is negligible compared with radial dimension of the three-dimensional sampling sphere. We should stress that the point of this test is simply to see the gross effects of using the ZADE approach to reconstruct the density field, with good approximations to the spatial sampling and to the photometric redshift accuracy.

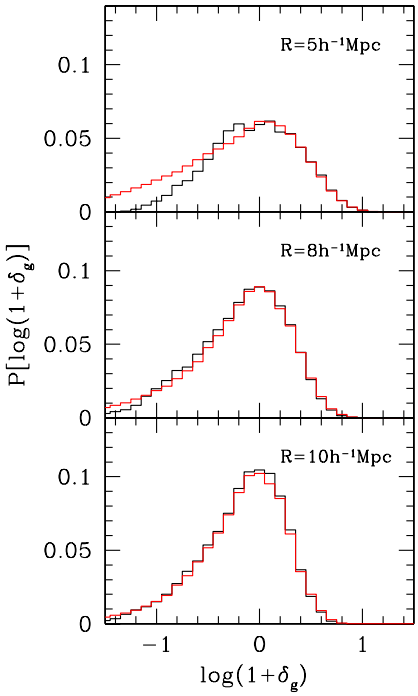

Figure 3. Example of the PDF of the galaxy density contrast field in $0.4 < z < 1$ using one mock catalog. The density field is reconstructed using the top-hat smoothing filter of 5, 8, and 10 h^{-1} Mpc going from the top to the bottom panel. The black histogram corresponds to the reconstruction with the 40k catalog (every galaxy has a measured spectroscopic redshift) and the red histogram corresponds to the reconstruction with the 10k+30kZADE catalog (10k-like sample of galaxies with a measured spectroscopic redshift, the rest of the $I_{AB} < 22.5$ galaxies have the ZADE-modified photometric redshift). Binning is carried out in $\log(1+\delta_g)$ units. At the current status of the zCOSMOS survey, we need scales of at least 8 h^{-1} Mpc to reconstruct the density field for the biasing analysis with acceptable errors at every δ_g up to $z \sim 1$.

The combination of the 10k sample of galaxies with spectroscopic redshifts (adopted from Knobel et al. 2009) and the rest of the galaxies from the 40k sample with the $P_{\rm ZADE}(z)$ makes the 10k+30kZADE catalog. The reconstructed overdensity field in the 10k+30kZADE mocks has been normalized using the same mean densities as computed for the corresponding samples in the 40k catalogs, described in Section 4.1.

As discussed in Kovač et al. (2010a), although the ZADE approach is overall better than traditional weighting schemes, the use of photometric redshifts tends to "fill in" small-scale low-density regions. Figure 3, in which we plot the PDFs of the reconstructed density contrast for the 40k and 10k+30kZADE samples in $0.4 < z < 1$ for a representative mock catalog, shows that this is a significant effect for $R_{\rm TH} = 5\,h^{-1}$ Mpc, but is small at and above $R_{\rm TH} = 8\,h^{-1}$ Mpc, and we limit our analysis to these scales.

To examine more directly the effects of reconstruction on the biasing analysis, we plot in Figures 4 and 5, for all 12 mocks, the differences between the conditional mean $\langle\delta_g|\delta\rangle$ functions that are computed for the 10k+30kZADE and 40k mocks, as a function of δ. Figure 4 is constructed using the flux-limited $I_{AB} < 22.5$ sample for $0.4 < z < 1$ with four overlapping $\Delta z = 0.3$ bins, and Figure 5 shows the luminosity-complete $M_B < -20 - z$ samples covering $0.4 < z < 0.9$ with three overlapping $\Delta z = 0.3$ bins. Both figures show the results only for an 8 h^{-1} Mpc smoothing radius.

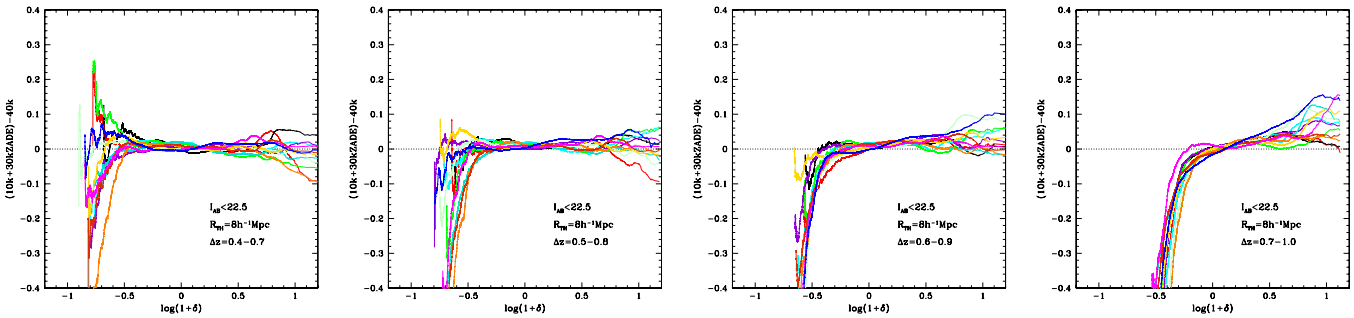

Figure 4. Reconstruction error in the conditional mean function $\langle \delta_g | \delta \rangle$ for the flux-limited individual mock samples. Reconstruction error is defined as the difference between the 10k+30ZADE and 40k mock $\langle \delta_g | \delta \rangle$ values at a given δ. The results are obtained for 12 sets of mock catalogs with tracers $I_{AB} < 22.5$ and smoothing $R_{\rm TH} = 8\,h^{-1}$ Mpc. The analysis is carried out in four overlapping $\Delta z = 0.3$ bins covering $0.4 < z < 1$, indicated in the right-hand corner in each of the panels. Each curve of different color corresponds to the measurement in one mock.

(A color version of this figure is available in the online journal.)

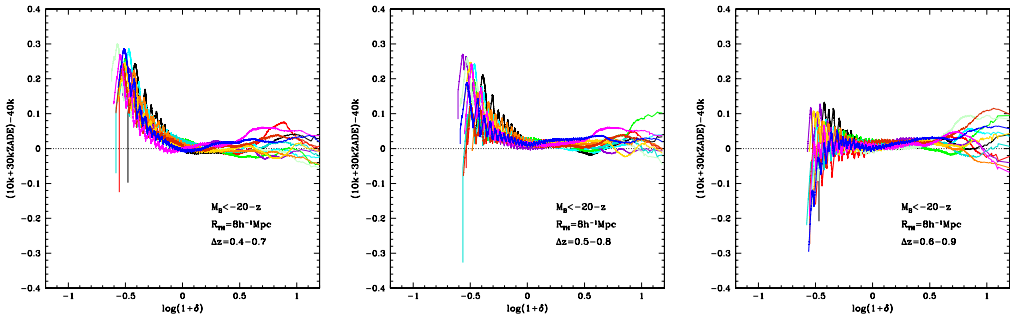

Figure 5. Reconstruction error in the conditional mean function $\langle \delta_g | \delta \rangle$ for the luminosity-complete individual mock samples. The curves have the same meaning as in Figure 4. The results are obtained with tracers $M_B < -20 - z$ in three overlapping $\Delta z = 0.3$ bins covering $0.4 < z < 0.9$.

(A color version of this figure is available in the online journal.)

If there was no reconstruction error, i.e., if the 10k+30kZADE reconstruction was a perfect representation of the actual 40k density field, then each line in these figures would be flat at a value of zero. The scatter in the 12 curves in these two figures therefore shows the random component of the reconstruction error, while any average offset from zero of those 12 curves corresponds to a systematic error in the $\langle \delta_g | \delta \rangle$ function.

The effects of systematic reconstruction error are shown in the lower panels of Figures 6 and 7, which display the $\langle \delta_g | \delta \rangle$ functions from the 10k+30kZADE and 40k mocks, obtained by averaging the $\langle \delta_g | \delta \rangle$ functions from the 12 mocks (the 40k mock averages are shown in black, the 10k+30kZADE averages are shown in violet). The results are obtained with the flux (Figure 6) and $M_B < -20 - z$ (Figure 7) limited samples of galaxies, both with $R_{\rm TH} = 8\,h^{-1}$ Mpc smoothing. In the upper panels of Figures 6 and 7 we show the corresponding rms values (σ) of the average $\langle \delta_g | \delta \rangle$ from the 12 mocks, as a function of δ. These σ values therefore correspond to the cosmic variance in the reconstructions of the galaxy density field with the 40k (black) and 10k+30kZADE (violet) samples. In addition, we show also the random component of the reconstruction error (green), obtained as the standard deviation $\sigma_{\rm rec}$ of the differences between the 10k+30kZADE and 40k mock $\langle \delta_g | \delta \rangle$ functions at each δ.

It can be seen that, for $\log(1+\delta) > -0.5$, the reconstruction uncertainty (i.e., random error) is much smaller than the cosmic variance uncertainty. The green curves in the upper panels are much lower than the black and violet, which are both practically identical, indicating the dominance of cosmic variance effects. The fact that the conditional mean function $\langle \delta_g | \delta \rangle$ does not vanish at $\log(1+\delta) < -0.5$ with the luminosity-complete samples for the 10k+30kZADE reconstruction in the lower redshift bins (Figure 7) is due to features of the ZADE in "filling" underdense regions. There is also the opposite effect, i.e., "emptying" of the underdense regions for the flux-limited samples in the higher redshift bins. This effect was clearly manifested already in Figures 4 and 5 as a sudden increase in the systematic offset from zero in the differences of $\langle \delta_g | \delta \rangle$ functions computed for the 10k+30kZADE and 40k mocks in the underdense regions $\log(1+\delta) \lesssim -0.5$, particularly visible in the $z > 0.7$ bin. Given that the matter distribution is lognormal, there is a very small volume at these very low underdensities, and the effect of this on the derived bias parameters is negligible. Moreover, the differences between the $\langle \delta_g | \delta \rangle$ functions computed for the reconstructions with the 10k+30kZADE and 40k mocks should not be identified with the reconstruction errors in the galaxy overdensity field (presented in Figures 6 and 7 in Kovač et al. 2010a).

The systematic error in the reconstruction of the density field changes the shape of $\langle \delta_g | \delta \rangle$ in different ways for the flux-limited and luminosity-complete $M_B < -20 - z$ samples of tracer galaxies, as follows. The reconstruction errors for the flux-limited sample of galaxies are negligible in low-redshift bins, and they increase in higher redshift bins, artificially increasing local bias $b(\delta, z, R)$ values in regions of both the highest and lowest density contrasts. For the volume-limited samples, the reconstruction error is manifested by lowering the local bias $b(\delta, z, R)$ values in the most underdense regions, and this error decreases with redshift. The different effect of the reconstruction error in the flux- and luminosity-complete samples arises from the fact that we use all spectroscopic galaxies to modify the probability functions for the objects without spectroscopic redshift, regardless of whether the spectroscopic objects will then be used in the computation of the density field.

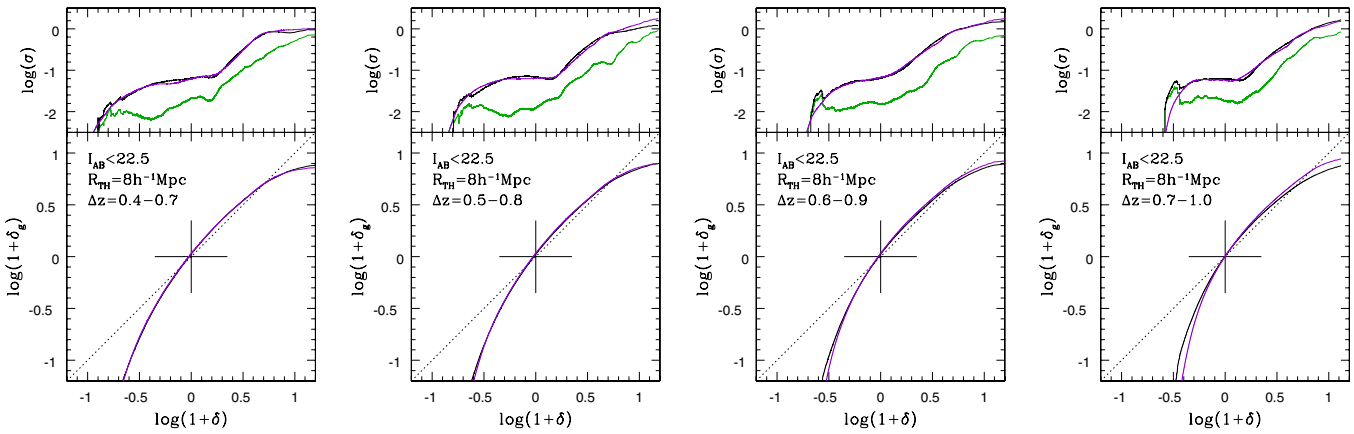

Figure 6. Reconstruction errors in the $\langle\delta_g|\delta\rangle$ function for the flux-limited samples. The analysis is carried out in four overlapping $\Delta z = 0.3$ bins covering $0.4 < z < 1$, indicated in the panels. Bottom panels: the $\langle\delta_g|\delta\rangle$ function of the overdensity field of galaxies ($I_{AB} < 22.5$) for a top-hat smoothing of $8\,h^{-1}$ Mpc for the 10k+30kZADE reconstruction (violet) and 40k reconstruction (black). The curves are obtained by averaging results from 12 mock catalogs of the same type. The systematic reconstruction error corresponds to the difference between these two averaged $\langle\delta_g|\delta\rangle$ functions from the 10k+30kZADE and 40k catalogs. Top panels: standard deviations in the corresponding $\langle\delta_g|\delta\rangle$ functions plotted below. The standard deviation (σ) of δ_g values from 12 40k-type mocks (black) and from 12 10k+30kZADE-type mocks (violet) corresponds to the cosmic variance error at a given δ. The standard deviation in the differences between $\langle\delta_g|\delta\rangle$ functions from the individual 10k+30kZADE and 40k catalogs (green) corresponds to the random reconstruction error.

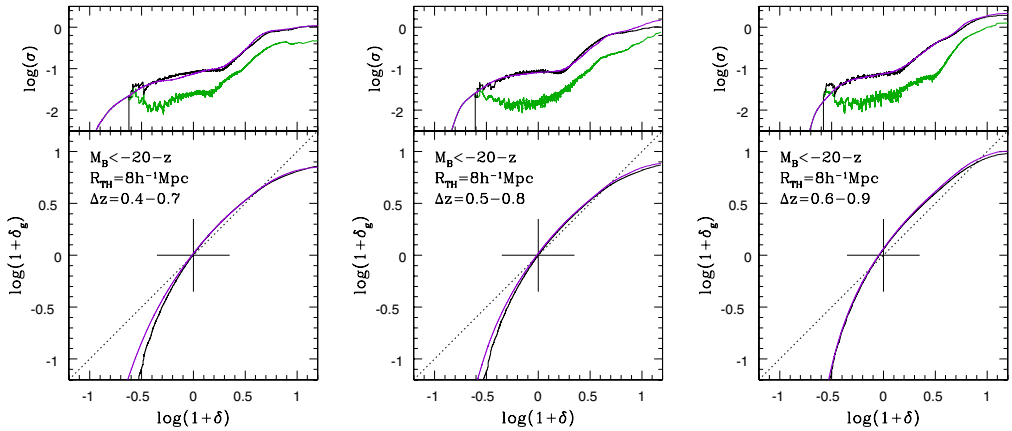

Figure 7. Reconstruction errors in the $\langle\delta_g|\delta\rangle$ function for the luminosity-complete samples. The analysis is carried out in three overlapping $\Delta z = 0.3$ bins covering $0.4 < z < 0.9$, indicated in the panels. The curves have the same meaning as in Figure 6, but the mock overdensity field is reconstructed with the $M_B < -20 - z$ galaxies.

Turning to the biasing parameters themselves, we compare the $\hat{b}$ and $\tilde{b}/\hat{b}$ parameters from the 10k+30kZADE and 40k samples in Figure 8. While there is a scatter in the differences between the biasing parameters estimated in the 10k+30kZADE and 40k catalogs (the plots in the first and third rows from the top in both panels in Figure 8), we can clearly see the systematic behavior in these differences. We quantify the systematic reconstruction error as the difference in the average biasing parameters from the 10k+30kZADE and 40k catalogs, obtained by averaging over the corresponding 12 mock catalogs. The systematic reconstruction error increases the $\hat{b}$ parameter for both flux-limited and luminosity-complete tracer galaxies (plots in the second row from the top in the left and right panels, respectively). On the other hand, the nonlinearity parameter $\tilde{b}/\hat{b}$ is hardly affected by the error in the reconstruction (plots in the forth row from the top in both panels). Moreover, it can be seen that the standard deviation in the differences between the $\hat{b}$ and $\tilde{b}/\hat{b}$ parameters in the 10k+30kZADE and 40k mocks is always smaller than the cosmic variance standard deviation (plots in the second and forth rows from the top in both panels in Figure 8), which again emphasizes the dominance of cosmic variance over the random uncertainty of the reconstruction.

We will use the standard deviation σ in the conditional mean $\langle\delta_g|\delta\rangle$ function and in the biasing parameters obtained from the 12 mock 40k catalogs as the cosmic variance errors in corresponding values derived from the zCOSMOS sample. We will also adopt the systematic effect, i.e., differences between the mean biasing quantities B from the 10k+30kZADE and 40k mocks, as the systematic reconstruction error. The values of such defined cosmic variance σ and reconstruction error $\Delta B_{\rm rec}$ for all samples considered in the biasing analysis are given in Table 2.

4.3. Shot Noise Errors

In this paper, we do not make any attempt to correct the reconstructed density field for the actual shot noise errors. Our goal is to understand and isolate the differential effect of the shot noise errors introduced due to the change in the mean intergalaxy separation (with respect to some value), e.g., for different luminosity-selected samples. This effect can be simulated by randomly resampling smaller fractions of the total population of galaxies.

Sparse sampling artificially enhances both the positive and the negative tails of the density contrast distribution. This effect broadens the PDF and thus steepens the conditional mean

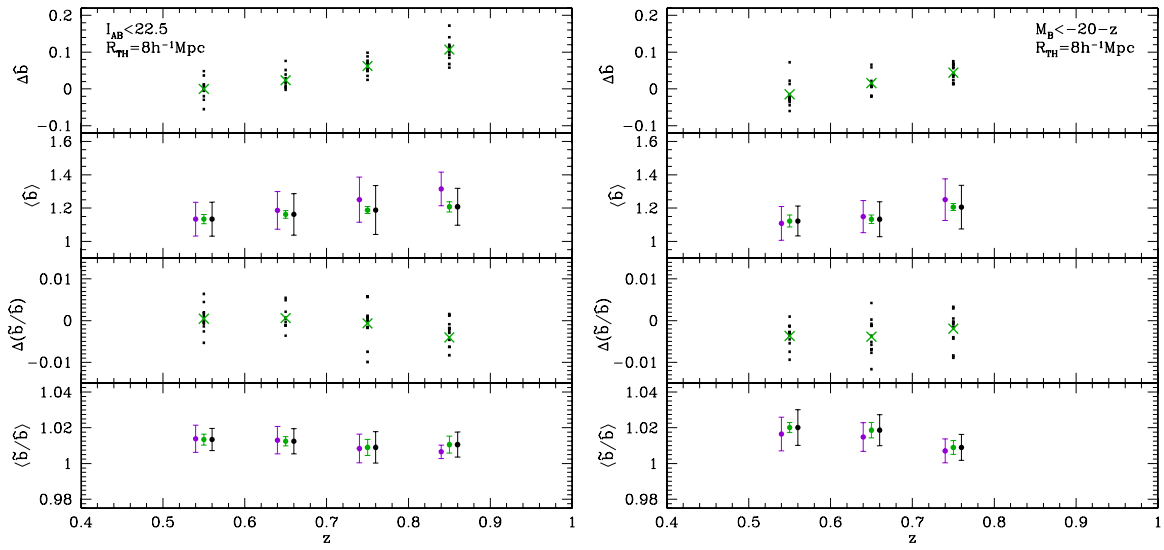

Figure 8. Reconstruction errors in the biasing parameters. Results obtained for the flux-limited $I_{AB} < 22.5$ and luminosity-complete $M_B < -20 - z$ samples with $R_{\rm TH} = 8\,h^{-1}$ Mpc are shown in the left and right panels, respectively, plotting the measured quantities in the middle of the redshift interval in which the analysis is carried out. For clarity, some of these quantities are slightly offset in the redshift. Differences between the biasing parameters in 12 pairs of 10k+30kZADE and 40k mock catalogs (black solid squares) and the average of these differences (green crosses) are shown in the first (for $\hat{b}$) and third (for $\tilde{b}/\hat{b}$) rows from the top. The biasing parameters obtained by averaging results from 12 10k+30kZADE (violet symbols) and 40k (black symbols) mock catalogs are shown in the second (for $\hat{b}$) and forth (for $\tilde{b}/\hat{b}$) rows from the top. The error bars are the corresponding standard deviations (i.e., the cosmic variance errors). In addition, we show also the standard deviations in the differences between the 10k+30kZADE and 40k biasing parameters (green error bars) from the individual mock catalogs in the second (for $\hat{b}$) and forth (for $\tilde{b}/\hat{b}$) rows from the top, plotted at the mean value of the 40k biasing parameters (green symbols). The difference between the average 10k+30kZADE and 40k mock parameters corresponds to the systematic reconstruction error, and the standard deviation of these differences corresponds to the random reconstruction error in the biasing parameters. The random reconstruction errors are smaller than the cosmic variance errors.

function $\langle\delta_g|\delta\rangle$ (e.g., SBD). To evaluate the shot noise effect, we use the 12 mocks (with the same overall geometrical constrains of the zCOSMOS survey) but extending the galaxy sample to include all galaxies down to an absolute magnitude $M_B < -18$. We ignore the luminosity evolution for the moment and the mean density is simply calculated as the number density of these galaxies in the full redshift range. $M_B = -18$ is approximately the faintest magnitude cut for which the given mock catalogs $r \leqslant 26$ (Kitzbichler & White 2007) are luminosity complete up to $z = 1$. The mean separation l between galaxies is about $2.7\,h^{-1}$ Mpc in the individual mocks, which should be sufficient to obtain the mean biasing function and its moments with the negligible shot noise errors for smoothing scales of $8\,h^{-1}$ Mpc and larger. To quantify the effect of the shot noise errors, we then resample these mock catalogs at random such that the mean distance between galaxies l successively increases to 3, 4, 5, 6, 7, and $8\,h^{-1}$ Mpc. We then derive the conditional mean function $\langle\delta_g|\delta\rangle$ and the second moments of the mean biasing function using the overdensity fields reconstructed from the resampled mock catalogs in two redshift bins: $0.4 < z < 0.7$ and $0.7 < z < 1$.

We present the systematic effect of this random resampling using the average of the 12 mock $\langle\delta_g|\delta\rangle$ functions in Figure 9. Changing the mean intergalaxy separation (i.e., in this case, change of the sampling rate of the same population, with the same actual bias) alters the shape of $\langle\delta_g|\delta\rangle$ very noticeably in the underdense regions, the effect clearly depending on the value of l (relative to R), i.e., on the mean number of galaxies per sampling region. In the underdense regions, the value of the mass density contrast that is associated with a given galaxy density contrast is artificially shifted to higher values as the mean intergalaxy separation increases. This is important given that this minimum δ value, below which the galaxy density field does not trace that of the matter, is often interpreted as the minimum mass density contrast below which the formation of tracer galaxies is partially or completely suppressed (e.g., Somerville et al. 2001; Marinoni et al. 2005). This analysis shows that it can instead arise purely from these shot noise effects rather than any underlying physical process.

In Figure 9, we examine the $\langle\delta_g|\delta\rangle$ function computed with $R_{\rm TH} = 8$ and $R_{\rm TH} = 10\,h^{-1}$ Mpc, for a constant set of galaxies, sampled with different l. Although the $\langle\delta_g|\delta\rangle$ function in overdense regions is different for $R_{\rm TH} = 8$ and $R_{\rm TH} = 10\,h^{-1}$ Mpc at $l \sim 2.7\,h^{-1}$ Mpc, it can be seen that its differential change with l (i.e., the change with l in the difference between the $\langle\delta_g|\delta\rangle$ functions for the samplings with l and $l \sim 2.7\,h^{-1}$ Mpc) is comparable for the two smoothing scales. In other words, the differential effect of shot noise in the most overdense regions is independent of $R_{\rm TH}$, for these $R_{\rm TH}$. The situation is opposite in the most underdense regions. For these regions, there is only a small difference between the $l \sim 2.7\,h^{-1}$ Mpc conditional mean $\langle\delta_g|\delta\rangle$ functions with $R_{\rm TH} = 8$ and $R_{\rm TH} = 10\,h^{-1}$ Mpc, but a larger differential effect is seen in $\langle\delta_g|\delta\rangle$ between the two smoothing radii as l increases. The conclusion is that changes in $\langle\delta_g|\delta\rangle$ in overdense regions for different galaxy samples (with different comoving densities and intergalaxy separations) are more likely to be physical effects than changes in $\langle\delta_g|\delta\rangle$ in low-density regions, where the effects of shot noise must be carefully considered.

A summary of the effect of the shot noise errors on the linear and nonlinear biasing parameters is shown in Figures 10 and 11, respectively. We show first the differences, in the individual mocks, between the biasing parameters obtained for the subsamples with various l and those with the full $l \sim 2.7\,h^{-1}$ Mpc (top plots in both panels in Figures 10 and 11). Then we show, below, the values of the biasing parameters averaged over the 12 mock catalogs for the various l. The (averaged) linear biasing parameter $\hat{b}$ increases monotonically

Table 2
Summary of the Measured zCOSMOS Biasing Parameters

$R_{\rm TH}$ (h^{-1} Mpc)	$z_{\rm min}$	$z_{\rm max}$	Tracers	$\hat{b}$	$\sigma_{CV}(\hat{b})$	$\Delta\hat{b}_{\rm rec}$	$\tilde{b}/\hat{b}$	$\sigma_{CV}(\tilde{b}/\hat{b})$	$\Delta(\tilde{b}/\hat{b})_{\rm rec}$
8	0.4	0.7	Flux	1.15	0.10	0.00	1.005	0.006	0.000
8	0.5	0.8	Flux	1.32	0.12	0.02	1.002	0.007	0.001
8	0.6	0.9	Flux	1.61	0.15	0.06	1.004	0.009	−0.001
8	0.7	1.0	Flux	1.63	0.11	0.11	1.003	0.007	−0.004
8	0.4	0.7	−19.5-z	1.18	0.10	0.00	1.005	0.009	−0.001
8	0.4	0.7	−20-z	1.24	0.09	−0.01	1.005	0.010	−0.004
8	0.5	0.8	−20-z	1.41	0.10	0.02	1.002	0.009	−0.004
8	0.6	0.9	−20-z	1.65	0.13	0.04	1.005	0.007	−0.002
8	0.4	0.7	−20.5-z	1.40	0.10	−0.07	1.008	0.008	−0.004
8	0.5	0.8	−20.5-z	1.58	0.11	−0.05	1.007	0.008	−0.004
8	0.6	0.9	−20.5-z	1.84	0.13	0.00	1.011	0.007	−0.002
8	0.7	1.0	−20.5-z	1.78	0.08	0.04	1.005	0.006	−0.004
10	0.4	0.7	Flux	1.16	0.12	0.01	1.006	0.006	0.000
10	0.5	0.8	Flux	1.32	0.13	0.01	1.003	0.005	0.000
10	0.6	0.9	Flux	1.60	0.15	0.03	1.004	0.008	0.000
10	0.7	1.0	Flux	1.59	0.11	0.06	1.004	0.006	0.001
10	0.4	0.7	−19.5-z	1.19	0.12	0.02	1.004	0.008	0.002
10	0.4	0.7	−20-z	1.24	0.11	0.01	1.004	0.010	−0.004
10	0.5	0.8	−20-z	1.40	0.11	0.02	1.004	0.010	−0.004
10	0.6	0.9	−20-z	1.64	0.14	0.02	1.005	0.007	0.000
10	0.4	0.7	−20.5-z	1.40	0.11	−0.04	1.009	0.008	−0.003
10	0.5	0.8	−20.5-z	1.57	0.12	−0.03	1.008	0.009	−0.003
10	0.6	0.9	−20.5-z	1.81	0.14	−0.01	1.012	0.008	−0.002
10	0.7	1.0	−20.5-z	1.73	0.09	0.01	1.007	0.005	−0.002
12	0.4	0.7	Flux	1.19	0.13	0.01	1.010	0.005	0.001
12	0.5	0.8	Flux	1.36	0.14	0.02	1.005	0.004	0.000
12	0.6	0.9	Flux	1.66	0.16	0.05	1.011	0.007	0.000
12	0.7	1.0	Flux	1.62	0.12	0.07	1.008	0.006	0.000
12	0.4	0.7	−19.5-z	1.22	0.14	0.02	1.007	0.007	0.001
12	0.4	0.7	−20-z	1.27	0.12	0.01	1.007	0.011	−0.002
12	0.5	0.8	−20-z	1.44	0.12	0.03	1.006	0.014	−0.005
12	0.6	0.9	−20-z	1.69	0.14	0.05	1.013	0.008	−0.001
12	0.4	0.7	−20.5-z	1.42	0.13	−0.03	1.011	0.009	−0.001
12	0.5	0.8	−20.5-z	1.61	0.13	−0.01	1.012	0.012	−0.004
12	0.6	0.9	−20.5-z	1.86	0.14	0.03	1.024	0.009	−0.001
12	0.7	1.0	−20.5-z	1.76	0.09	0.03	1.013	0.005	−0.002

Notes. The content of the columns is as follows. Column 1: smoothing radius $R_{\rm TH}$; Columns 2 and 3: lower and upper limits of the redshift bin, respectively; Column 4: type of the tracer galaxies; Column 5: measured $\hat{b}$ parameter; Columns 6 and 7: cosmic variance and systematic reconstruction errors in the $\hat{b}$ parameter, respectively; Column 8: measured $\tilde{b}/\hat{b}$ parameter; Columns 9 and 10: cosmic variance and systematic reconstruction errors in the $\tilde{b}/\hat{b}$ parameter, respectively.

with increasing mean intergalaxy separation. The nonlinearity parameter $\tilde{b}/\hat{b}$ is constant, or even slightly decreasing, as the mean intergalaxy separation increases, especially in the higher redshift bin.

To try to parameterize the differential effect of the shot noise errors, we combine the differential changes in $\hat{b}$ and $\tilde{b}/\hat{b}$ as functions of $l/R_{\rm TH}$. We find that at a given redshift the obtained mock results can be well described by the following relations:

$$\log\langle\hat{b}_l - \hat{b}_{2.7}\rangle = a\log(l/R_{\rm TH}) + b \quad (22)$$

and

$$\langle(\tilde{b}/\hat{b})_l - (\tilde{b}/\hat{b})_{2.7}\rangle = a'\log(l/R_{\rm TH}) + b', \quad (23)$$

where the averages are obtained over differences in 12 individual mock catalogs. These average values as a function of $\log(l/R_{\rm TH})$ and the corresponding linear fits are presented in Figure 12.

The obtained relations are clearly dependent on the "true" value of the biasing parameter (i.e., value measured for the sample of galaxies with $l \sim 2.7\,h^{-1}$ Mpc) and we will later use these relations to quantify the expected differential change in the zCOSMOS biasing parameters due to the change in the mean intergalaxy separation, assuming that the mock $M_B < -18$ results are valid for any other sample of zCOSMOS tracer galaxies, which is of course only an approximation. Moreover, from the presented scaling relations it is obvious that the change in l is not equivalent to a change in $R_{\rm TH}$, as the presented fitting equations are clearly offset at the same $l/R_{\rm TH}$ for measurements with different $R_{\rm TH}$. This means that they cannot be used to assess the possible differential change in the biasing parameters due to a change in the smoothing scales.

5. BIASING ANALYSIS: RESULTS AND THEIR INTERPRETATION

We derive the conditional mean function $\langle\delta_g|\delta\rangle$ and the biasing parameters $\hat{b}$ and $\tilde{b}/\hat{b}$ of the zCOSMOS galaxies using four subsets of galaxies from the overall 10k+30kZADE sample: the $I_{AB} < 22.5$ flux-limited sample and three luminosity-complete samples of $M_B < -19.5 - z$, $M_B < -20 - z$, and $M_B < -20.5 - z$ galaxies. We reconstruct the density field following Equation (8) with the top-hat three-dimensional filter (Equation (9)), using smoothing scales of 8, 10, and

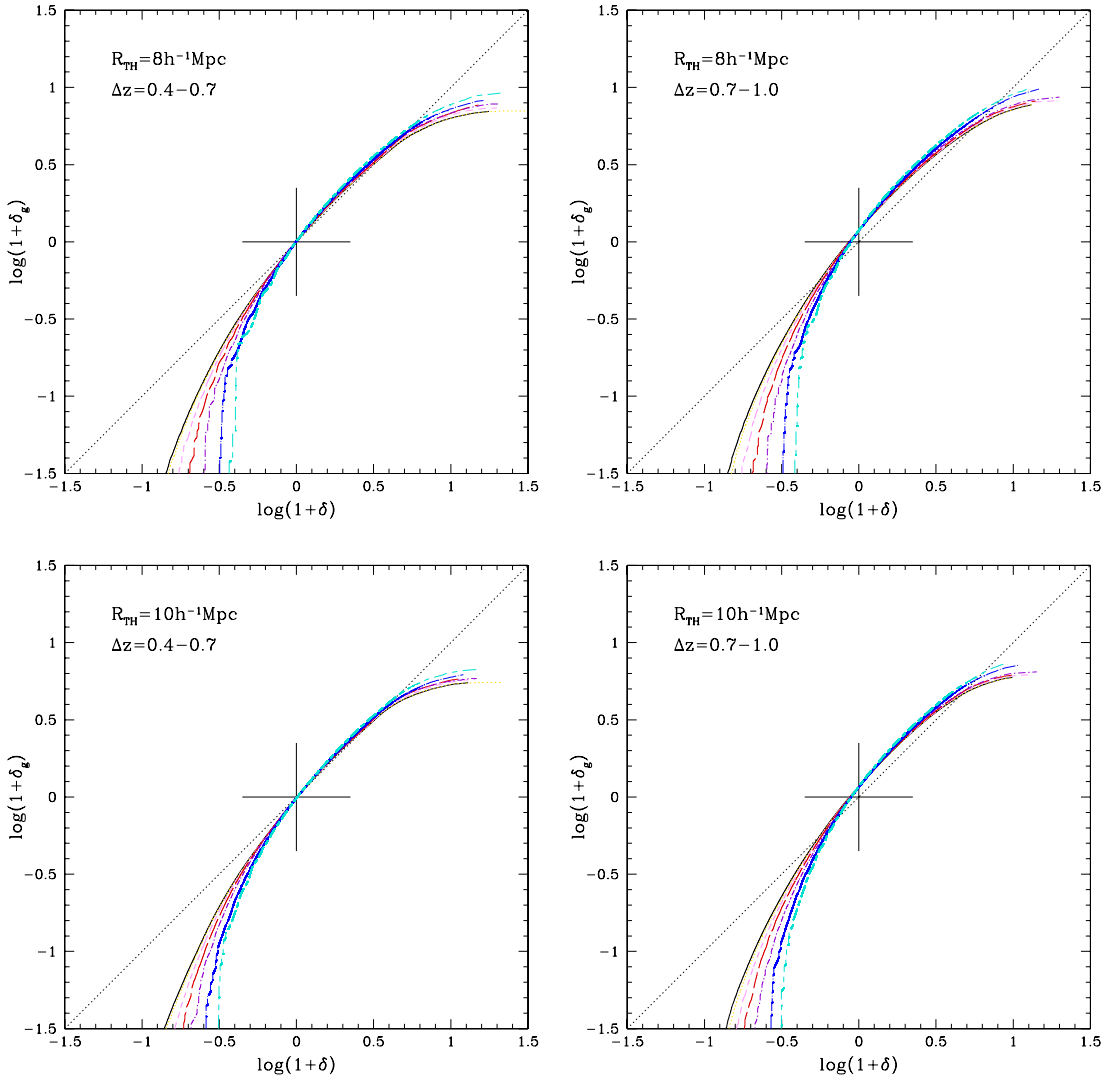

Figure 9. Effect of galaxy sampling on the conditional mean function $\langle \delta_g | \delta \rangle$. The $\langle \delta_g | \delta \rangle$ functions averaged over 12 mock $M_B < -18$ catalogs are obtained for the sample with mean galaxy separation l of the full sample ($l \sim 2.7\,h^{-1}$ Mpc, black) and of the subsequently randomly selected subsamples with l of 3 (yellow), 4 (pink), 5 (red), 6 (violet), 7 (blue), and 8 (cyan) h^{-1} Mpc. The $\langle \delta_g | \delta \rangle$ functions are presented in two redshift bins: $0.4 < z < 0.7$ and $0.7 < z < 1.0$ in the left and right panels, respectively, and for two top-hat smoothing filters of 8 and $10\,h^{-1}$ Mpc in the top and bottom panels, respectively.

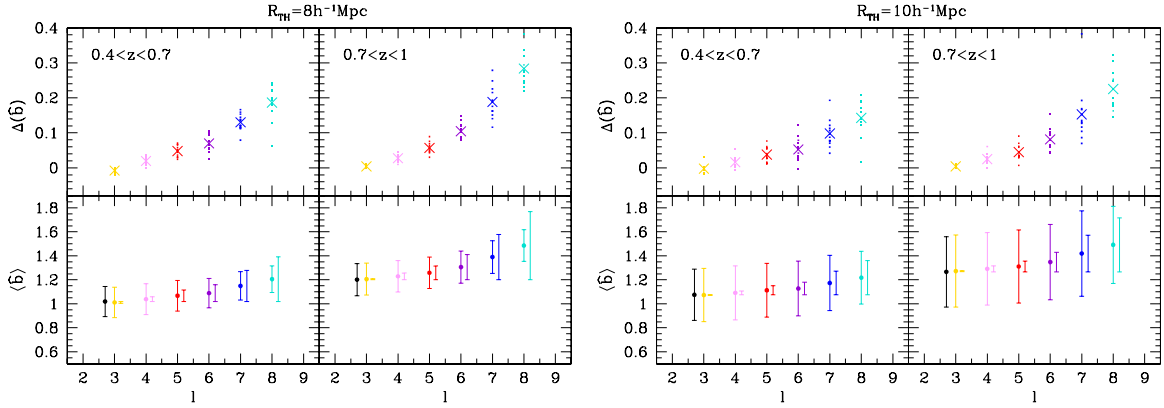

Figure 10. Effect of galaxy sampling on the linear biasing parameter using $M_B < -18$ mock catalogs. Differences between the $\hat{b}$ parameters in the l-subsampled and $l \sim 2.7\,h^{-1}$ Mpc individual mock catalogs (small solid squares) and the averages of these differences (crosses) are presented in the top panels, plotted as a function of l. Linear bias obtained by averaging the $\hat{b}$ parameters from 12 mocks of a given l is presented in the bottom panels. The error bars correspond to the standard deviations of the $\hat{b}$ parameters (i.e., cosmic variance errors). Slightly offset (along the l-axis) error bars correspond to the standard deviation in the differences between the l-subsampled and $l \sim 2.7\,h^{-1}$ Mpc individual mock catalogs, presented in the top panels. The four panel plots on the left and right sides are obtained for the galaxy density field reconstructed with $R_{\rm TH} = 8\,h^{-1}$ Mpc and $R_{\rm TH} = 10\,h^{-1}$ Mpc, respectively. In each of the four panels, the left-hand plots refer to $0.4 < z < 0.7$ and the right-hand plots refer to $0.7 < z < 1$.

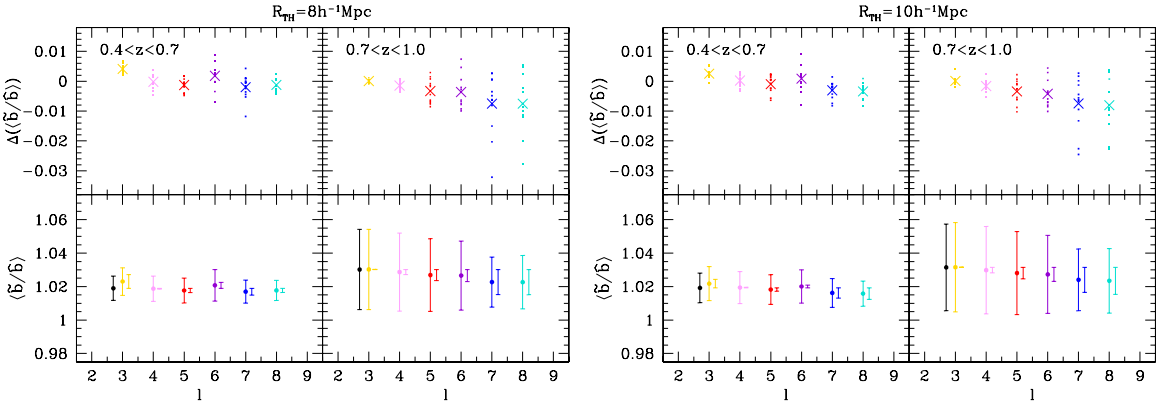

Figure 11. Effect of galaxy sampling on the nonlinear biasing parameter using $M_B < -18$ mock catalogs. We plot the equivalent quantities as in Figure 10 derived for the nonlinearity $\tilde{b}/\hat{b}$ parameters.

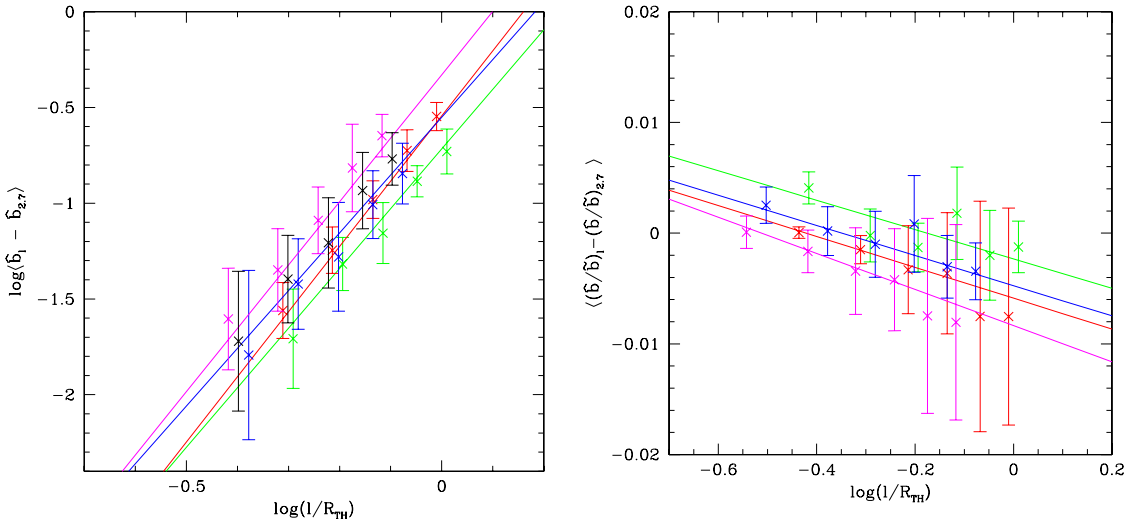

Figure 12. Differential effect of galaxy sampling on the biasing parameters at a given $l/R_{\rm TH}$ for the $M_B < -18$ mock samples. The points are the average values of the differences between the biasing parameters from the l-subsampled and $l \sim 2.7\,h^{-1}$ Mpc individual mock catalogs, plotted as a function of $l/R_{\rm TH}$. The differences for the $\hat{b}$ parameters are plotted in the left panel, in logarithmic units, starting from $l = 4$ due to noise in the results with $l = 3$, and the differences for the $\tilde{b}/\hat{b}$ parameters are plotted in the right panel, starting from $l = 3$. The vertical error bars are the standard deviations on the plotted differences, in the corresponding units. The continuous lines correspond to the best linear fits to the quantities plotted in the x- and y-axes. The symbols, errors, and lines are marked in green, red, blue, and magenta for the samples of $M_B < -18$ mock galaxies with $R_{\rm TH} = 8\,h^{-1}$ Mpc in $0.4 < z < 0.7$, $R_{\rm TH} = 8\,h^{-1}$ Mpc in $0.7 < z < 1.0$, $R_{\rm TH} = 10\,h^{-1}$ Mpc in $0.4 < z < 0.7$, and $R_{\rm TH} = 10\,h^{-1}$ Mpc in $0.7 < z < 1.0$. See the text for more details.

$12\,h^{-1}$Mpc. The range of the smoothing scales is limited by the minimum of $8\,h^{-1}$ Mpc at which we can reliably reconstruct the overdensity field (see Section 4.2) and the finite transverse size of the zCOSMOS field ($\sim 54\,h^{-1}$ Mpc at $z = 1$). We use the ZADE approach to account for galaxies without reliably measured spectroscopic redshift and therefore $\phi_i = 1$ for every tracer galaxy. We use only the unity-weighted overdensity field ($m_i = 1$) for the biasing analysis.

We reconstruct the zCOSMOS galaxy overdensity field on a grid separated by $0.5\,h^{-1}$ Mpc in the plane of the sky, and with $\Delta z = 0.002$, as was also done for the reconstruction of galaxy overdensity field on the mocks. The overdensity field that is reconstructed with $R = 8\,h^{-1}$ Mpc and flux-limited tracers in $0.4 < z < 1$ is shown in Figure 13. The complex, cosmic-web appearance of the density field, consisting of cluster-like structures, surrounded by empty, void-like regions, is visible throughout the redshift range probed (see Kovač et al. 2010a for the more detailed discussion of the structures in the zCOSMOS overdensity field).

We carry out the biasing analysis in the redshift range $0.4 < z < 1$, starting at $z = 0.4$ in order to exclude redshift slices in which a majority of grid points would have more than 50% of the sampling volume outside of the survey limits. We calculate the density contrasts in four redshift bins: $0.4 < z < 0.7$, $0.5 < z < 0.8$, $0.6 < z < 0.9$, and $0.7 < z < 1$, which overlap in order to maximize each volume and suppress the effect of the cosmic variance. The importance of the cosmic variance is clearly visible in the zCOSMOS overdensity field plots, as the large structures extend over a broad range in redshift (i.e., $\Delta z \sim 0.05$, seen in Figure 13; see also Figures 19 and 24 in Kovač et al. 2010a) and this will hamper the expected evolution in the distribution of large-scale structures with cosmic time (see Figure 26 in Kovač et al. 2010a). At lower redshift, the mean overdensity in the individual redshift slices differs from zero by a few percent. However, in $0.6 < z < 0.9$ and $0.7 < z < 1$, the mean overdensity is about 0.1–0.15 for all but $M_B < -20.5 - z$ sample in $0.6 < z < 0.9$, for which the mean overdensity is about 0.2. Therefore, the bias values for these samples need to be taken with caution. As discussed in the previous sections, the PDF of the mass density contrast is calculated assuming a lognormal distribution (Equation (13)), specified by the adopted cosmology.

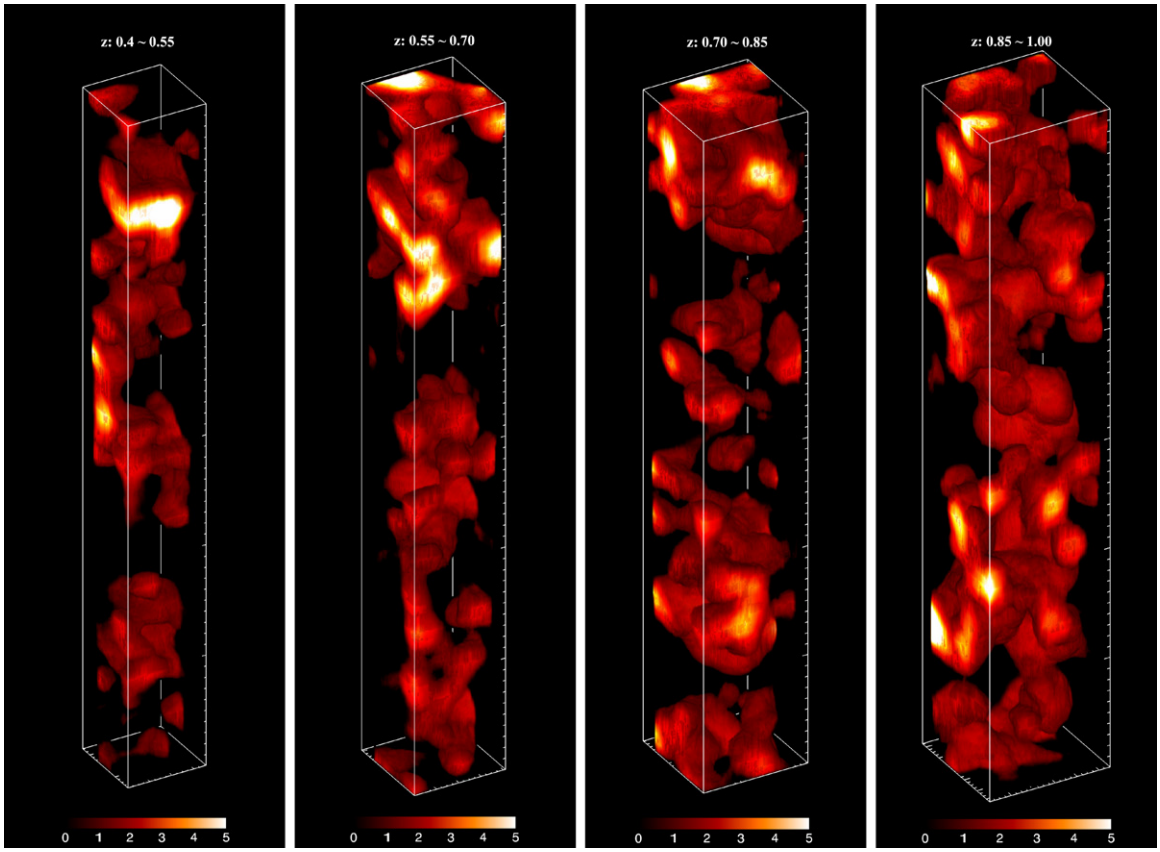

Figure 13. zCOSMOS overdensity field reconstructed with $R = 8\,h^{-1}$ Mpc and flux-limited tracer galaxies in $0.4 < z < 1$. The color scale on the bottom is given in the $1 + \delta$ units. The horizontal axes are RA and DEC, the vertical axis is redshift. The size of the box is 35, 40, 45, and $50\,h^{-1}$ Mpc along R.A. and decl. axes from lower to higher redshift and ∼0.15 along redshift. We plot only structures above the mean density ($1 + \delta > 1$), in order to increase the visibility.

(A color version of this figure is available in the online journal.)

We apply the errors estimated from the mock catalogs in Section 4 to the zCOSMOS analysis. For the mean conditional $\langle \delta_g | \delta \rangle$ function, we adopt the error which has been measured on the corresponding mock $\delta_g(\delta)$ value at the same δ. For the biasing parameters, we adopt the errors on the biasing parameters derived from the corresponding mock catalogs. As our final best estimate, we consider the zCOSMOS measured biasing quantities $B_{\rm measured}$ corrected for the systematic reconstruction error $\Delta B_{\rm rec}$ (e.g., see bottom panels in Figures 6 and 7 for $\Delta B_{\rm rec}$ in $\langle \delta_g | \delta \rangle$) with an uncertainty dominated by the cosmic variance σ_{CV} (e.g., see top panels in Figures 6 and 7, black and violet curves, for σ_{CV} in $\langle \delta_g | \delta \rangle$). Schematically this can be written as follows: $B = (B_{\rm measured} - \Delta B_{\rm rec}) \pm \sigma_{CV}$, following our definitions of these errors. We neglect the random reconstruction error $\sigma_{\rm rec}$ (e.g., see top panels in Figures 6 and 7, green curves, for $\sigma_{\rm rec}$ in $\langle \delta_g | \delta \rangle$) in the final estimate as it is much smaller than σ_{CV}. However, when comparing the various zCOSMOS results within one redshift bin, we will neglect the cosmic variance and use the random component of the reconstruction error instead. When relevant, we will discuss this in more detail in the following sections. The shot noise error is very difficult to apply directly, as we have quantified only its differential effect for the $M_B < -18$ mock samples. We will therefore be more descriptive about the contribution of the shot noise errors on our results—discussing their effect on the $\langle \delta_g | \delta \rangle$ function and tentatively quantifying the differential shot noise contribution on the biasing parameters. We want to stress again that to asses the shot noise errors we will extrapolate the results from the $M_B < -18$ mock catalogs to the zCOSMOS data for the fainter samples of galaxies, as that is the best what we can do at the moment. Therefore all the shot noise related corrections should be considered as an indication only. When necessary, we combine the random errors by adding their absolute values, as we do not have the evidence that they are independent. Particularly, there may be a residual effect of the cosmic variance in the random component of any error as all the tests which we have carried out are based on the zCOSMOS-size mock catalogs, while for the, e.g., reconstruction errors it would have been more preferable to carry out the tests on a field few times the zCOSMOS area.

As a final caution, we need to add that there is some level of the uncertainty arising from the fact that we are using the mock-estimated errors on the data. Clearly, if the mock catalogs had a completely different cosmological biasing, this could give wrong results. However, we have seen (e.g., figures in Section 4) that the biasing in the mocks is actually quite similar to the biasing in the data and so our approach is reasonable, while obviously not absolutely perfect. Moreover, as discussed in Section 3, there will also be an error on the estimated biasing quantities from the adoption of this particular method to estimate the conditional mean $\langle \delta_g | \delta \rangle$ function itself. The contribution of this error is also not possible to quantify, as SBD only quote the errors on the method for their particular simulations, carried out assuming different cosmologies than ours. Also, their sample of mock galaxies is fainter than the samples of zCOSMOS galaxies used here. However, the expected errors should be of the order of a few percent (SBD; see also Section 3).

The values of measured biasing parameters are given in Table 2, together with the cosmic variance and systematic

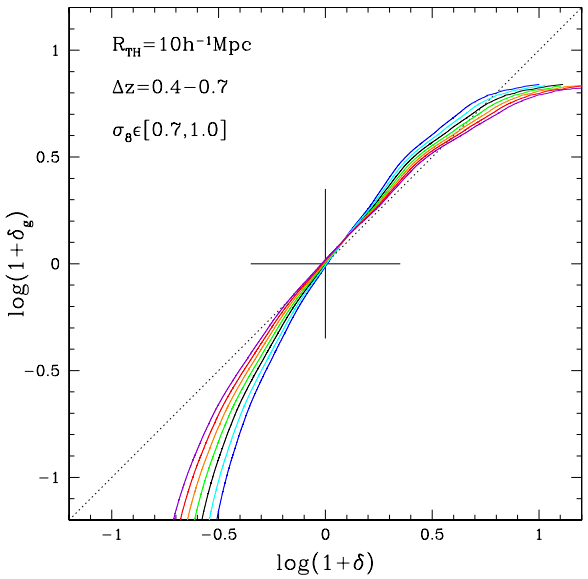

Figure 14. Conditional mean function $\langle\delta_g|\delta\rangle$ estimated for different σ_8 values. The parameter σ_8 increases from 0.7 to 1 in steps of 0.05. The resulting $\langle\delta_g|\delta\rangle$ function is presented in blue for $\sigma_8 = 0.7$, in cyan for $\sigma_8 = 0.75$, in black for $\sigma_8 = 0.8$, in green for $\sigma_8 = 0.85$, in orange for $\sigma_8 = 0.9$, in red for $\sigma_8 = 0.95$, and in violet for $\sigma_8 = 1$. The galaxy density field is obtained with the $M_B < -20 - z$ sample of galaxies in $0.4 < z < 0.7$ and the smoothing filter $R_{\rm TH} = 10\,h^{-1}$ Mpc.

reconstruction errors estimated from the analyses on the mock catalogs in Section 4. The detailed discussion and interpretation of the results obtained from the biasing analysis is presented in the following sections.

When interpreting the zCOSMOS biasing results and comparing them to other work, one has to keep in mind that the obtained results and their exact redshift evolution are both cosmology dependent. This is evident from the dependence of the growth rate on the cosmological parameters, and particularly the results are dependent on the chosen $\sigma_8(z = 0)$ normalization. SBD find that the linear biasing parameter $\hat{b}$ changes as σ_8^{-1}, while the nonlinearity parameter $\tilde{b}/\hat{b}$ changes only very weakly with σ_8, $\tilde{b}/\hat{b} \sim \sigma_8^{0.15}$. We show in Figure 14 the change of the shape of the $\langle\delta_g|\delta\rangle$ function with the σ_8 parameter on the arbitrarily chosen results with the $M_B < -20 - z$ sample of zCOSMOS galaxies in $0.4 < z < 0.7$ and the smoothing filter $10\,h^{-1}$ Mpc. Lowering σ_8 will produce less structure at a given epoch, and it has a similar effect on the change in the shape of the mean biasing function as the increasing the mean intergalaxy separation.

5.1. Shape of the Conditional Mean Function $\langle\delta_g|\delta\rangle$

We show the zCOSMOS conditional mean function $\langle\delta_g|\delta\rangle$ in Figures 15 and 16, where the galaxy overdensity fields are reconstructed with the luminosity-complete $M_B < -20 - z$ sample of galaxies for the smoothing filters of 8 and $10\,h^{-1}$ Mpc, respectively. We show both the functions measured directly from the data and the functions corrected for the systematic reconstruction error including the cosmic variance error on the latter ones. We also show the corresponding linear biasing approximation $\delta_g = b_L\delta$ with $b_L = \hat{b}$ at every δ. We use the value of $\hat{b}$ corrected for the systematic reconstruction error in these plots, but the $\delta_g = b_L\delta$ model with $\hat{b}_{\rm measured}$ would be almost indistinguishable from the shown function. By comparing the shape of the $\langle\delta_g|\delta\rangle$ function with the linear approximation, it is visually straightforward to assess in which δ regions the linear bias model is a valid simplification.

The $\langle\delta_g|\delta\rangle$ function vanishes in the most underdense regions. At moderate underdensities the $\langle\delta_g|\delta\rangle$ function sharply rises with approaching $\delta_g \approx \delta = 0$. From this point, up to the mildly overdense regions, the $\langle\delta_g|\delta\rangle$ function closely follows the linear relation with δ. In the most overdense regions, the shape of $\langle\delta_g|\delta\rangle$ suggests that galaxies are antibiased tracers of the underlying matter distribution. The local slope $b(\delta, z, R)$ of the biasing relation in the underdense regions is larger than unity. In the overdense regions, the trend is less clear, as the local slope can take values both larger and smaller than unity.

This characteristic shape of the conditional mean function $\langle\delta_g|\delta\rangle$ persists for all the samples of tracer galaxies and in all the redshift intervals covered by our study. The biasing relation between galaxies and matter is clearly nonlinear in the most underdense and overdense regions in $0.4 < z < 1$, in agreement with previous work at these redshifts, based both on simulations and SAM (SBD; Somerville et al. 2001) and on observations (Marinoni et al. 2005).

Theoretical work provides some explanation for the observed shape of the conditional mean function $\langle\delta_g|\delta\rangle$. The vanishing of the function in the underdense regions can be interpreted within

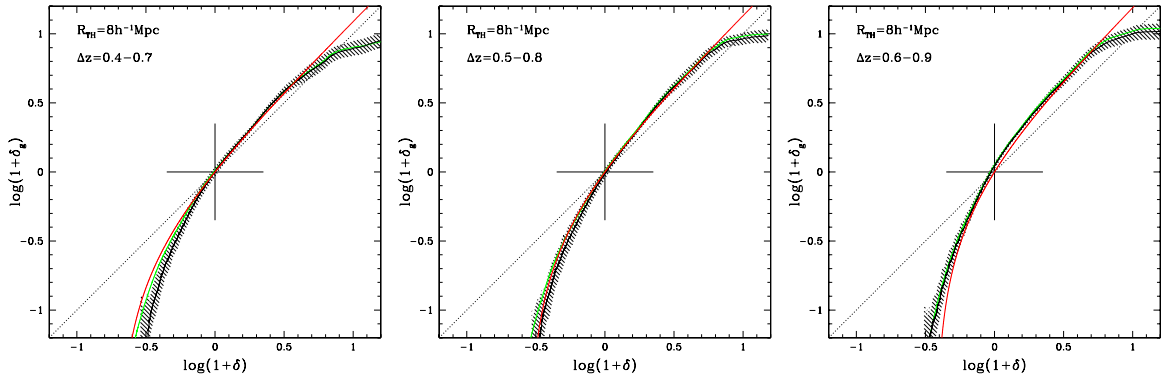

Figure 15. Conditional mean function $\langle\delta_g|\delta\rangle$ for the density field of the zCOSMOS galaxies ($M_B < -20 - z$) obtained by smoothing on scales of $8\,h^{-1}$ Mpc. The green curve is the $\langle\delta_g|\delta\rangle$ function measured directly from the data. The black curve is the $\langle\delta_g|\delta\rangle$ function corrected at each δ for the systematic reconstruction error in $\delta_g(\delta)$. The shaded area corresponds to the 1σ cosmic variance error in $\delta_g(\delta)$ (i.e., it encloses the errors along the y-axis). The shaded area in the underdense regions with δ smaller than the smallest δ value for which the $\langle\delta_g|\delta\rangle$ function is plotted is a part of the cosmic variance errors for $\delta_g(\delta)$, not visible on the plot. The red curve corresponds to the linear biasing case $\delta_g = \hat{b}\delta$, where $\hat{b}$ is the corresponding linear biasing parameter corrected for the systematic reconstruction error. The different panels are for the different redshift bins: $0.4 < z < 0.7$, $0.5 < z < 0.8$, and $0.6 < z < 0.9$ from the left to the right, respectively.

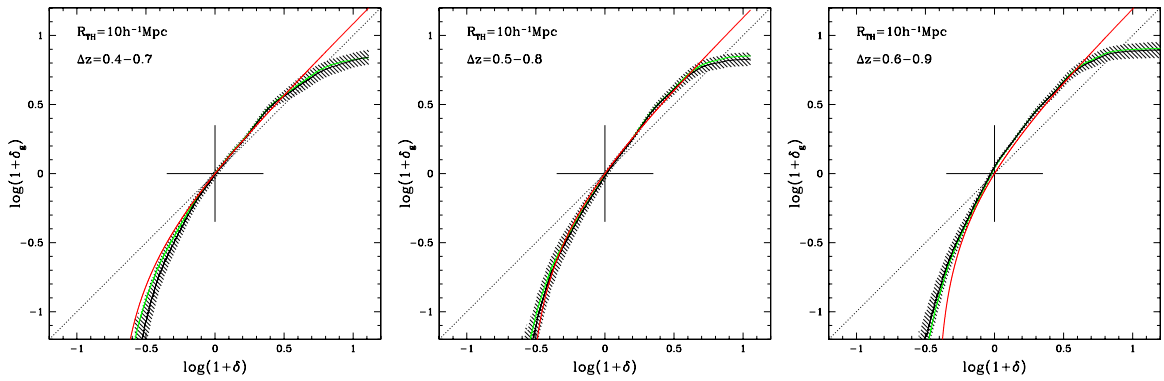

Figure 16. Conditional mean function $\langle\delta_g|\delta\rangle$ for the density field of the zCOSMOS galaxies ($M_B < -20 - z$) obtained by smoothing on scales of $10\,h^{-1}$ Mpc. The meaning of the curves and symbols is the same as in Figure 15.

a scenario in which galaxies do not form below some mass density threshold. However, as discussed above, one needs to be rather careful in this interpretation and consider the possible shot noise effects into account. The antibiasing of galaxies in the most overdense regions can be explained by quenching of galaxy formation in these regions, as at these redshifts the densest regions become too hot (Blanton et al. 2000). The other possibility to explain the antibiasing of galaxies in the most overdense regions are different epochs of formation of galaxies in overdense and underdense regions (Yoshikawa et al. 2001). This follows from the hierarchical scenario of galaxy formation, where for a given mass scale, there is a tendency for objects in overdense regions to form earlier than objects in the underdense regions. Therefore the young galaxies (e.g., with formation redshift since 1.7 in Yoshikawa et al. 2001) are expected to form in low-density, which are also low-temperature, environments. Also, the merging of galaxies in high-density environments could lower the number density of galaxies used to derive the density field (Marinoni et al. 2005).

5.2. Scale Dependence

To examine the possible dependence of the biasing quantities on the smoothing scale, we compare the results from the biasing analysis obtained with the $M_B < -20 - z$ tracer galaxies smoothed with three different filters: 8, 10, and $12\,h^{-1}$ Mpc. The cosmic variance, which is the dominant random error for the final estimates of biasing quantities, is not relevant in this case, as we want to compare the biasing quantities within a single field and redshift bin. Therefore we asses the significance of the differences between the $\langle\delta_g|\delta\rangle$ functions and biasing parameters obtained with various smoothing scales with respect to $\sigma_{\rm rec}$, which is our best estimate of the relevant random error within a single field.

We first compare the $\langle\delta_g|\delta\rangle$ functions. The results are plotted in Figure 17 in two redshift bins: $0.4 < z < 0.7$ and $0.6 < z < 0.9$, where in the top panels we show $\langle\delta_g|\delta\rangle$ as measured from the data, and in the bottom panels we show these functions after applying the systematic and random reconstruction errors. The differences between the $\langle\delta_g|\delta\rangle$ functions for different smoothing scales are not highly significant with respect to the $\sigma_{\rm rec}$ errors in all but the most overdense regions. For example, at $\log(1+\delta) = 1$ the difference between the $\delta_g(\delta)$ values smoothed with 8 and 10, 8 and 12, and 10 and $12\,h^{-1}$ Mpc is different from zero at 1.4σ, 3.0σ, and 1.4σ levels in $0.4 < z < 0.7$, respectively, and at 2.0σ, 4.1σ, and 2.7σ levels in $0.6 < z < 0.9$, respectively. Here, σ represents the sum of the corresponding random reconstruction errors (the quoted significance is not given in logarithmic units). Moreover, it is interesting to note that in the most overdense regions, the characteristic δ at which galaxies become antibiased decreases as the smoothing scale increases.

To try to understand the possible shot noise effect in the $\langle\delta_g|\delta\rangle$ function due to the change in the radius of the smoothing filter, we look back to the mock results presented in Figure 9. As we have summarized earlier, the change in the smoothing scale will not change the shot noise contribution in the most overdense regions. *If* the same is valid also for the results obtained with the zCOSMOS $M_B < -20-z$ sample, this would signify the observed difference in the conditional mean $\langle\delta_g|\delta\rangle$ functions due to change in $R_{\rm TH}$ in the most overdense regions. The small differences in the underdense regions between the $\langle\delta_g|\delta\rangle$ functions with various $R_{\rm TH}$, visible in the bottom panels in Figure 17, are consistent with the expected contribution of the shot noise errors in these regions. Moreover, the differences seen in the underdense regions fall within the sum of the random reconstruction errors.

The most overdense regions are very rare, and to obtain the overall picture, we study the impact of the different smoothing scales on the biasing parameters. The results are shown in Figure 18, and the differences between the biasing parameters obtained for the various smoothing filters and their errors are given in Table 3. To compare the zCOSMOS biasing parameters with each other, we neglect the cosmic variance, and consider only the systematic and random reconstruction errors. We find that the difference between the linear biasing parameters $\hat{b}$ obtained for the $M_B < -20 - z$ density fields smoothed on the scales from 8 to $12\,h^{-1}$ Mpc is less than 1.1σ in all redshift bins and for all possible combinations of smoothing scales. We measure a small significant difference at 1.5σ between the nonlinearity parameters $\tilde{b}/\hat{b}$ with $R_{\rm TH} = 10$ and $R_{\rm TH} = 12\,h^{-1}$ Mpc in $0.6 < z < 0.9$, but the other differences between the nonlinear parameters with different $R_{\rm TH}$ in the different redshift bins are significant at less than 1.1σ. In all these quoted results, σ is obtained by simply adding the random components of the corresponding reconstruction errors.

As we have discussed previously, with the current mocks, we cannot quantify what will be the contribution of the shot noise errors due to the change in $R_{\rm TH}$. It is interesting however to extract from the $M_B < -18$ mock catalogs what is the difference in the differential change of biasing parameters for $R_{\rm TH} = 8$ and $R_{\rm TH} = 10\,h^{-1}$ Mpc at $l = 5.5\,h^{-1}$ Mpc, the value which is very similar to the mean intergalaxy separation of $M_B < -20 - z$ zCOSMOS galaxies (see Table 1). By "differential change" we refer to the change in the value of a given biasing

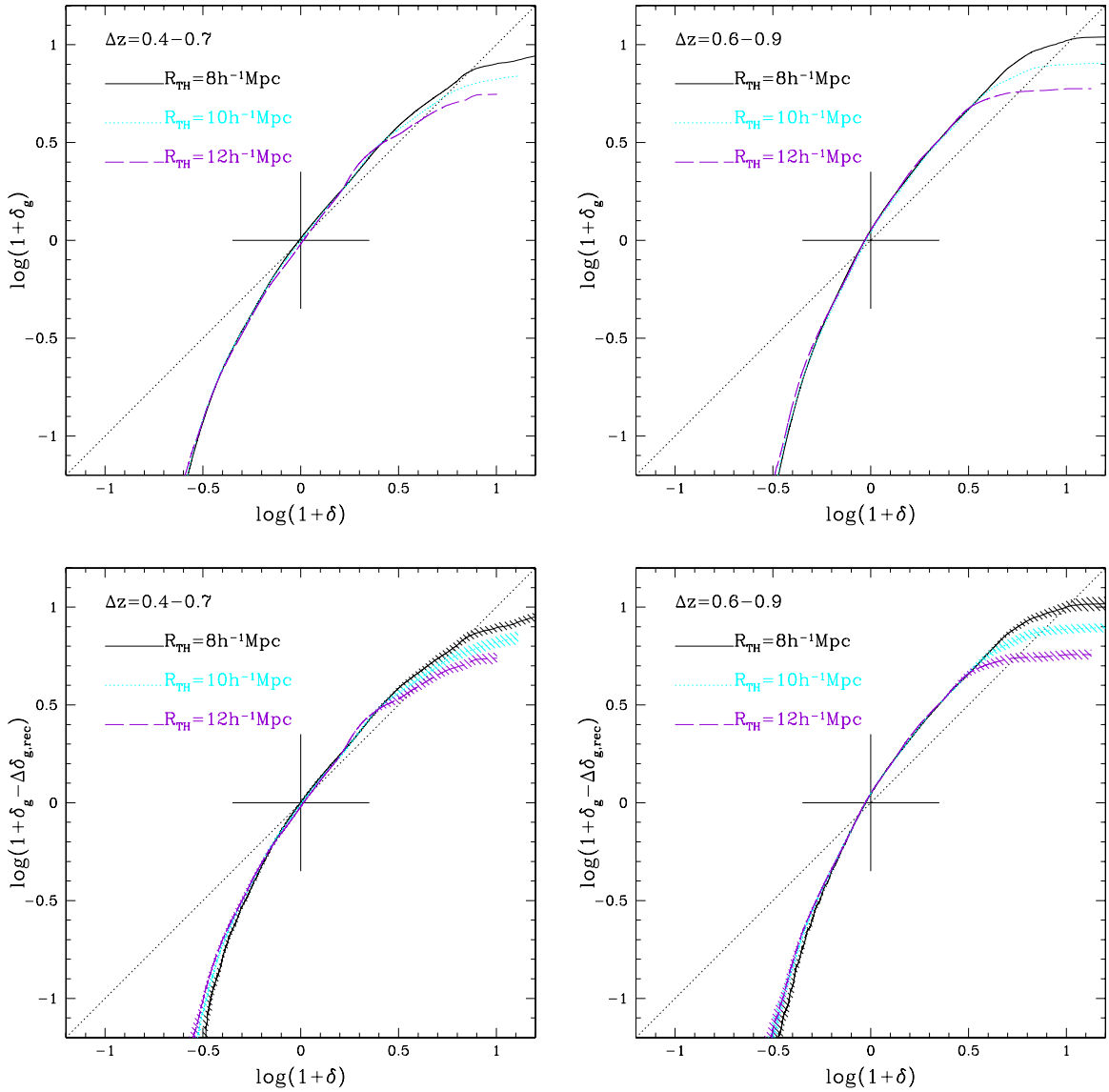

Figure 17. Conditional mean function $\langle\delta_g|\delta\rangle$ for the density field of the zCOSMOS galaxies ($M_B < -20 - z$) obtained by smoothing on various scales. The resulting functions are presented with the black, cyan, and violet lines for the scales of 8, 10, and $12\,h^{-1}$ Mpc, respectively, in two redshift intervals: $0.4 < z < 0.7$ (left) and $0.6 < z < 0.9$ (right). The functions in the top and bottom panels are as measured from the data and when corrected for the systematic reconstruction errors, respectively. We label explicitly the y-axis in the bottom plots to point out this difference. The shaded area in the bottom panels encompasses the 1σ random reconstruction errors in the $\delta_g(\delta)$ values. The shaded area is in the same color as the corresponding $\langle\delta_g|\delta\rangle$ function.

parameter at some l with respect to the same parameter at $l \sim 2.7\,h^{-1}$ Mpc. Averaging the mock results obtained with $l = 5$ and $l = 6\,h^{-1}$ Mpc in Section 4.3, we calculate the difference in the differential shot noise contributions between $\hat{b}$ with $R_{\rm TH} = 8$ and $R_{\rm TH} = 10\,h^{-1}$ Mpc to be 0.014 in $0.4 < z < 0.7$ and 0.017 in $0.7 < z < 1$. Even if we correct the measured differences between the linear biasing parameters obtained for the smoothing scales of 8 and $10\,h^{-1}$ Mpc for these values in the considered lower and upper redshift intervals, respectively, the total differences would still be within the quoted errors. Similarly, for the nonlinearity biasing parameters the differential shot noise contributions between $\tilde{b}/\hat{b}$ with $R_{\rm TH} = 8$ and $R_{\rm TH} = 10\,h^{-1}$ Mpc at $l = 5.5\,h^{-1}$ Mpc are 0.00034 in $0.4 < z < 0.7$ and 0.00035 in $0.7 < z < 1$. This correction will not increase the significance of the measured differences between the zCOSMOS $\tilde{b}/\hat{b}$ parameters with $R_{\rm TH} = 8$ and $R_{\rm TH} = 10\,h^{-1}$ Mpc.

Putting it all together, our results do not provide much evidence in favor of a significant dependence of the derived linear biasing parameter, or of the nonlinearity parameter, on the smoothing scale. However, we have covered only a relatively narrow range in scales and taking the estimated errors into account, we would detect a dependence of the bias on the smoothing scale only if the effect was quite strong.

The negligible dependence of the biasing function and bias parameters on the scales of $8\,h^{-1}$ Mpc and larger is in agreement with the arguments made in a number of theoretical works, in which the bias is expected to be constant on scales larger than a few h^{-1} Mpc (e.g., Kauffmann et al. 1997; Mann et al. 1998; Benson et al. 2000). However, using hydrodynamical simulations Blanton et al. (1999) saw a decrease in galaxy bias with the smoothing scale, where their bias is defined as the ratio between the variances of the number of galaxies and mass within spheres of radius R. This dependence is significant on the

Table 3
Differences between the zCOSMOS Biasing Parameters with the Different $R_{\rm TH}$ for the $M_B < -20 - z$ Sample of Galaxies

$z_{\rm min}$	$z_{\rm max}$	$\lvert\hat{b}(8) - \hat{b}(10)\rvert$	$\lvert\hat{b}_{\Delta\rm rec}(8) - \hat{b}_{\Delta\rm rec}(10)\rvert$	$\lvert\sigma_{\rm rec}(8)\rvert + \lvert\sigma_{\rm rec}(10)\rvert$
0.4	0.7	0.008	0.012	0.069
0.5	0.8	0.005	0.006	0.054
0.6	0.9	0.013	0.012	0.046
$z_{\rm min}$	$z_{\rm max}$	$\lvert\hat{b}(8) - \hat{b}(12)\rvert$	$\lvert\hat{b}_{\Delta\rm rec}(8) - \hat{b}_{\Delta\rm rec}(12)\rvert$	$\lvert\sigma_{\rm rec}(8)\rvert + \lvert\sigma_{\rm rec}(12)\rvert$
0.4	0.7	0.034	0.011	0.076
0.5	0.8	0.033	0.018	0.053
0.6	0.9	0.042	0.041	0.049
$z_{\rm min}$	$z_{\rm max}$	$\lvert\hat{b}(10) - \hat{b}(12)\rvert$	$\lvert\hat{b}_{\Delta\rm rec}(10) - \hat{b}_{\Delta\rm rec}(12)\rvert$	$\lvert\sigma_{\rm rec}(10)\rvert + \lvert\sigma_{\rm rec}(12)\rvert$
0.4	0.7	0.026	0.023	0.074
0.5	0.8	0.038	0.024	0.056
0.6	0.9	0.055	0.030	0.052
$z_{\rm min}$	$z_{\rm max}$	$\lvert\tilde{b}/\hat{b}(8) - \tilde{b}/\hat{b}(10)\rvert$	$\lvert\tilde{b}/\hat{b}_{\Delta\rm rec}(8) - \tilde{b}/\hat{b}_{\Delta\rm rec}(10)\rvert$	$\lvert\sigma_{\rm rec}(8)\rvert + \lvert\sigma_{\rm rec}(10)\rvert$
0.4	0.7	0.0006	0.0005	0.0062
0.5	0.8	0.0012	0.0009	0.0070
0.6	0.9	0.0001	0.0021	0.0065
$z_{\rm min}$	$z_{\rm max}$	$\lvert\tilde{b}/\hat{b}(8) - \tilde{b}/\hat{b}(12)\rvert$	$\lvert\tilde{b}/\hat{b}_{\Delta\rm rec}(8) - \tilde{b}/\hat{b}_{\Delta\rm rec}(12)\rvert$	$\lvert\sigma_{\rm rec}(8)\rvert + \lvert\sigma_{\rm rec}(12)\rvert$
0.4	0.7	0.0023	0.0008	0.0067
0.5	0.8	0.0034	0.0047	0.0099
0.6	0.9	0.0075	0.0067	0.0071
$z_{\rm min}$	$z_{\rm max}$	$\lvert\tilde{b}/\hat{b}(10) - \tilde{b}/\hat{b}(12)\rvert$	$\lvert\tilde{b}/\hat{b}_{\Delta\rm rec}(10) - \tilde{b}/\hat{b}_{\Delta\rm rec}(12)\rvert$	$\lvert\sigma_{\rm rec}(10)\rvert + \lvert\sigma_{\rm rec}(12)\rvert$
0.4	0.7	0.0028	0.0013	0.0073
0.5	0.8	0.0022	0.0038	0.0083
0.6	0.9	0.0076	0.0088	0.0058

Notes. The smoothing radius can take the values 8, 10, and $12\,h^{-1}$ Mpc and this value is indicated in the brackets after the biasing parameters or their errors. The content of the columns is as follows. Columns 1 and 2: lower and upper limits of the redshift bin in which the analysis is carried out, respectively; Columns 3 and 4: absolute values of the differences between the biasing parameters for the two smoothing scales without and with the systematic reconstruction errors, respectively; Column 5: sum of the corresponding random reconstruction errors. The top half of the table corresponds to the results for the linear biasing parameter $\hat{b}$ and the lower part of the table corresponds to the results for the nonlinear biasing parameter $\tilde{b}/\hat{b}$.

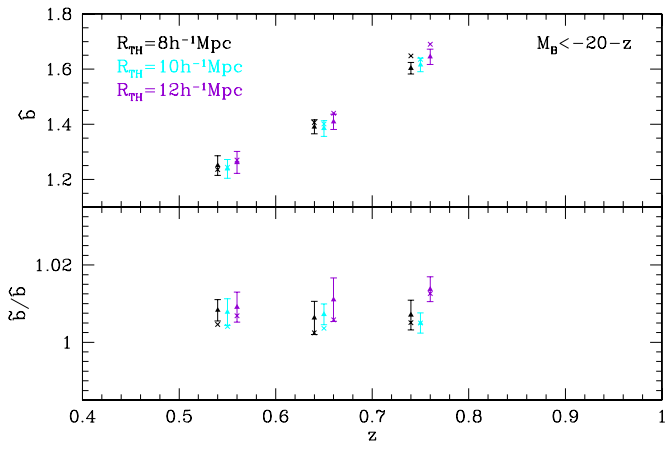

Figure 18. Biasing parameters from the 10k+30kZADE zCOSMOS overdensity field ($M_B < -20 - z$) calculated for the various smoothing scales. The linear biasing parameter $\hat{b}$ is presented in the top panel and the nonlinearity parameter $\tilde{b}/\hat{b}$ is presented in the bottom panel in three redshift bins in which the analysis was carried out. The biasing parameters with and without the systematic reconstruction errors are marked with the solid triangles and crosses, respectively. The vertical error bars correspond to the random reconstruction errors, plotted at the value of a biasing parameter corrected for the systematic reconstruction error. The black, cyan, and violet symbols represent the parameters for the $R_{\rm TH}$ scales of 8, 10, and $12\,h^{-1}$ Mpc, respectively. Some points and their errors are displaced along redshift axis from the mean redshift in the bin where analysis was carried out for the sake of clarity.

scales R smaller than the transition scale between the linear and nonlinear regimes (and it is $16\,h^{-1}$ Mpc in Blanton et al. 1999 simulations). Blanton et al. (1999) explain the scale dependence of the bias to follow from the dependence of the galaxy density field on the local temperature, which reflects the gravitational potential related to the mass density field. If the gas is too hot, galaxies will not form, influencing directly the reconstruction of the galaxy density field.

5.3. Luminosity Dependence

In this subsection, we investigate the dependence of the $\langle\delta_g|\delta\rangle$ function and the biasing parameters on the luminosity of galaxies used to reconstruct the overdensity field, for a fixed smoothing scale of $10\,h^{-1}$ Mpc. The $\langle\delta_g|\delta\rangle$ functions derived with the tracer galaxies of different luminosity thresholds in two redshifts bins ($0.4 < z < 0.7$ and $0.6 < z < 0.9$) are presented in Figure 19, as measured directly from the reconstructed overdensity fields in the top panels, and with the systematic and random reconstruction errors in the bottom panels. We observe a systematic dependence of $\langle\delta_g|\delta\rangle$ on the luminosity of the tracer galaxies, which becomes more pronounced when taking into account the systematic reconstruction errors (bottom panels). In the range from the mildly overdense to the most overdense regions of the mass density contrast, the local bias of more luminous galaxies is higher than the local bias of less luminous

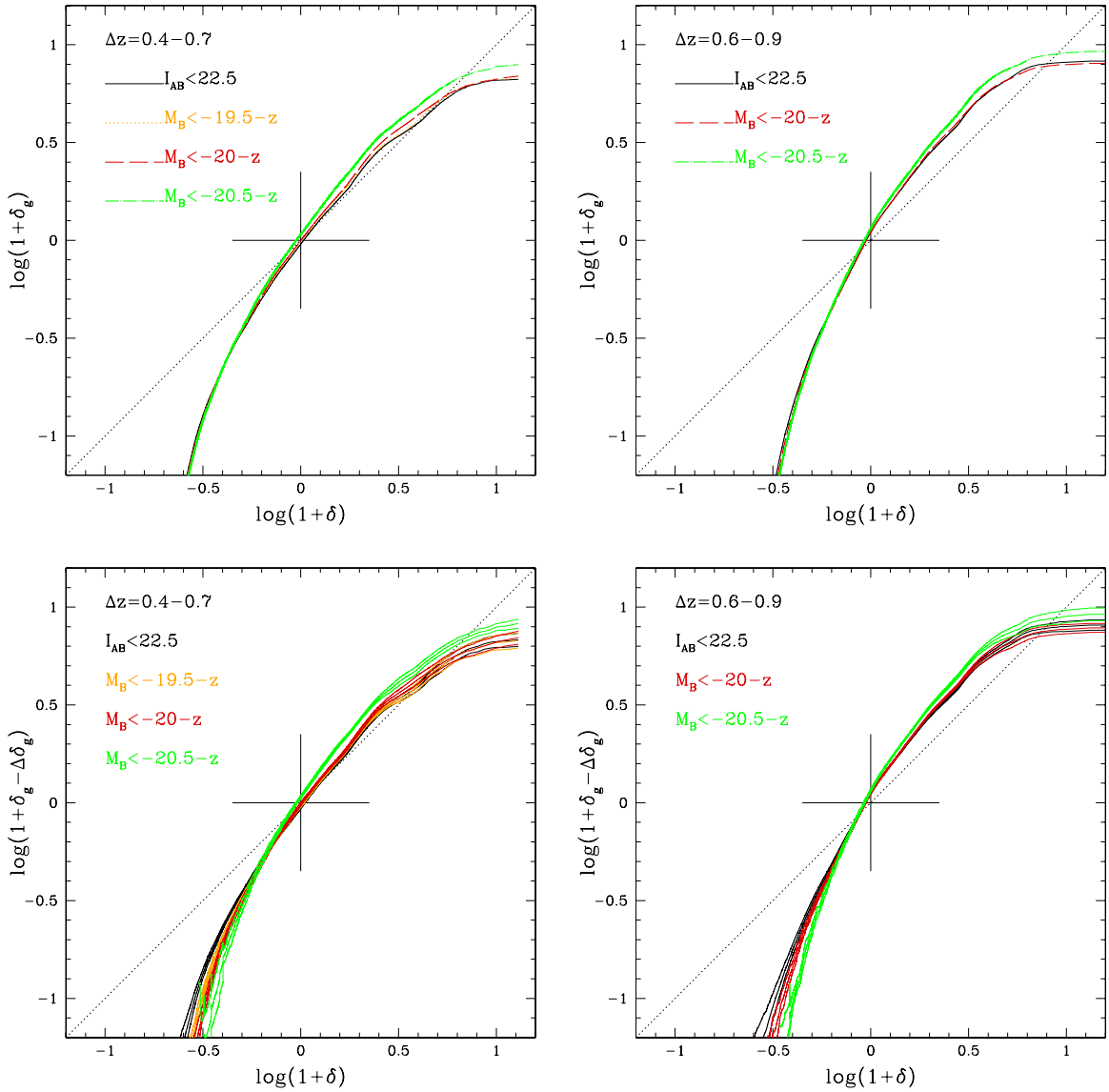

Figure 19. Conditional mean function $\langle\delta_g|\delta\rangle$ for the density field of the 10k+30kZADE zCOSMOS galaxies of various luminosity thresholds obtained by smoothing on a top-hat scale of $10\,h^{-1}$ Mpc. The resulting functions are presented with the black, yellow, red, and green lines for the samples of $I_{AB} < 22.5$, $M_B < -19.5 - z$, $M_B < -20 - z$, and $M_B - 20.5 - z$ galaxies, respectively, in two redshift intervals: $0.4 < z < 0.7$ (left) and $0.6 < z < 0.9$ (right). For the luminosity-complete samples, only results for the samples for which we are complete in a given redshift interval are presented. The functions in the top panels are obtained directly from the data. The middle curves in each set of three curves of the same color in the bottom panels are the measurements with the systematic reconstruction errors. We label explicitly the y-axis in the bottom plots to point out this difference. The upper and lower curves encompassing the $\langle\delta_g|\delta\rangle$ function of the same color in the bottom panels correspond to the 1σ random reconstruction errors in the $\delta_g(\delta)$ values.

galaxies. The same trend for the local bias is again present in the most underdense regions, where $\langle\delta_g|\delta\rangle$ of less luminous galaxies is systematically above $\langle\delta_g|\delta\rangle$ of more luminous galaxies.

We have already mentioned earlier that the mass density contrast at which the galaxy density field no longer traces that of the mass is often interpreted as the mass overdensity threshold (i.e., the critical overdensity δ_c) below which galaxies do not form. Taking into account the random reconstruction errors, the differences between the $\langle\delta_g|\delta\rangle$ functions for the samples of galaxies with different luminosities, corrected for the systematic reconstruction errors, are not highly significant, as seen in the bottom panels in Figure 19. For example, at $\delta = -0.6$ ($\log(1+\delta) \sim -0.4$) in $0.4 < z < 0.7$ the only difference in the $\langle\delta_g|\delta\rangle$ functions more significant than 1σ is between the samples of $M_B < -19.5 - z$ and $M_B < -20.5 - z$ galaxies (at 1.2σ), while in $0.6 < z < 0.9$ the difference between the $\langle\delta_g|\delta\rangle$ functions of $M_B < -20 - z$ and $M_B < -20.5 - z$ galaxies is significant at 2.7σ. Here, σ refers to the sum of the random reconstruction errors for $\delta_g(\delta)$ of the corresponding samples.

The $\langle\delta_g|\delta\rangle$ function in Marinoni et al. (2005) shows the same behavior with luminosity as seen in our results, even though their errors in the most overdense regions are much larger. Moreover, Marinoni et al. (2005) interpret the differentiation of the conditional mean $\langle\delta_g|\delta\rangle$ function with luminosity in the regions of $\delta < 0$ as an indication that the formation efficiency of galaxies is shifting toward higher densities with increasing luminosity.

However, we have shown in Section 4.3 that changing the mean intergalaxy separation by randomly subsampling smaller fractions of the population of tracer galaxies shifts this δ_c "artificially" to higher values. More luminous samples of galaxies have larger mean intergalaxy separations l, and

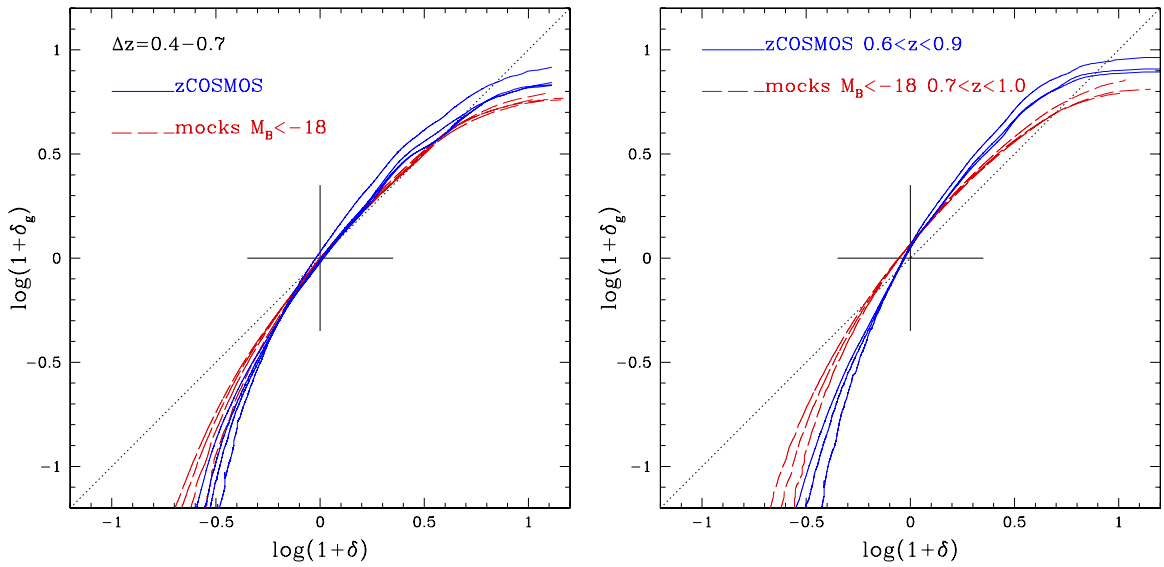

Figure 20. Change in the $\langle\delta_g|\delta\rangle$ function with luminosity and mean intergalaxy separation. Blue curves are the $\langle\delta_g|\delta\rangle$ functions, corrected for the systematic reconstruction errors for the $I_{AB} < 22.5$, $M_B < -19.5 - z$, $M_B < -20 - z$, and $M_B - 20.5 - z$ samples of zCOSMOS galaxies in $0.4 < z < 0.7$ (left panel) and $0.6 < z < 0.9$ (right panel, excluding the sample of $M_B < -19.5 - z$ galaxies) appearing in this order from the left to the right in the underdense regions. The red curves are the $\langle\delta_g|\delta\rangle$ functions for the $M_B < -18$ sample of mock galaxies with l of 4, 5, 6, and $7\,h^{-1}$ Mpc in $0.4 < z < 0.7$ (left panel) and with l of 5, 6, and $7\,h^{-1}$ Mpc in $0.7 < z < 1$ (right panel) appearing in this order from the left to the right in the underdense regions. The plotted zCOSMOS and mock functions encompass the galaxy samples with the similar range of l.

therefore one can expect the purely "shot noise shift" of δ_c to higher values with increasing luminosity. We roughly estimate the order of the expected shot noise caused change in δ_c due to change in luminosity of zCOSMOS galaxies by assuming that this effect is equivalent to the differential change in the mock $\langle\delta_g|\delta\rangle$ functions of the $M_B < -18$ subsamples with similar l values as the mean intergalaxy separations of the zCOSMOS galaxies with different luminosities. We show in Figure 20 the zCOSMOS $\langle\delta_g|\delta\rangle$ functions for the tracers of different luminosities, corrected for the systematic reconstruction errors in two redshift bins (the same functions as in the bottom panels in Figure 19) and the mock $\langle\delta_g|\delta\rangle$ functions with $M_B < -18$ averaged over 12 mocks for $l = 4, 5, 6$, and $7\,h^{-1}$ Mpc in the lower redshift bin and for $l = 5, 6$, and $7\,h^{-1}$ Mpc in the higher redshift bin. These mock l values encompass the range of l of the used samples of zCOSMOS galaxies (the measured l of zCOSMOS galaxies is given in Table 1). The lower redshift bin is $0.4 < z < 0.7$. For the mocks the higher redshift bin is $0.7 < z < 1$, while the zCOSMOS results are given in $0.6 < z < 0.9$ as $z = 0.9$ is the highest redshift up to which $M_B < 20 - z$ sample of galaxies is complete.

A comparison of the curves in Figure 20 shows that in the underdense regions of matter, the differences between the zCOSMOS $\langle\delta_g|\delta\rangle$ functions at some δ_g of the samples with different luminosities are roughly consistent with the differences between the mock $\langle\delta_g|\delta\rangle$ functions at the same δ_g arising due to the change in l only (all mock samples have intrinsically the same bias). If we assume that these mock differential shot noise errors are also correct for the zCOSMOS samples with similar l, the difference in the zCOSMOS $\langle\delta_g|\delta\rangle$ functions (corrected for the systematic reconstruction errors) for the different luminosity samples in the regions of small δ should be mostly ascribable to the shot noise errors. We therefore conclude that there is not much evidence that the observed luminous segregation in $\langle\delta_g|\delta\rangle$ function in the underdense regions is significant.

The linear biasing parameter measured by $\hat{b}$ is shown in the upper panel of Figure 21. The errors in the plot include the

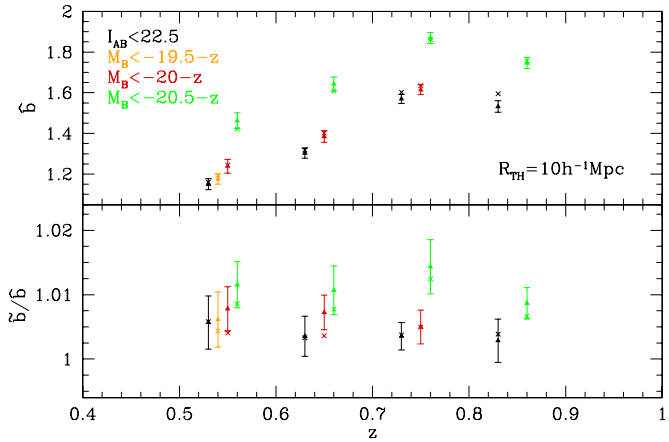

Figure 21. Biasing parameters for the 10k+30kZADE zCOSMOS overdensity field of the various luminosity thresholds. The black, yellow, red, and green symbols represent the parameters for the samples of $I_{AB} < 22.5$, $M_B < -19.5 - z$, $M_B < -20 - z$, and $M_B - 20.5 - z$ galaxies, respectively, all with $R_{\rm TH} = 10\,h^{-1}$ Mpc. For the luminosity-complete samples, only results for the samples for which we are complete in a given redshift interval are presented. Details are the same as in Figure 18.

systematic and random reconstruction errors. The $\hat{b}$ parameter shows a systematic dependence on the luminosity of the tracers: it is higher for the more luminous galaxies. The difference between the linear biasing parameters $\hat{b}$ of $M_B < -20.5 - z$ and $M_B < -20 - z$ samples of galaxies (corrected for the systematic reconstruction error) is significant at 2.8σ, 3.5σ, and 3.9σ in $0.4 < z < 0.7$, $0.5 < z < 0.8$, and $0.6 < z < 0.9$, respectively. While the difference between $\hat{b}$ of $M_B < -20 - z$ and $M_B < -19.5 - z$ galaxies at $0.4 < z < 0.7$ is only 1.1σ, the difference between $\hat{b}$ of $M_B < -20.5 - z$ and $M_B < -19.5 - z$ galaxies in the same redshift interval is 4.2σ. Here, we refer to σ as the sum of the random components of the reconstruction errors. The differences between the linear biasing parameters for all possible combinations of lumi-

Table 4
Differences between the zCOSMOS Biasing Parameters Measured with the Tracer Galaxies of Different Luminosities for $R_{\rm TH} = 10\,h^{-1}$ Mpc

$z_{\rm min}$	$z_{\rm max}$	Tracers1	Tracers2	$\lvert\mathrm{Diff}\,\hat{b}\rvert$	$\lvert\mathrm{Diff}\,\hat{b}_{\Delta\rm rec}\rvert$	$\Sigma\,\lvert\sigma_{\rm rec}\rvert$	$\Delta_{\rm SN}$	$\lvert\sigma_{\rm SN}\rvert$
0.4	0.7	−19.5-z	Flux	0.0320	0.0250	0.0511	−0.0014	0.0005
0.4	0.7	−20.0-z	Flux	0.0838	0.0882	0.0605	−0.0018	0.0021
0.4	0.7	−20.0-z	−19.5-z	0.0517	0.0632	0.0583	−0.0003	0.0017
0.4	0.7	−20.5-z	Flux	0.2406	0.2919	0.0655	0.0028	0.0059
0.4	0.7	−20.5-z	−19.5-z	0.2086	0.2668	0.0634	0.0042	0.0054
0.4	0.7	−20.5-z	−20-z	0.1569	0.2036	0.0727	0.0046	0.0038
0.5	0.8	−20.0-z	Flux	0.0834	0.0814	0.0537	0.0003	0.0037
0.5	0.8	−20.5-z	Flux	0.2524	0.3001	0.0596	0.0045	0.0071
0.5	0.8	−20.5-z	−20-z	0.1690	0.2188	0.0626	0.00414	0.0034
0.6	0.9	−20.0-z	Flux	0.0333	0.0452	0.0468	0.0012	0.0014
0.6	0.9	−20.5-z	Flux	0.2094	0.2485	0.0494	0.0087	0.0108
0.6	0.9	−20.5-z	−20-z	0.1761	0.2034	0.0516	0.0075	0.0094
0.7	1.0	−20.5-z	Flux	0.1400	0.1912	0.0561	0.0028	0.0058
$z_{\rm min}$	$z_{\rm max}$	Tracers1	Tracers2	$\lvert\mathrm{Diff}\,\tilde{b}/\hat{b}\rvert$	$\lvert\mathrm{Diff}\,\tilde{b}/\hat{b}_{\Delta\rm rec}\rvert$	$\Sigma\,\lvert\sigma_{\rm rec}\rvert$	$\Delta_{\rm SN}$	$\lvert\sigma_{\rm SN}\rvert$
0.4	0.7	−19.5-z	Flux	0.0084	0.0114	0.0048	−0.0011	0.0021
0.4	0.7	−20.0-z	Flux	0.0076	0.0298	0.0127	−0.0021	0.0021
0.4	0.7	−20.0-z	−19.5-z	0.0077	0.0185	0.0079	−0.0010	0.0021
0.4	0.7	−20.5-z	Flux	0.0077	0.0827	0.0352	−0.0036	0.0021
0.4	0.7	−20.5-z	−19.5-z	0.0079	0.0713	0.0304	−0.0025	0.0021
0.4	0.7	−20.5-z	−20.0-z	0.0070	0.0529	0.0225	−0.0015	0.0021
0.5	0.8	−20.0-z	Flux	0.0058	0.0287	0.0083	−0.0016	0.0021
0.5	0.8	−20.5-z	Flux	0.0069	0.0926	0.0268	−0.0033	0.0021
0.5	0.8	−20.5-z	−20.0-z	0.0065	0.0639	0.0185	−0.0016	0.0021
0.6	0.9	−20.0-z	Flux	0.0048	0.0239	0.0060	−0.0011	0.0018
0.6	0.9	−20.5-z	Flux	0.0063	0.0980	0.0244	−0.0028	0.0018
0.6	0.9	−20.5-z	−20.0-z	0.0069	0.0741	0.0185	−0.0017	0.0018
0.7	1.0	−20.5-z	Flux	0.0058	0.0938	0.0267	−0.0020	0.0016

Notes. The content of the columns is as follows. Columns 1 and 2: lower and upper limits of the redshift bin in which the analysis is carried out, respectively; Columns 3 and 4: luminosities of the tracer galaxies; Columns 5 and 6: absolute values of the differences between the biasing parameters of the tracers in the third and fourth columns without and with the systematic reconstruction errors, respectively; Column 7: sum of the corresponding random reconstruction errors; Column 8: systematic differential shot noise error expected from the difference in the mean intergalaxy separations of the two tracer populations; Column 9: random differential shot noise error. To obtain the difference between the biasing parameters corrected for the differential shot noise error, the correction given in Column 8 should be subtracted from the differences given in Column 5 or 6. The top half of the table corresponds to the results for the linear biasing parameter $\hat{b}$ and the lower part of the table corresponds to the results for the nonlinear biasing parameter $\tilde{b}/\hat{b}$.

nosity limits, and the errors on these differences, are given in Table 4.

If we assume for a moment that all samples of tracer galaxies are equally biased tracers of the matter, we can roughly estimate what would be the change in $\hat{b}$ just due to the change in l at a given $R_{\rm TH}$ exploring the results presented in Section 4.3. Using Equation (22) for $R_{\rm TH} = 10\,h^{-1}$ Mpc, we calculate what would be the expected contribution in the difference between the $\hat{b}$ parameters of the various samples of tracer galaxies just due to the different l of the considered tracers, $\Delta_{\rm SN}$. The expected systematic differences ($\Delta_{\rm SN}$) and their errors ($\sigma_{\rm SN}$), propagated from the fit to Equation (22), are also given in Table 4 (Columns 8 and 9, respectively). Taking then both the systematic and random components of the shot noise errors into account, the significance of the differences of $\hat{b}$ parameters with luminosity becomes lower. However, the $\hat{b}$ parameters of $M_B < -20.5 - z$ and $M_B < -20 - z$ samples of galaxies still differ at 1.6σ, 1.9σ, and 1.8σ in $0.4 < z < 0.7$, $0.5 < z < 0.8$, and $0.6 < z < 0.9$, respectively. The quoted σ includes also the corresponding random shot noise error.

To conclude, as we observe that the trends in the change of $\hat{b}$ with luminosity are systematic, and for some samples always significant at more than 1.5σ, we are confident that the trend of increasing $\hat{b}$ with luminosity reflects intrinsic physical processes in galaxy formation. The dependence of the correlation function on the luminosity is a well-known observational result (e.g., Zehavi et al. 2005; Pollo et al. 2006; Coil et al. 2008; but see Meneux et al. 2009), therefore an increase in the linear bias with luminosity is expected.

The equivalent results for the nonlinearity parameter $\tilde{b}/\hat{b}$ are shown in the lower panel of Figure 21 and in Table 4. Again, the $\tilde{b}/\hat{b}$ values are systematically larger for the $M_B < -20.5 - z$ than the $M_B < -20 - z$ sample of galaxies, but the differences are significant at more than 1σ only in $0.6 < z < 0.9$. This significance is 1.4σ with respect to the reconstruction errors or 1.3σ when adding also the differential shot noise errors (estimated from Equation (23)) to the reconstruction errors.

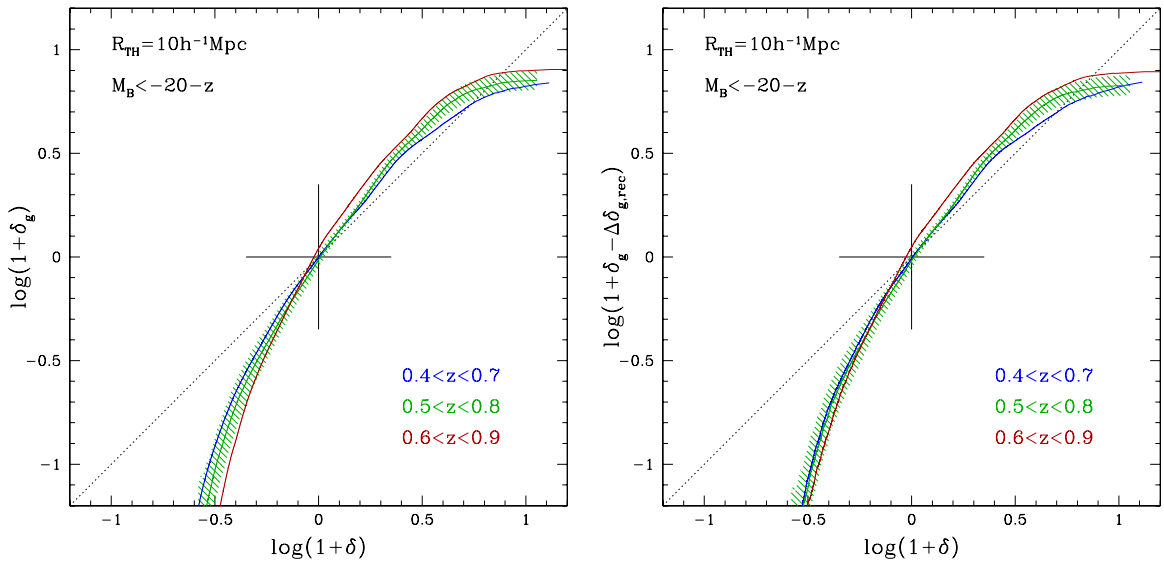

Figure 22. Redshift evolution of the conditional mean $\langle\delta_g|\delta\rangle$ function. The resulting functions are presented in blue, green, and red lines for the sample of $M_B < -20-z$ galaxies and $R_{\rm TH} = 10\,h^{-1}$ Mpc in $0.4 < z < 0.7$, $0.5 < z < 0.8$, and $0.6 < z < 0.9$, respectively. The $\langle\delta_g|\delta\rangle$ functions without and with the systematic reconstruction errors are plotted in the left and right panels, respectively. The shaded area corresponds to the 1σ cosmic variance error in the $\delta_g(\delta)$ or $\delta_g(\delta) - \Delta\delta_{g,\rm rec}(\delta)$ values in the left and right panels, respectively (i.e., it encloses the errors along the y-axis). The shaded area in the underdense regions with δ smaller than the smallest δ value for which the $\langle\delta_g|\delta\rangle$ function is plotted is a part of the cosmic variance errors for $\delta_g(\delta)$, not visible on the plot. For clarity, the cosmic variance errors are plotted only for the functions in $0.5 < z < 0.8$. The cosmic variance errors have similar values in the other redshift bins.

Based on these results, we conclude that the zCOSMOS data do not provide evidence for a significant dependence of the biasing nonlinearity parameter on the luminosity of tracer galaxies.

5.4. Redshift Evolution

The evolution of the conditional mean function $\langle\delta_g|\delta\rangle$ and biasing parameters with redshift can be studied in all results presented so far. Here, we briefly summarize those.

At a given luminosity and smoothing scale, the basic shape of the $\langle\delta_g|\delta\rangle$ function (e.g., Figures 15 and 16) is preserved in all three redshifts bins probed by the overdensity field traced by the 10k+30kZADE zCOSMOS galaxies. To highlight the possible differences, we plot the $\langle\delta_g|\delta\rangle$ functions of the sample of $M_B < -20-z$ galaxies, smoothed with $R_{\rm TH} = 10\,h^{-1}$ Mpc, from all three redshift bins in a single panel in Figure 22. There is a systematic shift in the $\langle\delta_g|\delta\rangle$ function from one redshift bin to another, indicating an increase of the local bias with redshift. The statement is valid for the $\langle\delta_g|\delta\rangle$ functions measured both directly from the data and when corrected for the systematic reconstruction errors, though the redshift evolution in the underdense regions is almost negligible after correction for the systematic reconstruction errors. Galaxies also become antibiased at gradually higher matter overdensities when going from lower to higher redshifts. However, with respect to the cosmic variance errors, which are the relevant errors in comparison of the results over the various redshift bins, the significance of any of the above statements is less than 1σ.

On the other hand, the evolution of the mean biasing parameter $\hat{b}$ with redshift is clearly evident (top panels in Figures 18 and 21). This should not be surprising with respect to the weak redshift evolution in the shape of the $\langle\delta_g|\delta\rangle$ function, as to measure the second moments in the mean biasing function, the expectation values in Equations (6) and (7) are taken from the probability distribution of the corresponding density fields. To assess the significance of the redshift evolution in the linear bias, one needs to take into account the cosmic variance errors. For example, the $\hat{b}$ parameter, corrected for the systematic reconstruction error, increases from 1.23 ± 0.11 at $z \sim 0.55$ to 1.62 ± 0.14 at $z \sim 0.75$ for the $M_B < -20-z$ sample of galaxies for the top-hat smoothing of $10\,h^{-1}$ Mpc, meaning that the redshift evolution between the lowest and the highest redshift bin is significant (measurements for $\hat{b}$ and its corresponding cosmic variance errors are given in Table 2). Obviously, the significance of the redshift evolution in $\hat{b}$ is much lower than what would be obtained by calculating its significance using the random reconstruction errors, which are shown in the relevant Figures 18 and 21.

The nonlinearity of the mean biasing function as measured by $\tilde{b}/\hat{b}$ is the least affected by the shot noise and reconstruction errors. The nonlinearity parameter does not show any significant redshift evolution, in addition to no dependence on the smoothing scale or on the luminosity limit of galaxies used to reconstruct the overdensity field (bottom panels in Figures 18 and 21). The $\tilde{b}/\hat{b}$ is offset from unity by a maximum of 2%, with errors of the same order. The values of all biasing parameters and their errors are given in Table 2.

The observed significant redshift evolution of the zCOSMOS linear biasing parameter supports the theoretical predictions for the bias evolution. To put our results in the context of the theoretical works, we briefly summarize below different effects which can be responsible for this bias behavior, as already discussed by Blanton et al. (2000). First, galaxy formation process shifts from the highest peaks in the density field at early epoch to the lower peaks in the density field as time progresses, i.e., this process shifts from the most biased to less biased tracers of the underlying density field. Second, the formation of galaxies in the most dense environments is halted toward lower redshifts, because these regions become filled with gas which is shock heated and virialized, but which is not able to cool and collapse. At higher redshifts ($z \sim 3$) galaxies are expected to be biased even in the highest density regions, because they are still sufficiently cold enough to allow for fast cooling of

the clumps of gas. These two effects combined are responsible for the shift in the galaxy formation from the most dense to less dense environments. Third, once galaxies are formed, they experience the same gravitational physics as the dark matter, and therefore the distribution of galaxies and matter becomes more and more similar (Fry 1996; Tegmark & Peebles 1998).

6. COMPARISON TO PREVIOUS WORK

The zCOSMOS biasing results are in qualitative agreement with the biasing framework extracted from the ΛCDM models and with a previous study of similar type based on the VVDS data. In order to put some tighter constraints on the models of galaxy formation and evolution, it is important to carry out more exact comparisons with previous results. For this purpose, we use only the linear biasing parameter, which is much easier to compare.

6.1. Linear Bias from the Nonlinear Biasing Analysis

In the study of the (nonlinear) biasing of the VVDS galaxies, Marinoni et al. (2005) assumed a cosmological model described by $\Omega_{m,0} = 0.3$, $\Omega_{\Lambda,0} = 0.7$, and $\sigma_8 = 0.9$. Moreover, they use the $\tilde{b}$ parameter as the linear biasing parameter. For a proper comparison with our linear biasing parameter $\hat{b}$, we infer $\hat{b}$ from the values of $\tilde{b}$ and nonlinearity parameters published in Marinoni et al. (2005) and correct it for the difference in the used σ_8 normalization, following the correction given by SBD. The comparison of linear biasing parameters from the zCOSMOS and VVDS is presented in Figure 23. We use the errors for the $\tilde{b}$ parameter in Marinoni et al. (2005) as a proxy for the errors of the inferred $\hat{b}$ parameter. Even with this effort our comparison to the results from the VVDS is still only approximate. Complications arise from the different luminosity-complete samples used for the analyses. Moreover, Marinoni et al. (2005) use a non-evolving magnitude to define the samples of tracer galaxies, while we use an evolving magnitude cut.

As a local reference in Figure 23, we use the bias obtained from the bispectrum of the 2dFGRS galaxies measured by Verde et al. (2002). We take their b_1 values (following the Fry & Gaztanaga 1993 bias description, see Equation (4)) as a proxy for the linear biasing parameter, derived for L^* galaxies. Norberg et al. (2001) detected a clear increase of the biasing parameter b_ξ (from the clustering analysis) with luminosity L of galaxies, described well by $\frac{b_\xi}{b_\xi^*} = 0.85 + 0.15\frac{L}{L^*}$, where b_ξ^* is the bias for the L^* galaxies. Using this relation, we calculate the bias of the sample of $M_B < -20 - z$ galaxies at the effective redshift of 2dFGRS survey $z = 0.17$ (Verde et al. 2002), taking for L the median luminosity of all $M_B < -20 - z$ zCOSMOS tracer galaxies. We use the prescription from Norberg et al. (2002) for the transformation from our B to the 2dFGRS b_j filter at the median $B-V$ color of $M_B < -20 - z$ zCOSMOS tracer galaxies with secure redshifts. Moreover, Gaztañaga et al. (2005) measure the three-point correlation function in the 2dFGRS and estimate the bias parameters from the correlations on weakly nonlinear scales (6–27 h^{-1} Mpc). They find that their best measurement of the linear bias, i.e., b_1 term, of $-21.77 < M_{b_j} < -20.77$ galaxies (using here $h = 0.7$ for magnitudes) agrees well with that of Verde et al. (2002), and therefore we do not include this measurement in Figure 23. We stress that the measurement by Verde et al. (2002) is derived in Fourier space, from a flux-limited and volume-weighted sample, and for scales larger than 13 h^{-1} Mpc. It is anyway reassuring

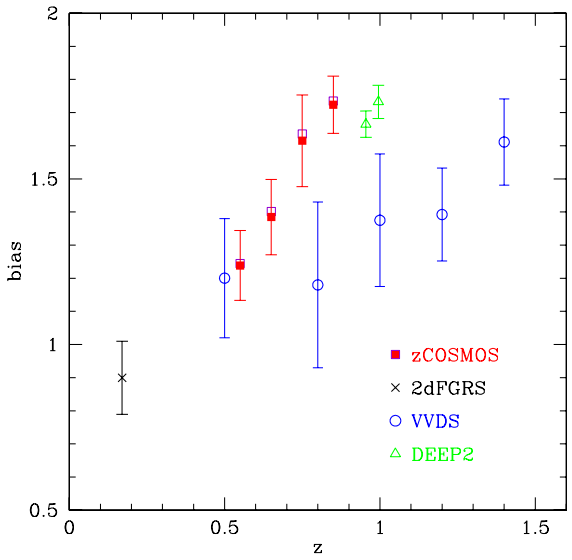

Figure 23. Comparison of the zCOSMOS linear biasing parameters to the bias values from similar analyses available in the literature. The filled squares correspond to the zCOSMOS measurements of $\hat{b} - \Delta\hat{b}_{\rm rec}$, where the underlying empty squares are the $\hat{b}$ values as measured from the zCOSMOS overdensity field. The zCOSMOS error bars correspond to the cosmic variance errors. The empty circles are the $\hat{b}$ values based on the nonlinear biasing analysis in the VVDS (Marinoni et al. 2005) and the cross is the b_1 value from the 2dFGRS (Verde et al. 2002). The zCOSMOS points are presented at the mean redshift of the bins $\Delta z = 0.3$ wide. The three lower z points are calculated for the $M_B < -20 - z$ sample, while the $z \sim 0.85$ point is for the $M_B < -20.5 - z$ sample and the smoothing scale is $R = 10\,h^{-1}$ Mpc for all the points. The biasing values from the VVDS are inferred from the overdensity field reconstructed using a sample with $M_B < -20.77$ on the $R = 5\,h^{-1}$ Mpc scale in $0.4 < z < 0.7$ and on the $R = 10\,h^{-1}$ Mpc scale in $0.7 < z < 0.9$, $0.9 < z < 1.1$, $1.1 < z < 1.3$, and $1.3 < z < 1.5$. The VVDS points are plotted at the center of the corresponding bin, with the exception of the lowest z point, offset along the redshift axis due to clarity by -0.05. The b_1 value from the 2dFGRS is recalculated for $M_B < -20 - z$ galaxies at $z = 0.17$, which is the effective redshift of 2dFGRS. For comparison, we add linear bias values obtained from the clustering statistics in the DEEP2 (Coil et al. 2006), represented as triangles. The DEEP2 bias is plotted at the mean redshift of the $0.75 < z < 1.2$ interval used for the analysis, offset along the redshift axis due to clarity by -0.02 for the $M_B < -20.77$ sample and by $+0.02$ for the $M_B < -21.27$ sample of galaxies. See the text for more details.

(A color version of this figure is available in the online journal.)

that it agrees (within the quoted uncertainties) with the real space study based on a volume-limited sample by Gaztañaga et al. (2005). It is interesting to point out here that the measurements of the nonlinear bias component (i.e., quadratic bias) by Verde et al. (2002) and Gaztañaga et al. (2005) differ significantly. While the results of Verde et al. (2002) are consistent with the linear bias model, Gaztañaga et al. (2005) detect a 3σ non-zero value of the quadratic bias (see Section 5 in Gaztañaga et al. 2005 for a detailed discussion of the possible sources of this discrepancy).

From Figure 23, it is clear that the linear bias values measured from the zCOSMOS and VVDS surveys at $z > 0.4$ are higher than the linear bias measured in the local universe. At $z \sim 0.55$, the mean redshift of the lowest explored bin of both the zCOSMOS and the VVDS surveys, there is excellent agreement between the linear biasing parameters from the two surveys. However, the evolution of the linear biasing seems to be happening at different rate at higher redshifts. While in zCOSMOS we detect a constant increase in the linear biasing parameter of about 0.15–0.2 per $\Delta z = 0.1$ for the galaxies of the similar evolved luminosity, the VVDS results suggest a slower

increase of the linear biasing parameter of about 0.1 or less per $\Delta z = 0.1$.

The most probable explanation of this difference, apart from the various techniques used for the density field reconstruction, cosmological density parameters, galaxy samples etc., lies in the observed fields themselves. For instance, the COSMOS volume is dominated by large density fluctuations over the full redshift range probed by the zCOSMOS. Large structures dominate the whole zCOSMOS field even at redshifts of $z \sim 0.9$ (Kovač et al. 2010a). When compared to the mock catalogs, the size of structures in the zCOSMOS galaxy density field points out that the COSMOS field is in the upper tail of the cosmic variance distribution (Kovač et al. 2010a), indicated also by the other studies (McCracken et al. 2007; Meneux et al. 2009). On the other hand, the VVDS field is in the lower tail of the cosmic variance distribution (Meneux et al. 2009). Moreover, as we have already mentioned, the field used in the VVDS analysis is smaller than the zCOSMOS field and the uncertainty in the redshift precision in the VVDS is about three times larger than in the zCOSMOS. Nevertheless, the exact bias values and their redshift evolution should be explored further.

To complete the comparison, we add in Figure 23 linear bias values obtained from the clustering analysis in the DEEP2 survey in $0.75 < z < 1.2$ with $M_B < -20.77$ and $M_B < -21.27$ samples of galaxies (using here $h = 0.7$ for magnitudes) in the range of projected scales $r_p = 1$–$10\,h^{-1}$ Mpc (Coil et al. 2006). These bias values fall between the zCOSMOS and VVDS measurements; however, these are bias values obtained from the different statistics. We will discuss in more details the bias obtained from the clustering analysis in the following section.

6.2. Linear Bias from Clustering Studies

As discussed in the Introduction, clustering studies are commonly used to derive the linear biasing parameter. One needs to keep in mind that the linear bias inferred from the clustering analysis and from the analysis of the second moments of the $\langle \delta_g | \delta \rangle$ function is not exactly the same quantity. In some sense, b_ξ is differential, calculated at a given distance r_p, while the biasing parameter from our analysis $\hat{b}$ is some weighted average over the smoothing scale R. Moreover, in recent clustering studies, linear bias is derived by using simultaneously correlation values at a range of r_p, leading to a value of the linear biasing parameter more comparable to our approach. In addition, the difference between $\hat{b}$ and b_ξ also reflects the physical factors such as stochasticity and nonlinearity (e.g., Somerville et al. 2001). For example, at $z = 0$ Somerville et al. (2001) find that b_ξ is systematically higher than $\hat{b}$ for about 10%–20% for the ΛCDM cosmology for the $M_B < -20.27$ sample of (mock) galaxies.

Meneux et al. (2009) study the dependence of clustering of the 10k zCOSMOS galaxies on their luminosity for the various evolving-luminosity-complete samples in $0.4 < z < 1$. The measured dependence of the projected correlation function on the luminosity of galaxies is very weak and without any coherent redshift evolution in the amplitude or shape. From the comparison of the correlation function of $M_B < -20.27 - z$ galaxies (presented in Meneux et al. 2009, using here $h = 0.7$ for magnitudes) to the correlation function of dark matter (Smith et al. 2003) in $0.5 < z < 1$, it has been inferred that these galaxies are consistent with biasing $b_\xi \sim 1.81$ at small scales, while at large scales $R > 8\,h^{-1}$ Mpc the clustering analysis requires $b_\xi \sim 2.25$ (correcting the b_ξ values to $\sigma_8 = 0.8$). The high biasing value at large scales is explained to reflect the relatively small transverse size of the zCOSMOS field with respect to the size of the structures, as the derived correlation function is not a power law (see, e.g., Figure 19 in Meneux et al. 2009). The zCOSMOS b_ξ inferred from the sample of $M_B < -20.27 - z$ galaxies in $0.5 < z < 1$ at $r_p \approx 10\,h^{-1}$ Mpc (Meneux et al. 2009) is larger for about 50% and 31% than the $\hat{b}$ measured here for the samples of $M_B < -20 - z$ (averaged over $0.5 < z < 0.9$) and $M_B < -20.5 - z$ galaxies (averaged over $0.5 < z < 1$) with $R = 10\,h^{-1}$ Mpc, respectively. For the smaller r_p scales, this b_ξ value is larger for about 21% and 6% than $\hat{b}$ for the same zCOSMOS samples as above.

It is of interest to note here that Meneux et al. (2009) compare the correlation function of the zCOSMOS and VVDS galaxies (Meneux et al. 2008), finding that the bias inferred from clustering of $\log(M_*/M_\odot) \geqslant 10$ galaxies in $0.5 < z < 1$ is systematically higher for the zCOSMOS than VVDS galaxies. The observed difference is fully consistent with the difference between the linear biasing parameters derived from the nonlinear biasing analysis in these two surveys, as shown here (e.g., Figure 23).

Using the full DEEP2 sample, Coil et al. (2006) measure the increase of b_ξ with luminosity on both small and large scales, where the trend is stronger on smaller scales. The measured bias b_ξ takes values from 1.42 ± 0.04 for the $M_B < -19.77$ sample at $0.75 < z < 1$ to 1.67 ± 0.04 for the $M_B < -20.77$ sample at $0.75 < z < 1.2$, or to 1.73 ± 0.05 for the $M_B < -21.27$ sample of galaxies at $0.75 < z < 1.2$ (using here $h = 0.7$ for magnitudes), derived simultaneously for the range of scales $r_p = 1$–$10\,h^{-1}$ Mpc. We have increased the bias values quoted in Coil et al. (2006) by ∼13% in order to correct for the different σ_8 used. The values of the most luminous DEEP2 samples of Coil et al. (2006) are comparable to our $\hat{b}$ values of the two most luminous samples at $z \geqslant 0.6$, and they are higher than any of the $\hat{b}$ values inferred from the VVDS sample of $M_B < -20.77$ galaxies in $0.7 < z < 1.5$ (see Figure 23). Moreover, the DEEP2 sample is complete for the red $M_B < -21.27$ galaxies only up to $z = 1.05$ (Coil et al. 2008). These galaxies are more biased than the blue galaxies (e.g., Coil et al. 2008) and therefore the value of bias for the $M_B < -21.27$ DEEP2 galaxies can be partially lower due to this effect (our luminosity-complete samples are chosen to be also color complete).

The comparison of the zCOSMOS linear bias measured in this work to the previous biasing analyses based both on the clustering and moments statistics leads us to conclude that the cosmic variance is the main contributor to the different bias values and the different rate of the redshift evolution of bias of galaxies with similar luminosities in the existing $0.4 \lesssim z \lesssim 1.5$ spectroscopic surveys. Our future work is oriented toward quantifying the systematic contribution of the cosmic variance in the zCOSMOS field (e.g., de la Torre et al. 2011) and we will put stronger constraints from the presented biasing analysis only after being able to correct for this systematic effect.

6.3. Bias of the Dark Matter Halos

From the observed bias of the zCOSMOS galaxies we can infer a characteristic mass of dark matter halos that host these galaxies. In the ideal case, we would compare the measured galaxy bias to the bias of halos estimated from the halo overdensity field. In the absence of such results, we will use the standard approximations for the bias of halos of a given

mass M_h and redshift z. Under the assumption that the observed galaxies are central galaxies of a halo, the measured bias (which we showed does not depend on the scale of 8–12 h^{-1} Mpc used to reconstruct the galaxy density field) can be matched to the bias of the dark matter halos. With this assumption (no satellite galaxies), the inferred characteristic halo mass at a given bias value will be higher than the true halo mass (e.g., Zheng et al. 2007). This is not that important for our calculations, as on scales larger than the halo sizes the bias depends only on the mean mass of the host halos and this is what we measure. The other uncertainty comes from the fact that we are comparing bias of galaxies above a given luminosity with a bias of halos of a given mass. Having in mind all the approximations mentioned above, the results on the typical halo masses of the zCOSMOS galaxies should be understood only as indicative.

We use two approximations for the bias–halo mass relations given by Sheth et al. (2001) and Pillepich et al. (2010), to also highlight theoretical uncertainties in these fits. First, we calculate for the adopted cosmology the halo bias for the range of halo masses at redshifts 0.55, 0.65, 0.75, and 0.85, which are the mean redshifts of the redshift intervals used in our analysis. We start from the simplest scenario, in which galaxies of a given type reside always in halos of the same mass. For the sample of $M_B < -20 - z$ galaxies and $R = 10\,h^{-1}$ Mpc, we find by χ^2-minimization of differences between the bias of galaxies and halos at different redshifts that the best-fit mass of dark halos to host this sample is $\sim 2.6 \times 10^{12}\,h^{-1}\,M_\odot$ or $\sim 5.6 \times 10^{12}\,h^{-1}\,M_\odot$, when using the Sheth et al. (2001) or Pillepich et al. (2010) bias expressions, respectively. In this process, we used linear bias values $\hat{b}$ corrected for the systematic reconstruction errors and cosmic variance errors.

The redshift evolution of linear bias of $\sim 2.6 \times 10^{12}\,h^{-1}\,M_\odot$ and $\sim 5.6 \times 10^{12}\,h^{-1}\,M_\odot$ halos following Sheth et al. (2001) and Pillepich et al. (2010), respectively, is presented in Figure 24, along with the measured redshift evolution of linear bias (corrected for the systematic reconstruction errors) of the $M_B < -20 - z$ zCOSMOS galaxies. The models of halo biasing approximately describe the observed evolution of galaxian biasing, where the difference falls almost completely within the 1σ cosmic variance errors of the galaxy bias.

The considered (halo) biasing models include the effect of the merging of halos. For comparison, we calculate also the evolution of biasing using the so-called galaxy conserving model (e.g., Fry 1996), in which the number of galaxies is preserved over cosmic time (no merging). Here, we assume that the model bias at the redshifts of zCOSMOS observations is given by the bias of $M_B < -20 - z$ zCOSMOS galaxies at the $R = 10\,h^{-1}$ Mpc scale. The results are included in Figure 24. The conserving model produces too high values of biasing at low z. This is a known result in the biasing analysis, indicating that merging is an important ingredient in the biasing of cosmic structures. Commonly, the difference in the evolution of halo and galaxy biasing (e.g., black points and red/blue curves in Figure 24) are attributed to the different timescales of mergers of galaxies and halos, as well as the evolution in mass-to-light ratios between halos and galaxies (e.g., Somerville et al. 2001). For a precise answer on the difference in the evolution of galaxian and halo bias, the broader baseline in redshift is needed.

If we consider a different scenario, in which the galaxies defined by their evolving B-band magnitude reside in halos of different mass at different redshifts, we find that the characteristic mass of a halo (i.e., the halo mass at which the halo bias matches the bias of galaxies, latter one corrected for the

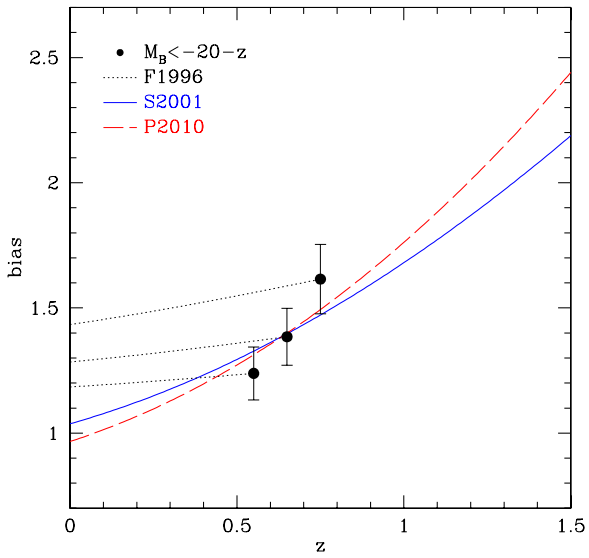

Figure 24. Redshift evolution of the bias of $M_B < -20 - z$ galaxies (filled circles), $2.6 \times 10^{12}\,h^{-1}\,M_\odot$ dark matter halos following the Sheth et al. (2001, S2001) expression for halo biasing (continuous line), and $5.6 \times 10^{12}\,h^{-1}\,M_\odot$ dark matter halos following the Pillepich et al. (2010, P2010) expression for halo biasing (dashed line). The evolution of biasing of halos using the so-called galaxy conserving model (Fry 1996, F1996) is calculated assuming that at the redshift of zCOSMOS observations the model bias has the same value as the bias of $M_B < -20 - z$ zCOSMOS galaxies at the $R = 10\,h^{-1}$ Mpc scale (dotted lines). The plotted zCOSMOS linear bias values $\hat{b}$ are corrected for the systematic reconstruction error. The plotted vertical error bars are the cosmic variance errors.

(A color version of this figure is available in the online journal.)

systematic reconstruction errors) to host a $M_B < -20 - z$ galaxy increases from $\sim 1.7 \times 10^{12}\,h^{-1}\,M_\odot$ at $z \sim 0.55$ to $4.1 \times 10^{12}\,h^{-1}\,M_\odot$ at $z \sim 0.75$ when using the halo bias approximation of Sheth et al. (2001; continuous curves in Figure 25) or from $\sim 4.2 \times 10^{12}\,h^{-1}\,M_\odot$ at $z \sim 0.55$ to $7.3 \times 10^{12}\,h^{-1}\,M_\odot$ at $z \sim 0.75$ when using the halo bias approximation of Pillepich et al. (2010; dashed curves in Figure 25). This result indicates that galaxies defined by the same $-\Delta z$ evolved luminosity reside on average in more massive halos at higher z (where $z < 1$). We do not include errors in the quoted characteristic halo masses, and therefore these values should not be used to infer the exact rate in evolution in the halo mass-to-light ratio, particularly having in mind the discrepancy from the zero mean overdensity field in the $0.6 < z < 0.9$ bin, which can largely affect the implied evolution. Physically, the inferred trend in the halo mass-to-light ratio is consistent with a scenario in which the star formation, as traced by the B-band luminosity, shifts from more massive to less massive halos with decreasing redshift. This is similar to the evolution in halo mass-to-light ratio found between the DEEP2 and SDSS (Zheng et al. 2007). Specifically, Zheng et al. (2007) find that the mean luminosity of the central galaxy increases with halo mass at both redshifts, and the central L_* galaxies reside in the halos a few times more massive at $z \sim 1$ than at $z \sim 0$. However, the physical interpretation of the results above is hampered by the fact that we (and Zheng et al. 2007) have used the luminosity-complete samples, defined here by their evolving B-band luminosity, which is very sensitive to the recent star formation history. Preferentially, one should use stellar masses to define complete samples.

From Figure 25 it is also noticeable that the models for the halo bias predict higher biasing of halos of higher mass. Moreover, the difference between the biasing of halos of different masses increases with redshift, reflecting the fact

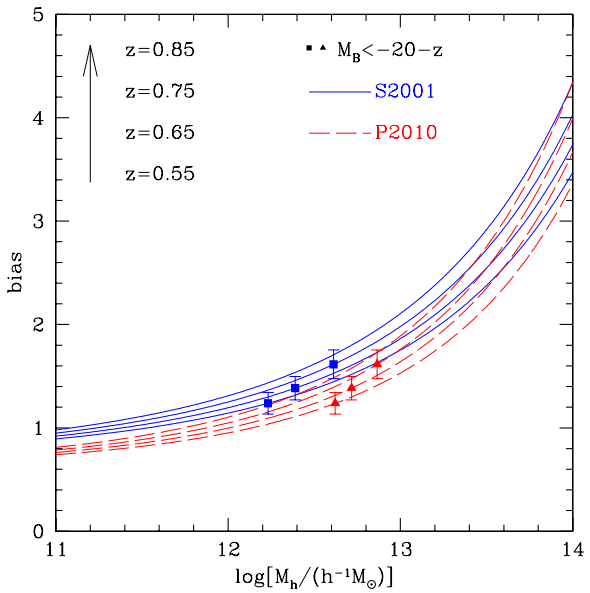

Figure 25. Bias of the dark matter halos at redshifts used in this analysis. The continuous and dashed curves correspond to the bias of dark matter halos of a given halo mass as given by Sheth et al. (2001, S2001) and Pillepich et al. (2010, P2010), respectively. The results are calculated for redshifts $z = 0.55$, $z = 0.65$, $z = 0.75$, and $z = 0.85$ (mean redshifts of the bins used in the presented biasing analysis) for the curves presented from the bottom to the top, as indicated by the arrow along the given redshift values. The filled symbols (squares and triangles) are the $\hat{b}$ values from the zCOSMOS analysis with the $M_B < -20 - z$ sample on the $R = 10\,h^{-1}$ Mpc scale, plotted at the values of a dark matter halo mass of the same bias as galaxies at the corresponding redshift. The squares are for the Sheth et al. (2001) approximation and the triangles are for the Pillepich et al. (2010) approximation. The $\hat{b}$ values are corrected for the systematic reconstruction error. The plotted vertical error bars are the cosmic variance errors.

(A color version of this figure is available in the online journal.)

that at high-redshift more massive halos are formed in the higher, and more rare density peaks, and therefore they are more biased tracers of the underlying mass distribution at higher redshifts. We measure higher linear biasing for more luminous galaxies, and therefore the characteristic halo mass of more luminous galaxies is higher. For example, when using the bias expression by Sheth et al. (2001), at $z \sim 0.55$ the characteristic mass of halos which host $M_B < 19.5 - z$ and $M_B < -20.5 - z$ zCOSMOS galaxies (taking into account systematic reconstruction errors) is $1.2 \times 10^{12}\,h^{-1}\,M_\odot$ and $4.0 \times 10^{12}\,h^{-1}\,M_\odot$, respectively. At $z \sim 0.75$, $M_B < -20.5 - z$ zCOSMOS galaxies are hosted by dark matter halos of mass of $7.0 \times 10^{12}\,h^{-1}\,M_\odot$. When using the bias expression by Pillepich et al. (2010), the corresponding characteristic masses are $3.3 \times 10^{12}\,h^{-1}\,M_\odot$, $8.0 \times 10^{12}\,h^{-1}\,M_\odot$ and $1.1 \times 10^{13}\,h^{-1}\,M_\odot$ for $M_B < 19.5 - z$ at $z \sim 0.55$, $M_B < -20.5 - z$ at $z \sim 0.55$ and $M_B < -20.5 - z$ at $z \sim 0.75$ zCOSMOS galaxies, respectively.

7. SUMMARY AND CONCLUSIONS

In this work, we make use of the reconstructed overdensity field in the zCOSMOS volume (see Kovač et al. 2010a) to derive the conditional mean function $\langle \delta_g | \delta \rangle = b(\delta, z, R)\delta$ and the second moments of the mean biasing function $b(\delta, z, R)$. For this purpose, we employ the density field on a grid reconstructed by using the three-dimensional distances between galaxies and grid points and counting the objects within a spherical top-hat aperture. We implement a novel method ZADE (Kovač et al. 2010a) to account for galaxies not yet observed spectroscopically in the selected samples of galaxies used to reconstruct the density field. For a biasing analysis, the main advantage of the ZADE method is that in a statistical sense, the mean intergalaxy separation is that of all galaxies in the selected galaxy sample, and not only of the sample of galaxies with spectroscopic redshifts.

We have carried out a number of tests on the mock catalogs to assess various errors which are going to affect our biasing analysis. Particularly, using the zCOSMOS like mock catalogs we have quantified uncertainties due to cosmic variance and the density field reconstruction errors. We have also broadly determined the expected effect of the shot noise errors.

1. Cosmic variance errors cause a spread in the $\langle \delta_g | \delta \rangle$ function: for a given δ there is a range of δ_g values measured in the mock catalogs. Quantifying this spread by the standard deviation σ of $\log(1 + \delta_g)$, we find that σ is largest in the most underdense regions where $\sigma \sim 0.1$, becomes lower at the intermediate δ values, $\sigma < 0.05$, and increases again in the most overdense regions up to $\sigma \sim 0.05$ at a given δ.
2. The systematic error in the reconstruction of the density field changes the shape of $\langle \delta_g | \delta \rangle$ in different ways for the flux-limited and luminosity-complete $M_B < -20 - z$ samples of tracer galaxies, being most relevant in the underdense regions. Moreover, for $\log(1 + \delta) > -0.5$, the reconstruction uncertainty is much smaller than the cosmic variance uncertainty.
3. The shot noise (discrete galaxy sampling) errors modify significantly the shape of the $\langle \delta_g | \delta \rangle$ function in the most underdense regions, making the local bias $b(\delta, z, R)$ values in the same regions appear higher.
4. The $\hat{b}$ parameter increases due to the shot noise and reconstruction errors. The $\tilde{b}/\hat{b}$ parameter is not susceptible to either of these errors. The cosmic variance causes a spread in the measured values of both of these parameters.

We can summarize our main findings in the biasing analysis of the 10k zCOSMOS galaxies as follows.

1. The conditional mean function $\langle \delta_g | \delta \rangle$ has a characteristic shape as described below. In most underdense regions, this function vanishes. At some $\delta < 0$, the conditional mean function appears and then rises sharply in the underdense regions, with the local slope of the biasing function larger than unity. Starting from around mean density and toward higher overdensities, the $\langle \delta_g | \delta \rangle$ function closely follows a linear relation $\delta_g = b\delta$ with b being a constant. In the most overdense regions zCOSMOS galaxies are antibiased, i.e., locally $b(\delta, z, R) < 1$. This is true for all samples of tracer galaxies used. The conditional mean function $\langle \delta_g | \delta \rangle$ is clearly nonlinear in the most overdense and underdense regions.
2. The $\langle \delta_g | \delta \rangle$ function shows some dependence on the scale in the most overdense regions, more pronounced at high redshift, such that at smaller scales galaxies are more biased tracers of the underlying matter distribution. At $\log(1 + \delta) = 1$ the difference between the $\delta_g(\delta)$ values smoothed with 8 and $12\,h^{-1}$ Mpc is different from zero at 3.0σ and 4.1σ levels in $0.4 < z < 0.7$ and $0.6 < z < 0.9$, respectively, using the random reconstruction errors. Based on the extrapolation of the tests on the mock catalogs, we do not expect that the results quoted above are dominated by the differential shot noise errors.
3. We observe a systematic dependence of $\langle \delta_g | \delta \rangle$ on the luminosity of the tracer galaxies, such that in the range from

the mildly overdense to the most overdense regions, and again in the most underdense regions of the mass density contrast, the local bias of more luminous galaxies is higher than the local bias of less luminous galaxies.

4. There is a systematic redshift evolution in the $\langle\delta_g|\delta\rangle$ function, consistent with the increase of the local bias with redshift. When taking into account the systematic reconstruction errors, the redshift evolution in the uderdense regions is almost negligible. Moreover, the differences between the $\langle\delta_g|\delta\rangle$ functions at different redshifts fall within the 1σ interval of cosmic variance errors.
5. The linear bias between the 10k zCOSMOS galaxies and mass is increasing with redshift. There is some evidence that more luminous galaxies are more biased tracers of matter. The $\hat{b}$ parameters for $M_B < -20.5 - z$ and $M_B < -20 - z$ samples are significantly different at 3.5σ in $z \sim 0.65$ when taking into account reconstruction errors, or at 1.9σ when adding also the expected contribution from the shot noise errors. We do not detect any significant dependence of the linear biasing parameter on the scale at which we measure galaxy overdensity fields. The nonlinearity parameter differs from unity by up to 2%, with the errors of the same order of magnitude. It does not change with the redshift, with the smoothing scale or with the luminosity of the tracer galaxies at a level higher than the relevant $\sim 1\sigma$ errors.
6. By comparing the galaxy biasing to the halo biasing, using the approximation for halo bias of Sheth et al. (2001) and Pillepich et al. (2010), we infer that the $M_B < -20 - z$ zCOSMOS galaxies in $0.4 < z < 1$ reside in dark matter halos with a characteristic mass of ~ 2.6 or $\sim 5.6 \times 10^{12}\, h^{-1}\, M_\odot$, using these two models, respectively. One would need to work with the stellar mass complete samples to obtain the evolution in characteristic halo mass whose physical interpretation is not ambiguous.

Broadly speaking, our results are in line with findings from the previous study of the nonlinear biasing of high-redshift galaxies (Marinoni et al. 2005, 2008) and, qualitatively, they follow the biasing history outlined by the theoretical works (e.g., Blanton et al. 1999, 2000; Somerville et al. 2001). When going into details, there are a number of discrepancies which need to be solved, such as the exact rate in the evolution of the linear biasing parameter or the dependence of biasing on the luminosity of tracer galaxies. While the current biasing results from the $z < 1.5$ surveys are important as they support the general picture of the biased galaxy formation and provide a framework for the future theoretical work, the fine-tuning of the galaxy formation models is still hampered by the limitations of the existing spectroscopic surveys at these redshifts, particularly by the cosmic variance.

We thank Annalisa Pillepich for useful discussions. We also thank M. G. Kitzbichler and S. D. M. White for providing the mock catalogs (Kitzbichler & White 2007). This work has been supported in part by a grant from the Swiss National Science Foundation and an ASI grant ASI/COFIS/WP3110I/026/07/0.

REFERENCES

Abazajian, K., et al. 2005, ApJ, 625, 613
Basilakos, S., Plionis, M., Kovač, K., & Voglis, N. 2007, MNRAS, 378, 301
Benson, A. J., Cole, S., Frenk, C. S., Baugh, C. M., & Lacey, C. G. 2000, MNRAS, 311, 793
Blanton, M., Cen, R., Ostriker, J. P., & Strauss, M. A. 1999, ApJ, 522, 590
Blanton, M., Cen, R., Ostriker, J. P., Strauss, M. A., & Tegmark, M. 2000, ApJ, 531, 1
Bolzonella, M., et al. 2010, A&A, 524, 76
Bond, J. R., Cole, S., Efstathiou, G., & Kaiser, N. 1991, ApJ, 379, 440
Capak, P., et al. 2007, ApJS, 172, 99
Carroll, S. M., Press, W. H., & Turner, E. L. 1992, ARA&A, 30, 499
Catelan, P., Lucchin, F., Matarrese, S., & Porciani, C. 1998, MNRAS, 297, 692
Cen, R., & Ostriker, J. P. 2000, ApJ, 538, 83
Coil, A. L., Newman, J. A., Cooper, M. C., Davis, M., Faber, S. M., Koo, D. C., & Willmer, C. N. A. 2006, ApJ, 644, 671
Coil, A. L., et al. 2008, ApJ, 672, 153
Coles, P., & Jones, B. 1991, MNRAS, 248, 1
Conway, E., et al. 2005, MNRAS, 356, 456
Cooray, A., & Sheth, R. 2002, Phys. Rep., 372, 1
Dekel, A. 2000, in ASP Conf. Ser. 201, Cosmic Flows Workshop, ed. S. Courteau & J. Willick (San Francisco, CA: ASP), 420
Dekel, A., Bertschinger, E., & Faber, S. M. 1990, ApJ, 364, 349
Dekel, A., Eldar, A., Kolatt, T., Yahil, A., Willick, J. A., Faber, S. M., Courteau, S., & Burstein, D. 1999, ApJ, 522, 1
Dekel, A., & Lahav, O. 1999, ApJ, 520, 24
de la Torre, S., et al. 2011, MNRAS, tmp, 88
de la Torre, S., et al. 2011, A&A, 525, 125
De Lucia, G., & Blaizot, J. 2007, MNRAS, 375, 2
Dressler, A. 1980, ApJ, 236, 351
Dunkley, J., et al. 2009, ApJS, 180, 306
Feldmann, R., et al. 2006, MNRAS, 372, 565
Fry, J. N. 1996, ApJ, 461, L65
Fry, J. N., & Gaztanaga, E. 1993, ApJ, 413, 447
Gaztañaga, E., Norberg, P., Baugh, C. M., & Croton, D. J. 2005, MNRAS, 364, 620
Jing, Y. P. 1998, ApJ, 503, L9
Jing, Y. P. 1999, ApJ, 515, L45
Kaiser, N. 1984, ApJ, 284, L9
Kaiser, N. 1987, MNRAS, 227, 1
Kauffmann, G., Nusser, A., & Steinmetz, M. 1997, MNRAS, 286, 795
Kayo, I., et al. 2004, PASJ, 56, 415
Kitzbichler, M. G., & White, S. D. M. 2007, MNRAS, 376, 2
Knobel, C., et al. 2009, ApJ, 697, 1842
Koekemoer, A. M., et al. 2007, ApJS, 172, 196
Kovač, K., Somerville, R. S., Rhoads, J. E., Malhotra, S., & Wang, J. 2007, ApJ, 668, 15
Kovač, K., et al. 2010a, ApJ, 708, 505
Kovač, K., et al. 2010b, ApJ, 718, 86
Kravtsov, A. V., & Klypin, A. A. 1999, ApJ, 520, 437
Lahav, O., Lilje, P. B., Primack, J. R., & Rees, M. J. 1991, MNRAS, 251, 128
Lee, K.-S., Giavalisco, M., Gnedin, O. Y., Somerville, R. S., Ferguson, H. C., Dickinson, M., & Ouchi, M. 2006, ApJ, 642, 63
Le Fèvre, O., et al. 2005, A&A, 439, 845
Lilly, S. J., et al. 2007, ApJS, 172, 70
Lilly, S. J., et al. 2009, ApJS, 184, 218
Magliocchetti, M., & Porciani, C. 2003, MNRAS, 346, 186
Mann, R. G., Peacock, J. A., & Heavens, A. F. 1998, MNRAS, 293, 209
Marinoni, C., et al. 2005, A&A, 442, 801
Marinoni, C., et al. 2008, A&A, 487, 7
Massey, R., et al. 2007, Nature, 445, 286
Matarrese, S., Verde, L., & Heavens, A. F. 1997, MNRAS, 290, 651
McCracken, H. J., et al. 2007, ApJS, 172, 314
Meneux, B., et al. 2008, A&A, 478, 299
Meneux, B., et al. 2009, A&A, 505, 463
Mo, H. J., Jing, Y. P., & White, S. D. M. 1997, MNRAS, 284, 189
Mo, H. J., & White, S. D. M. 1996, MNRAS, 282, 347
Moustakas, L. A., & Somerville, R. S. 2002, ApJ, 577, 1
Nishimichi, T., Kayo, I., Hikage, C., Yahata, K., Taruya, A., Jing, Y. P., Sheth, R. K., & Suto, Y. 2007, PASJ, 59, 93
Norberg, P., et al. 2001, MNRAS, 328, 64
Norberg, P., et al. 2002, MNRAS, 332, 827
Phleps, S., Peacock, J. A., Meisenheimer, K., & Wolf, C. 2006, A&A, 457, 145
Pillepich, A., Porciani, C., & Hahn, O. 2010, MNRAS, 402, 191
Pollo, A., et al. 2006, A&A, 451, 409
Porciani, C., Catelan, P., & Lacey, C. 1999, ApJ, 513, L99
Porciani, C., Matarrese, S., Lucchin, F., & Catelan, P. 1998, MNRAS, 298, 1097
Porciani, C., Magliocchetti, M., & Norberg, P. 2004, MNRAS, 355, 1010
Pozzetti, L., et al. 2010, A&A, 523, 13
Sanders, D. B., et al. 2007, ApJS, 172, 86

Scannapieco, E., & Barkana, R. 2002, ApJ, 571, 585
Scoville, N., et al. 2007a, ApJS, 172, 38
Scoville, N., et al. 2007b, ApJS, 172, 150
Seljak, U., & Warren, M. S. 2004, MNRAS, 355, 129
Sheth, R. K., & Lemson, G. 1999, MNRAS, 304, 767
Sheth, R. K., Mo, H. J., & Tormen, G. 2001, MNRAS, 323, 1
Sheth, R. K., & Tormen, G. 1999, MNRAS, 308, 119
Sigad, Y., Branchini, E., & Dekel, A. 2000, ApJ, 540, 62
Smith, R. E., et al. 2003, MNRAS, 341, 1311
Somerville, R. S., Lemson, G., Sigad, Y., Dekel, A., Kauffmann, G., & White, S. D. M. 2001, MNRAS, 320, 289
Springel, V., et al. 2005, Nature, 435, 629
Swanson, M. E. C., Tegmark, M., Blanton, M., & Zehavi, I. 2008, MNRAS, 385, 1635
Szapudi, I. 1998, ApJ, 497, 16
Szapudi, I., & Pan, J. 2004, ApJ, 602, 26
Tegmark, M., & Bromley, B. C. 1999, ApJ, 518, L69
Tegmark, M., & Peebles, P. J. E. 1998, ApJ, 500, L79
Tinker, J. L., Weinberg, D. H., Zheng, Z., & Zehavi, I. 2005, ApJ, 631, 41
van den Bosch, F. C., et al. 2007, MNRAS, 376, 841
Verde, L., Heavens, A. F., Matarrese, S., & Moscardini, L. 1998, MNRAS, 300, 747
Verde, L., et al. 2002, MNRAS, 335, 432
Wang, L., & Steinhardt, P. J. 1998, ApJ, 508, 483
White, S. D. M., & Rees, M. J. 1978, MNRAS, 183, 341
Wild, V., et al. 2005, MNRAS, 356, 247
Yang, X., Mo, H. J., Jing, Y. P., & van den Bosch, F. C. 2005, MNRAS, 358, 217
Yoshikawa, K., Taruya, A., Jing, Y. P., & Suto, Y. 2001, ApJ, 558, 520
Zehavi, I., et al. 2005, ApJ, 630, 1
Zheng, Z., Coil, A. L., & Zehavi, I. 2007, ApJ, 667, 760